Modeling of Plasma Irregularities Associated with Artificially Created Dusty Plasmas in the Near-Earth Space Environment

Haiyang Fu

Dissertation submitted to the Faculty of the
Virginia Polytechnic Institute and State University
in partial fulfillment of the requirements for the degree of

Doctor of Philosophy
in
Electrical Engineering

Wayne A. Scales, Chair
Paul A. Bernhardt
Robert C. Clauer
John M. Ruohoniemi
Timothy Pratt
Danesh K. Tafti

December 10, 2012
Blacksburg, Virginia

Keywords: Space Plasma Physics, Ionospheric Irregularities, Active Space Experiment,
Hybrid Computational Model, Dust Aerosol Charging

Modeling of Plasma Irregularities Associated with Artificially Created Dusty Plasmas in the Near-Earth Space Environment

Haiyang Fu

(ABSTRACT)

Plasma turbulence associated with the creation of an artificial dust layer in the earth's ionosphere is investigated. The Charged Aerosol Release Experiment (CARE) aims to understand the mechanisms for enhanced radar scatter from plasma irregularities embedded in dusty plasmas in space. Plasma irregularities embedded in a artificial dusty plasma in space may shed light on understanding the mechanism for enhanced radar scatter in Noctilucent Clouds (NLCs) and Polar Mesospheric Summer Echoes (PMSEs) in the earth's mesosphere. Artificially created, charged-particulate layers also have strong impact on radar scatter as well as radio signal propagation in communication and surveillance systems. The sounding rocket experiment was designed to develop theories of radar scatter from artificially created plasma turbulence in charged dust particle environment. Understanding plasma irregularities embedded in a artificial dusty plasma in space will also contribute to addressing possible effects of combustion products in rocket/space shuttle exhaust in the ionosphere.

In dusty space plasmas, plasma irregularities and instabilities can be generated during active dust aerosol release experiments. Small scale irregularities (several tens of centimeter to meters) and low frequency waves (in the ion/dust scale time in the order of second) are studied in this work, which can be measured by High Frequency (HF), Very High Frequency (VHF) and Ultra High Frequency (UHF) radars. The existence of dust aerosol particles makes computational modeling of plasma irregularities extremely challenging not only because of multiple spatial and temporal scale issue but also due to complexity of dust aerosol particles.

This work will provide theoretical and computational models to study plasma irregularities driven by dust aerosol release for the purpose of designing future experiments with combined

ground radar, optical and in-situ measurement. In accordance with linear analysis, feasible hybrid computational models are developed to study nonlinear evolution of plasma instabilities in artificially created dusty space plasmas. First of all, the ion acoustic (IA) instability and dust acoustic (DA) instability in homogenous unmagnetized plasmas are investigated by a computational model using a Boltzmann electron assumption. Such acoustic-type instabilities are attributed to the charged dust and ion streaming along the geomagnetic field. Secondly, in a homogenous magnetized dusty plasma, lower-hybrid (LH) streaming instability will be generated by dust streaming perpendicular to the background geomagnetic field. The magnetic field effect on lower-hybrid streaming instabilities is investigated by including the ratio of electron plasma frequency and electron gyro frequency in this model. The instability in weakly magnetized circumstances agree well with that for the ion acoustic (IA) instability by a Boltzmann model. Finally, in an inhomogeneous unmagnetized/magnetized dust boundary layer, possible instabilities will be addressed, including dust acoustic (DA) wave due to flow along the boundary and lower-hybrid (LH) sheared instability due to flow cross the boundary.

With applications to active rocket experiments, plasma irregularity features in a linear/nonlinear saturated stage are characterized and predicted. Important parameters of the dust aerosol clouds that impact the evolution of waves will be also discussed for upcoming dust payload generator design. These computational models, with the advantage of following nonlinear wave-particle interaction, could be used for space dusty plasmas as well as laboratory dusty plasmas.

This work received financial support from National Science Foundation.

Dedication

To my family, who inspired me with love.

Acknowledgments

I would like to thank my advisor, Prof. Wayne A. Scales, for his tremendous support, comprehensive guidance and great patience. His scientific passion and knowledge have greatly affected on this research work. I would also appreciate Prof. Wayne A. Scales for providing unique opportunities to improve myself not only academically but also personally.

I would like to express my great gratitude to Dr. Paul A. Bernhardt for his advice on this work. His insightful knowledge and delightful personality has inspired me great passion for research and humorous wisdom for life. The discussion with Dr. Paul A. Bernhardt has contributed significantly to this work. Also, I want to thank Dr. Marlene Rosenberg for providing valuable comments on my research work.

I would like to acknowledge my dissertation committee members for their willingness to serve and for providing helpful feedback on my research, Prof. Robert C. Clauer, Prof. John M. Ruohoniemi, Prof. Timothy Pratt and Prof. Danesh K. Tafti. Also thanks for Prof. Scott Bailey, Prof. Gregory Earle and Prof. Joseph Baker for useful discussions.

I would like to acknowledge and thank my colleagues at the Space Science and Engineering Research Center at Virginia Tech. I want to express my special thanks to Alireza Mahmoudian, Maitrayee Ranade Bordikar, Alireza Samimi and John Janeski for their research collaboration, discussion and friendship. These memories will be always cherished as a part of my life journey at Virginia Tech. Thanks for my friends Ying-tsen Lin and Brentha Thurairajah for their support and friendship. Thanks for Nathaniel Frissell and de Larquier

Sebastien for providing SuperDARN radar support.

I am very grateful to all of my friends in Blacksburg who made my life full of sincere friendship and joyful memories. I want to give my special thanks to my friends to Dr. Pu Wang, Dr. Zhiye Zhang, Dr. Qing Yang, Dr. Yu Lei, Dr. Senlin Peng, Tong Qin and Shaobin Liu for your kindness. Also, I am very grateful to my friends Dr. Hengheng Chen, Yue Meng, Jingyao Zhang, Yue Yan and Yiran Li for sharing your life with me. My life is so great with all of you.

Finally, I would like to thank my parents and my sister for all their deep love and forever support. I am deeply indebted to my husband, Weipeng Li, for his patient love. Although we stay far away from each other, he is the very one who always raises me up with all his love. It is all love that motivates me to complete this dissertation. Special thank to Chinese Scholarship Council for financial support during my study.

Contents

List of Figures

List of Tables

Chapter 1

Introduction

The near-earth space environment and its response to natural and artificial disturbances have strong impact on human societies, including Global Positioning System (GPS), over-the-horizon radars, HF communications, satellites, as well as global climate change [*Baker*, 2000]. The earth's upper atmosphere can be classified in several ways such as troposphere, stratosphere, mesosphere and thermosphere based on neutral characteristic temperature regime and ionosphere and magnetosphere based on the plasma characteristic ionization regime. The ionosphere, as an ionized plasma layer, extends a vertical height approximately from 50 km to 600 km in the upper atmosphere.

Radio waves propagate and reflect in the ionosphere depending on frequencies, polarizations and ionospheric environment. It was first demonstrated on December 12, 1901 when *Gugliemo Marconi* received wireless radio signals across the Atlantic. In 1902, *Oliver Heaviside* and *Arthur Keenelly* proposed that radio waves must have been reflected by the existence of the Kennelly-Heaviside Layer of the ionosphere. Direct evidence for the existence of the ionized layer was measured by *Appleton* and *Barnett* in England in 1925 and *Breit* and *Tuve* in America in 1926. *Robert Watson-Watt* introduced the term *ionosphere* in 1926. The basic physics of the ionized layer formation was explained by *Chapman* in 1931. In late 1950s, ionospheric physics developed with in situ sampling by rockets and satellites and earth-based

radar observations of Thomson (or incoherent) Scatter [*Evans*, 1968].

The ionosphere varies continuously with universal time, with seasons, with latitude and longitude and solar activities. Ionospheric disturbances arise and exist at various scales, since the ionosphere is coupled with the lower thermosphere and the upper magnetosphere in the solar system.

The ionosphere is generally classified into layers in equilibrium as following:

1). D-region ($50 \sim 90\,\mathrm{km}$), it represents the lowermost part and a highly collisional region with electron density in the order of $10^8 \sim 10^{10}\,\mathrm{m}^{-3}$. The molecular ions O_2^+ by $0.1 \sim 1\,\mathrm{nm}$ solar X-rays and NO^+ by the $\mathrm{Lyman}_\alpha = 121.6\,\mathrm{nm}$ are principal constituents.

2). E-region ($90 \sim 130\,\mathrm{km}$), the ions in E layer are mainly O_2^+ and NO^+ produced by solar X-rays in the $1 - 10\,\mathrm{nm}$ range and Extreme ultraviolet EUV radiation in the $100 \sim 150\,\mathrm{nm}$ range. The electron density is of the order $10^{11}\,\mathrm{m}^{-3}$. Sporadic E layers of enhanced ionization occur at mid-latitudes in the lower E region at altitudes between $95 \sim 120\,\mathrm{km}$

3). F1-Region ($150 \sim 220\,\mathrm{km}$ only during the daytime), it is composed of a mixture of molecular ions O_2^+ and NO^+, and atomic ions O^+. The ionization source for this region is the least penetrating EUV radiation. Because of the presence of molecular ions, the chemistry is controlled by dissociative recombination. The F1 layer merges into the F2 layer at night.

4). F2-Region ($220 \sim 500\,\mathrm{km}$), the region primarily consists of atomic ions O^+ , with maximum production in the F1 region. The region has the maximum electron density up to $10^{12}\,\mathrm{m}^{-3}$, due to the presence of the atomic ions which are lost by charge transfer processes with molecular neutral species. The Chapman function is not good for F2 region since this layer is controlled not only by recombination but also by other chemical process and plasma vertical drift transport processes.

The F layer of the ionosphere with the maximum plasma density is responsible for most skywave propagation, facilitating high frequency (HF or shortwave) radio communications

over long distances. Ionospheric disturbances may have strong impact on radio propagation in communication system performance (signal fading) and navigation system. The mechanism of ionospheric disturbances may be generated by natural sources such as solar activity and artificial sources such as meteors, rocket/space shuttle exhausts, and high power radio waves.

The purposes of active space experiment to study ionospheric physics are:

1). To open the possibility of imitating natural phenomena and following its formation, evolution, and properties with ground and space-based diagnostics in the near earth environment;

2). To understand the impact of ionospheric disturbances on radio propagation in communication and surveillance system performance;

3). To allow for possible new communication system technique (i.e., Natural Ionospheric Currents and Stimulated Electromagnetic Emission).

1.1 Motivation

Over tons of meteoric dust enters the earth's atmosphere every day, which deposit mass, momentum and energy in the ionosphere. This dust settles and creates natural dust layers in the altitude range $80 \sim 100\,\mathrm{km}$ such as metal layers commonly measured by Lidars, which spans the earth's upper mesosphere to lower thermosphere. These dust layers are immersed in the earth's upper atmosphere, they become charged solid particulates due to accumulation of electrons and ions from earth's ionospheric plasma. Dust particles could become the source of the condensation nuclei (CN) for ice layer-related phenomena including Noctilucent Clouds NLCs and Polar Mesospheric Summer Echoes PMSEs. Noctilucent Clouds NLCs are a fascinating visual manifestation of these dust layers. So-called Polar Mesospheric Summer Echoes PMSEs are radar echoes that are a direct consequence of the

Table 1.1: Dust particles in the Earth's environment [After *Shukla and Mamun*, 2002]

Origin	**Composition**	**Radius** (μm)	**Density** (cm^{-3})
Shuttle exhausts	dirty ice	5×10^{-3}	3×10^{4}
Terrestrial aerosal	Aluminum Oxide Al_2O_3 spheroid	$0.1 - 10$	$10^{-10} - 10^{-6}$
Micrometeoroid	60% chondritic, 10% silicates	$5 - 10$	$10^{-10} - 10^{-9}$
	30% iron-sulfur-nickel		
Industrial contamination	magnetite spherule	~ 10	$\sim 10^{-5}$
NLCs and PMSEs	ice particles	≤ 0.1	~ 10

sub-visible charged dust that exists at altitudes above NLC regions. Because of the intimate relationship between these phenomenological signatures and the global environment [*Stones*, 1991; *Gore*, 1992; *Gadsden*, 1990], the study of such natural dust layers is a forefront issue in upper atmospheric space science, which attracts more attention with the trend of global climate change. There are many unresolved issues regarding the basic physics of natural dust layers. The study of such natural dusty plasma physics can also help understand fundamental dusty plasma phenomenon in astrophysical environments from the interstellar medium to cometary tails, planetary ring system and also laboratory plasmas such as fusion energy schemes and semiconductor manufacturing [*Smith*, 1982; *Selwyn*, 1994; *Tsytovich*, 1998; *Shukla*, 2001]. The source, constituent, size, density of dust particles in the earth's atmosphere is summarized in Table 1.1 [*Shukla and Mamun*, 2002].

An alternate approach to understanding natural dust layers is to perform active space experiments in which a dust cloud is artificially created in a controlled manner in the upper atmosphere. The formation, evolution and properties of the artificially created dust clouds can be more carefully observed and studied and then compared to characteristics of natural dust clouds. A comparison of natural and artificially created dust clouds is expected to be quite enlightening and lead to more insight into the physical processes associated with natural dust clouds. Several important issues to be investigated include dust charging pro-

Figure 1.1: Noctilucent clouds over Finland [Photographed by Pekka Parviainen]

cesses, plasma flows, electrodynamics structure, plasma irregularities, and coupling between the neutral components of the upper atmosphere and the dust clouds. Also, possibilities of sensor techniques for plasma processes in these dusty clouds could be evaluated through combined radar, optical and in-situ measurements. In particular, radar signals scattered from plasma irregularities in artificially created dusty plasmas will be modified by dust particles according to electromagnetic wave theory. Such active experiment could also provide insight into ionospheric phenomenon modified by rocket/space shuttle plume, which may impact electromagnetic wave propagation.

1.2 Charged Aerosol Release Experiments

The Charged Aerosol Release Experiment (CARE) is such an active ionospheric modification experiment, which aims to examine the effect of artificially created, charged-particulate layers on the scatter of UHF, L-Band, and S-Band radars [*Bernhardt et al.,* 2012]. The CARE rocket experiment will be conducted to test theories of radar scatter from electron density irregularities embedded in charged particulates in the ionosphere [*Kelley et al.*, 1987; *Bingham et al.,* 1991; *Hagfors*, 1992; *Cho et al.*, 1992]. The sounding rocket experiment includes a chemical release module and multiple space and ground based instruments. The CARE I sounding rocket used a chemical release from a Nihka motor with 111 kg of aluminum

Table 1.2: Nihka motor properties [After *Bernhardt et al.*, 2012].

Quantity	Value
Motor Diameter	0.4384 m
Motor Length	1.92 m
Motor Mass	402.1 kg
Fuel Mass	315.1 kg
Nozzle Throat Area	0.00413 m^2
Nozzle Area Ratio	27.26
Nozzle Exit Diameter	0.379 m
Nozzle Divergence Angle	19.61 Degrees
Throat Gas Temperature	3523.8 K
Throat Gas Pressure	29.2 atm
Throat Gas Velocity	1945.9 m/s
Gas Specific Heat Ratio	1.1712
Exit Gas Temperature	1734.5 K
Exit Gas Pressure	0.207 atm
Exit Gas Velocity	2835.2 m/s
Engine Burn Duration	17.79 s
Thrust	51.079 kN
Total Impulse	908.77 kN − s
Specific Impulse	2882.51m/s

oxide (Al_2O_3) dust and 200 kg of exhaust molecule vapors, which was fired at the altitude 280 kg. The CARE I sounding rocket mission was conducted from NASA's Wallops Flight Facility in Virginia on 19 September 2009 at 23:46 GMT (18:46 local time) near sunset.

The sounding rocket for the CARE I mission was configured as a Black Brant XII with the Nihka motor used as the chemical payload. The Black Brant XII is a four-stage, solid propellant sounding rocket consisting of a Talos 1st stage, Taurus 2nd stage, Black Brant 3rd stage, and Nihka 4th stage. The Nihka motor properties are listed in Table 1-2 [*Bernhardt et al.*, 2012]. The exhaust material, composed of 1/3 aluminum oxide particles as dust particulate and 2/3 combustion product molecules, similar compositions as listed in Table 1.1. The dust aerosols and molecules may interact with the ionosphere to create a dusty plasma with high-speed pick-up ion beam, charged dust beam and electron density depletion region. The composition of the chemical payload is listed in Table 1-3 [*Bernhardt et al.*, 2012]. The 111 kg of aluminum oxide particulate form a charged dust cloud as one dominant energy source for plasma wave excitation. Over 200 kg of molecules from the rocket release react with O^+ ion in the F-layer of the ionosphere. These molecules may charge exchange to produce a charged ion beam as another energy source for exciting plasma irregularities. The effects of charged dust from hypersonic ions can be distinguished by in-situ wave observations, ground radar scatter, and optical emissions.

The trajectory of the sounding rocket and radio beacon experiment are sketched in Figure 1.2a [*Bernhardt et al.*, 2012]. The Nihka motor fired at altitude $\sim$ 280km within 17.8 s with approximately about 3 km/s velocity relative to the background ionosphere. The dual frequency (150 MHz and 400 MHz) radio beacon was the only instrument on the the chemical release payload used for the Coherent Electromagnetic Radio Tomography experiment, which has the capability to show the formation of an electron hole in the dust cloud regions and variations of VHF and UHF signals passing through the exhaust plume [*Bernhardt et al.*, 1993; *Bernhardt et al.*, 2012].

The ground diagnostics sites are shown in Figure 1.2b, including Westford, Massachusetts;

Table 1.3: Constituent in the dust generator [After *Bernhardt et al.*, 2012]

Constituent	**Mass** kg	**Mole Fraction**
Carbon Monoxide (CO)	69.1	0.2039
Carbon Dioxide (CO_2)	9.9	0.0186
Monatomic Chlorine(Cl)	5.3	0.0124
Hydrogen Chloride(HCl)	65.2	0.1478
Hydrogen(H_2)	6.6	0.2712
Monatomic Hydrogen (H)	0.4	0.0317
Water (H_2O)	30.4	0.1393
Nitrogen(N_2)	27.7	0.0817
Aluminum Oxide(Al_2O_3)	110.6	0.0897

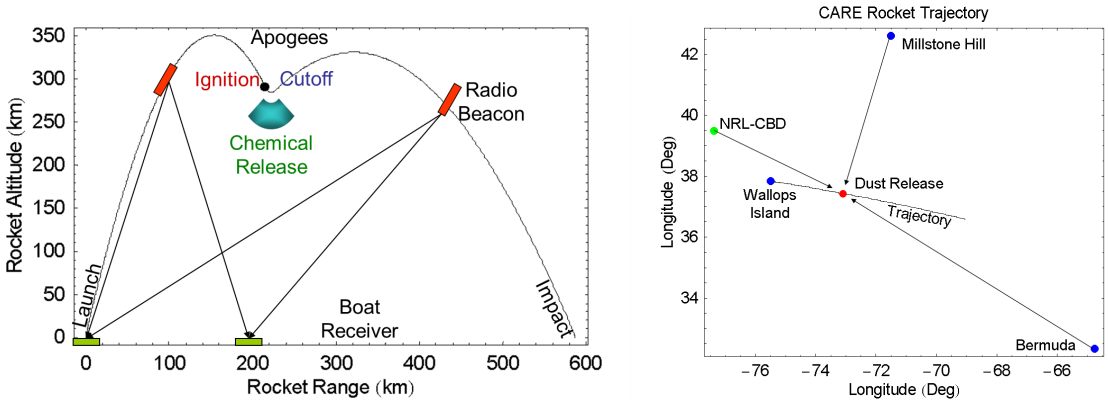

Figure 1.2: a) Nozzle Nihka motor chemical payload trajectory and radio beacon experiment schematic (left) and b) ground diagnostic sites for the CARE I experiment (right) [After *Bernhardt et al.*, 2012]

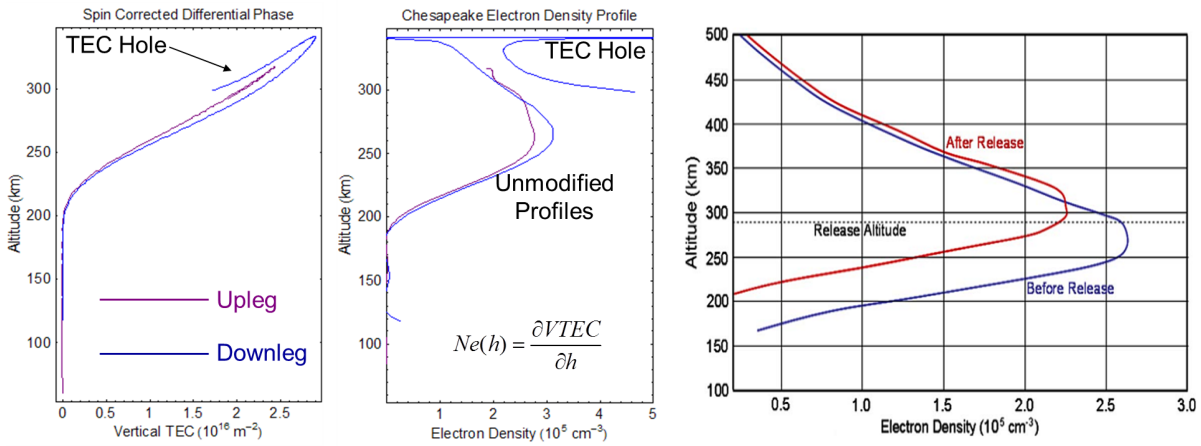

Figure 1.3: Total electron content and electron density disturbances by the CARE I chemical release determined by radio beacon propagation (left) and by the Millstone Hill ISR (right) on 19 September 2009 [After *Bernhardt et al.*, 2012].

Wallops Island, Virginia; Bermuda and NRL-CBD. The ground equipment include 440 MHz UHF Millstone Incoherent Scatter Radar(ISR), Haystack, Massachusetts; Digisonde and Dynasonde, Wallops Island, Virginia; 50 MHz VHF radar, Bermuda; and NRL Optical Test Facility, MRC, Virgnia.

The ISR radar and radio beacon data show a similar magnitude for electron density profiles and TEC reduction in Figure 1.3 [*Bernhardt et al.*, 2012]. The electron density reduction has contributions primarily from exhaust molecule reactions rather than the charging process of the dust particles. *Bernhardt et al.* [2012] points out that the electron density reduction by charging of dust particles is only important at early times when the cloud has not expanded to more than 1 km in radius.

The optical signature of the CARE I release has been previously reported as shown in Figure 1.4 [*Bernhardt et al.*, 2011; *Bernhardt et al.*, 2012]. Figure 1.4 shows sunlight scattered from dust clouds with a conical spread and red-Line emission from excited atomic oxygen from electron and ion recombination recorded by a CCD camera. The major emission species and the ion-electron recombination emission lines can be identified by spectroscopy during the

Figure 1.4: Images of the CARE I dust and molecular exhaust release showing (left) sunlight scattered from the aluminum oxide particulates and (right) dust ring produced by motor coning along with red-line emissions from excited atomic oxygen [After *Bernhardt et al.*, 2011].

release process. Optical phenomena of gasdust formations from rocket exhaust in the upper atmosphere has been classified by *Platov et al.* [2004] as well. Small impurities of sodium and potassium were observed and reported by *Bernhardt et al.* [2012].

A follow-on CARE II mission is planned by Naval Research Lab for launch from Andoya, Norway, in 2013. The CARE II mission will be modified based on the first CARE I experiment and theoretical and computational work afterwards. One important feature of the CARE II mission will be the reduced firing time from 17.8 s to 2 s. The CARE II mission will incorporate in-situ instruments for dust particles and plasma wave measurement.

1.3 Review of Related Phenomena

1.3.1 Review of Polar Mesospheric Clouds and Summer Echoes

Mesospheric clouds, including NLCs and PMSEs have been studied by sophisticated radar experiments as well as lidar and in situ rocket measurements, which have shed some light on the underlying physics and chemistry for remarkably strong radar echoes from the summer polar mesosphere. Mesospheric clouds have also been studied by satellites called Polar mesospheric clouds PMCs. The relation between NLCs, PMSEs, PMC are closely related with each other.

Noctilucent clouds were first identified as "shining night clouds" by *Backhouse* in 1885 at height $\sim$ 82 km first measured through triangulation techniques [*Jesse et al.*, 1887]. NLC occurs in summer at altitudes around $82 \sim 83$ km, visible only in twilight as shown in Figure 1.1, generally at solar depression angles between 6° and 16° [*Thomas*, 1991]. Right above NLC altitudes, polar mesosphere summer echoes (PMSEs) were first observed by the Poker Flat 50 MHz radar in Alaska [*Ecklund and Balsley*, 1981] nearly a century after the first sighting of NLCs. These remarkable PMSEs echoes just above NLCs clouds height were widely observed and reported continuously by UHF (EISCAT 933 MHz and Sondrestrom 1.29 GHz), VHF (Poker flat 50 MHz and EISCAT 224 MHz), HF ($8 \sim 9$ MHz radars at higher latitude ($> 52^o$), which have been summarized by *Cho and Rottger* [1997]. Review papers on NLCs and PMSEs are referred [*Cho and Kelly*, 1993; *Cho and Rottger*, 1997; *Rapp and Lubken*, 2004].

Radar waves are mostly scattered by refractive index structures equal to the radar half wavelength known as Bragg scatter condition. For instance, the commonly used VHF 50 MHz radar in the mesosphere is sensitive to irregularities with 3 m wavelength. The nature of the mechanism for generating irregularities in the refractive index is, still not fully understood. However, NLCs and PMSEs are commonly considered to be closely related with ice particles in these regions at a extremely low temperature below 100 K [*Schmidlin et al.*, 1992].

Experimental radar observations for PMSEs suggest that the irregularity length scale extends to the viscous subrange (where the air fluctuation dissipated by molecular viscosity) of clear air turbulence, which is supposed to be in the inertial subrange (where irregularities exist). The question becomes why small scale irregularities could be generated and exist in the viscous subrange of the clear air turbulence. *Kelly et al.* [1987] proposed that the charged dust grains (icy particles) play the role as the heavy positive ions causing the kinematic viscosity to decrease and shifting the transition scale in the plasma so that the neutral turbulence may affect the small scales of the plasma directly. *Cho et al.* [1992] shows an aerosol with a radius of $0.01\,\mu$m can raise the Schmidt number $S_c = \nu/D$ to 100, where ν is the kinematic viscosity and D is the electron diffusion coefficient. Figure 1-5a shows the effect of charged aerosols on mesospheric radar scatter, which extends the radar reflectivity to shorter scales for a larger Schmidt number $S_c = \nu/D$ [*Cho and Kelly*, 1993], with the turbulent energy dissipation rate $\epsilon = 1\,\mathrm{W/kg}$ (the rate at which turbulent kinetic energy is dissipated to heat).

In addition to radar measurement, PMSEs have been studied by rocket/radar campaign in the 1980s, summarized by *Rapp and Lubken* [2004]. One of the most prominent feature of the PMSE region is the electron density 'biteouts' observed in almost all rocket borne electron number density measurements in the vicinity of PMSE and also detected by the UHF radars [*Rottger et al.*, 1990]. Figure 1.5b shows the electron density 'biteout' profile and enhanced radar power from the STATE campaign in 1983 [*Ulwick et al.*, 1988]. The electron biteouts are direct evidence for the presence of charged ice particles. *Ulwick et al.* [1988] also showed the electron density fluctuation level in the order of $1 \sim 100\,\mathrm{Hz}$ and the spectral power of the electron density fluctuation locates in an inertial subrange of homogeneous, isotropic turbulence.

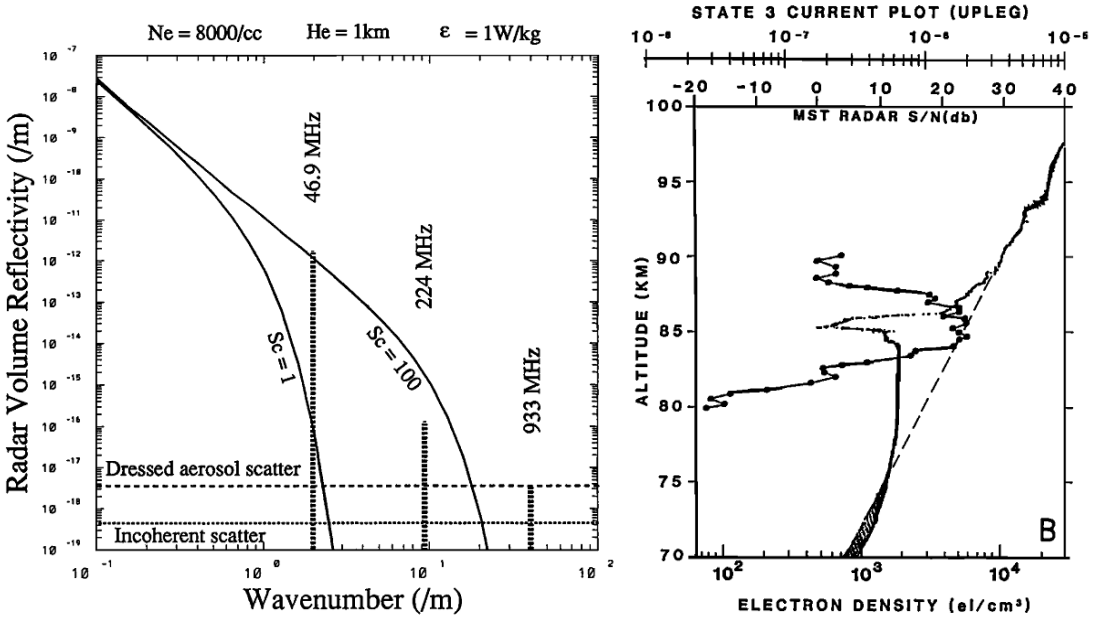

Figure 1.5: a) The radar reflectivity model for two Schmidt numbers S_c (left) [After *Cho and Kelley*, 1993] and b) height profiles of rocket borne DC probe measurements of the electron number density (solid line) and VHF radar echoes (solid circles) for the STATE-3 rocket flight conducted on 17 June 1983 from Poker Flat, Alaska. The dashed line illustrates a more typical D-region electron number density (right) [After *Ulwick et al.*, 1988].

1.3.2 Review of Previous Aerosol Release Studies

Aerosol release materials from man-made objects can unintentionally/intentionally generate ionospheric depletion and disturbances mainly in the F layer of the ionosphere. Such ionospheric disturbance could have great impact on communication and surveillance systems, particularly for large launching rocket system.

On February 17, 1959, an ionospheric hole was measured by ionosonds for about half an hour when Vanguard II penetrated the F region of the ionosphere. It was interpreted that the missile's exhaust gases "punched" a hole in the ionoshere [*Booker et al.*, 1961]. Later in 1962, a similar ionospheric hole was observed in the wake of a NASA rocket exhaust burn using the Faraday rotation to detect a reduction in total electron content (TEC) [*Jackson et al.*, 1962]. In 1973, after the launch of NASA's Skylab I by a Saturn 5 rocket, the ionosphere was widely disturbed in a region approximately 1000 km in radius and the disturbance appeared as the dramatic 'bite-out' of substantial magnitude ($> 50\%$) for about several hours from both Faraday rotation and total electron content (TEC) data. The specific mechanism involved was the rapid ion-atom interchange reactions between the ionospheric O^+ and the hydrogen and water vapor molecules in the plume, followed by dissociative recombination of the molecular ion [*Mendillo et al.*, 1975a and 1975b].

The mechanism of ionospheric depletion or ionospheric hole include (i) snow plow effects, (ii) plasma depletion and (iii) electron attachments, which are summarized by *Mendillo et al.* [1988] as following. First of all, the snow plow effects happen because a rocket exhaust cloud literally push aside ionospheric plasma. This phenomenon exists close to the exhaust of any injection of a dense gas into plasma for a short time scale. Secondly, the plasma depletion process is the rapid conversion of the dominant ionospheric ion O^+ to a molecular ion. The generic process as described by *Mendillo et al.* [1988] is $O^+ + M_n \rightarrow M_m^+ + N_n$ and $M_m^+ + e^- \rightarrow \text{neutrals} + \text{Airglow}$, where $M_n = H_2$, H_2O, CO_2, $M_m^+ = OH^+$, H_2O^+, O_2^+, $N_n = H$, O, CO, O. Plasma ion and electron pairs are removed by artificially enhancing the conversion of atomic ions to molecular ions, which is the slowest process in the normal

F-region loss process. Thirdly, the electron depletion process is due to electron attachment process for materials with high electron affinities such as SF_6, Al_2O_3. This process results that the ambient plasma of positive ions and electrons converts to to a plasma of both positive and negative ions. One such example process can be summarized as $e^- + SF_6 \rightarrow SF_6^-$ and $e^- + SF_6 \rightarrow SF_5^- + F$ [*Bernhardt*, 1984; *Bernhardt et al.*, 1987a].

The first set of active ionospheric modification experiments were undertaken in 1960 and 1962 during the Air Force sponsored project Firefly [*Rosenberg*, 1964]. Four such experiments used sulfur hexafluoride (SF_6) releases. After the discovery of the Skylab effect and its verification via the Lagopedo experiments, several experiments have been conducted to characterize the disturbances induced by larger rockets passing through the ionosphere on satellite launching missions, such as HEAO-C [*Mendillo and Bernhardt*, 1980] and Atlas-F [*Mendillo and Baumgardner*, 1982]. During active space experiments, atmospheric disturbances were diagnosed with incoherent scatter radars, optical system and total electron content (TEC) monitoring stations.

NASA sponsored a series of burns during the SpaceLab 2 Mission for the Ionospheric Depletion Experiments (IDE), which may be the best chance to study the physical process associated with disturbance by the rocket exhaust [*Bernhardt et al.*, 2012]. After launch of the Challenger on 12 July 1985, seven dedicated firings of the Space Shuttle orbital maneuver subsystem (OMS) engines were conducted over incoherent scatter radars. One of the largest IDE burn was observed by the Millstone Hill radar and 630.0 nm optical emission [*Mendillo et al.*, 1988]. Another IDE burn over the Arecibo ISR produced a localized ionospheric hole and enhanced radar scatter correspondingly in this region caused by exhaust induced turbulence for about 30 s [*Bernhardt et al.*, 1988]. *Mendillo* et al. [2008] reported the last Titan launch from the U.S. burning, which pointed out that large-scale gradients in TEC could be produced by the rocket exhaust gas similar to those found during ionospheric storms. *Ozeki* and *Heki* [2010] provided measurements of the large ionospheric hole generated by the North Korean launches of the Taepodong-1 on 31 August 1998 and Taepodong-2 on 9 April 2009.

The next series of experiments with rocket motors firing in the ionosphere is called Shuttle Ionospheric Modification with Pulsed Localized Exhaust (SIMPLEX) experiments by the DoD Space Test Program (STP) with collaborations of NASA and the NRL. The concept of SIMPLEX aims to investigate artificial plasma turbulence driven by rocket exhaust in the ionosphere using ground based radars. The Shuttle Exhaust Ion Turbulence Experiment(SEITE) mission by NRL aims to investigate plasma turbulence driven by rocket exhaust in the ionosphere using space-based sensors, which provided opportunities to fly on-orbit satellite instrumentation through far-field plumes from the Space Shuttle OMS engine. The purpose of both campaigns was to develop quantitative models of plasma turbulence that can affect tracking and imaging radars. A review paper by *Bernhardt et al.* [2012] summarized ground and space-based measurement of rocket engine burns in the ionosphere, including the results of the series of SIMPLEX experiments, SEITE experiment, IDE experiment as well as the CARE experiment.

In addition to ionospheric experiments in space shuttle, there have been sounding rockets campaigns NICARE 1 and 2 [*Bernhardt et al.,* 1991; *Bernhardt et al.,* 1993], and Ionospheric Focused Heating (IFH) [*Bernhardt and Duncan*, 1987b; *Bernhardt et al.,* 1995] with Combined-Release and Radiation Effects Satellite CRRES. These experiments aimed to create electron depletion materials and chemical effects on the electromagnetic wave propagation in the ionosphere. High resolution measurements were obtained with in situ probes and high power radio waves. Experimental results by the in-situ measurement shows electron depletion in the early time period 0.1 s. More importantly, small-scale irregularities in the boundary layer were observed during such experiments, in the form of electron density cavities and spikes with diameter from $1 \sim 10$ m. There have been many papers on small scale irregularities generation during such electron attachment material release experiment [e.g., *Ganguli et al*, 1993; *Scales et al*, 1993; *Scales et al,* 1994; *Scales et al,* 1995]. These sounding rockets experiments provide experimental background for the recent CARE mission in this work.

There have been several application for studying rocket release exhaust on the ionosphere

in a controlled way. First of all, the active rocket aerosol release experiment contributes to understanding the ionospheric modification process by dust aerosol particles (electron attachment material) in the PMSE region as well as in large rocket exhaust plume. Secondly, the enhanced radar backscatter is primarily associated with plasma irregularities generation mechanism particularly in the dusty plasma, which may applied for explaining PMSE strong radar echoes, equatorial irregularities and Sporadic-E Layer. Thirdly, this experiment provides a method to study how high frequency radio signals are attenuated by a dust clouds. Fourthly, experimental radar data provide validation for radar theory in a dusty beam plasma environment. Fifthly, an artificially created ionospheric depletion opens up a window for studying low frequency cosmic ray. Sixthly, ionospheric depletion may cause ionospheric focused heating to enhance the power density in the radio beam, which can possibly stimulate new interactions between the radio wave and the ionospheric plasma (e.g., Stimulated Brillouin Emission and oscillating two-stream instabilities).

1.4 Scope of Dissertation

The dissertation is organized as below. Chapter 2 introduces the definition of dusty plasmas, governing equations of plasma, hybrid computational dusty plasma method and numerical techniques in this dissertation. Chapter 3 presents theory and model of the ion acoustic instability in unmagnetized plasmas (along the magnetic field) in a homogeneous plasma. Chapter 4 presents theory and model of dust acoustic instability in unmagnetized plasmas (along the magnetic field) in a homogeneous plasma. Chapter 5 presents model and analysis of plasma irregularities in magnetized plasmas (perpendicular to the magnetic field) in a homogeneous plasma. Chapter 6 addresses model and analysis of possible plasma irregularities in an inhomogeneous dusty plasma. Chapter 7 summarizes the possibility of each instability to produce radar echoes for future experiment and also will discuss critical parameter regimes for the next upcoming charged aerosol release experiment.

This research work has contributed to scientific knowledge of these aspects

1). Investigation of the physical mechanism for possible irregularities generated by charged aerosol release. Important aerosol parameter regimes are determined for guiding CARE experiment design, including dust injection speed and direction, dust particle size, dust density, and collisions;

2). Comparative analysis of typical characteristics and features for each instability. These analysis include wave frequency and wave growth rate, electron density fluctuation level, wave propagation direction and phase speed, bulk drift speed, and particle energization, which are important for ground radar diagnostics and in-situ measurements;

3). Development of dusty plasma models to explore nonlinear evolution (turbulence) of possible instabilities (saturation mechanism and saturation amplitude) for multiple scales problem, with the advantage of following nonlinear wave and particle interaction. These models primarily developed for space experiment application could also be applied to laboratory dusty plasma experiment.

Chapter 2

Simulation of Irregularities in Dusty Space Plasmas

Plasmas in the ionosphere can be treated with kinetic theory or fluid theory. Dust grains embedded in plasma are often considered as a complex plasma. Starting with definition of a dusty plasma, this chapter describes computational methods for simulating irregularities in dusty plasmas. A hybrid computational dusty plasma model will be described, including electron model, ion model, and dust model with a field model. Finally, numerical techniques are briefly explained.

2.1 Definition of a Dusty Plasma

A dusty plasma is defined as a electron-ion plasma with an additional charged component of micron- or submicron-sized particulate. Massive dust grains could be metallic, conducting, or made of ice particulate with a varying size, shape and particle charge. A plasma with dust particles can be termed differently based on characteristic lengths including the dust grain radius r_{d}, the average intergrain distance a, the plasma Debye radius λ_d and the dimension

of the dusty plasma. If $r_{\mathrm{d}} \ll \lambda_d < a$, it corresponds to a dust in plasma when charged dust particles are considered as a collection of isolated screened grains; while $r_{\mathrm{d}} \ll a < \lambda_d$, a dusty plasma is considered in which charged dust particles embraces the collective behavior [*Shukla and Mamum*, 2012].

This research work will treat dust grains with plasma as a dusty plasma, which corresponds to the regime $r_{\mathrm{d}} \ll a < \lambda_d$. In studies of dust collective behaviors, when $a << \lambda_d$, the dust grains can be treated as additional massive charged particles with dust grain charging process.

As a complex plasma, the presence of massive dust grains not only modifies the existing low frequency ion wave (e.g., ion acoustic waves (IA) and lower-hybrid waves (LH)) but also introduces new types of lower-frequency dust related waves (dust acoustic (DA) and dust ion acoustic (DIA)). These lower frequency dust waves have been observed and studied in laboratory dusty plasma facilities [*Merlino et al.*, 1998].

2.2 Governing Equations of Plasma

Kinetic plasma phenomena are described by the Vlasov Equation in the *mks* units of the International System (SI)

$$\frac{\partial f_{\mathrm{j}}}{\partial t} + \mathbf{v} \cdot \nabla f_{\mathrm{j}} + \frac{q_{\mathrm{j}}}{m_{\mathrm{j}}}(\mathbf{E} + \mathbf{v} \times \mathbf{B}) \cdot \frac{\partial f_{\mathrm{j}}}{\partial \mathbf{v}} = 0 \tag{2.1}$$

where $f_{\mathrm{j}}(\mathbf{x}, \mathbf{v})$ is the velocity distribution of the jth plasma species with charge q_{j} and mass m_{j}, and the electric field $\mathbf{E}$ and magnetic field $\mathbf{B}$ are given by Maxwell's equations with the sources terms from the moments of all plasma species. Note that the charge of the plasma species (q_{e}, q_{i}, q_{d})= (e, e, $\mathrm{Z_d}$e), where e is the unit electron charge and Z_{d} is the charge number on dust grains.

The Maxwell's equations are written in term of the velocity distribution as

$$\nabla \times \mathbf{E} = -\frac{\partial \mathbf{B}}{\partial t} \tag{2.2}$$

$$\nabla \times \mathbf{B} = \mu(\sum_{j=1}^{n} q_{\mathrm{j}} \int f_{\mathrm{j}} \mathbf{v} d\mathbf{v} + \epsilon \frac{\partial \mathbf{E}}{\partial t}) \tag{2.3}$$

$$\epsilon \nabla \cdot \mathbf{E} = \sum_{j=1}^{n} q_{\mathrm{j}} \int f_{\mathrm{j}} d\mathbf{v} \tag{2.4}$$

$$\nabla \cdot \mathbf{B} = 0 \tag{2.5}$$

where ϵ and μ is permittivity and permeability, respectively. In a plasma, $\epsilon \simeq \epsilon_0$ if all charge is regarded as free and $\mu \simeq \mu_0$, where the subscript 0 denotes quantity in vacuum. This set of equations could be solved by assuming that f_{j} could be represented by a number of macroparticles, N_{j}. The particle-in-cell (PIC) method is such a kinetic method adopted in this work. The charge and current density are collected on a spatial grid and the field equations are solved [*Birdsall and Langdon*, 1985]. The force on each particle is collected by interpolating values on the grid points near the neighboring grid cells. The set of equations could also be further simplified by fluid approximations and electrostatic field approximation depending on different applications.

Plasma dispersion is obtained by Fourier analyzing the Vlasov, Poisson and Maxwell's equations as described in previous section. Plasma dispersion in the form of the wave frequency ω and the wave vector $\mathbf{k}$ describes characteristics of plasma waves and plasma instabilities with the phase velocity $v_{\mathrm{p}} = \omega/k$ in a linear regime. In a dusty plasma, the properties of the electrostatic waves are determined from [*Shukla*, 2001]

$$\epsilon(\omega, \mathbf{k})\varphi = 0 \tag{2.6}$$

where φ is the wave potential and the dielectric constant ϵ is given by

$$\epsilon(\omega, \mathbf{k}) = 1 + \sum_{j=i,e,d} \chi_{\mathrm{s}} + \chi_{\mathrm{qe}} + \chi_{\mathrm{qi}} \tag{2.7}$$

where χ_{j} is the j species particle susceptibility, and χ_{qe} and χ_{qi} are the linear susceptibilities associated with the dust charge fluctuation dynamics.

The general dispersion relation of electrostatic waves in a dusty plasma without dust charge fluctuation is

$$1 + \sum_{j=i,e,d} \chi_{\mathrm{s}} = 0 \tag{2.8}$$

Plasma instabilities are associated with high frequency electron wave, low frequency ion wave and even lower frequency dust plasma waves. Waves can be categorized as electron, ion and dust waves, electrostatic and electromagnetic waves, hydrodynamic and kinetic waves. Also, waves can also be classified according to whether they propagate in an unmagnetized plasma or parallel, perpendicular, or oblique to the stationary magnetic field. Depending on plasma instabilities, approximations will be made for each plasma species, respectively, to handle instabilities with different time scale and spatial scale concerned.

2.3 Hybrid Computational Dusty Plasma Method

The complex nature of plasma instabilities has motivated considerable interest in computer simulations. Since linear analysis can not completely provide description of nonlinear evolution of plasma instabilities, kinetic computational methods are required to investigate nonlinear evolution of plasma instabilities. Computational simulation plays an important role in the development of plasma instability theory and also becomes an efficient design tool to provide accurate performance predictions for plasma instabilities.

Computational simulations of plasma comprise two general methods based on kinetic and fluid description. The kinetic method is achieved by solving numerically the plasma kinetic

equations (e.g., Vlasov or Fokker-Plank equations) or by particle-in-cell method. The fluid method proceeds by solving numerically the magnetohydrodynamic equations, primarily used for large scale simulation. The fluid theory is most appropriate for the length scale interested L much larger than the ion gyroradius r_{Li} and the time scale T larger than the inverse of the ion gyro period $\Omega_{\mathrm{ci}}^{-1}$. For scales larger than r_{Li} and $\Omega_{\mathrm{ci}}^{-1}$ but shorter than the fluid scales, the hybrid approach is most useful. For smaller scales, full particle is the best. For the particle simulation, if one is interested in long time scale but not spatial scales, a Boltzmann approximation can be made. And for very short time scale and spatial scale, the ion dynamics can be ignored too. The basic description of various electromagnetic hybrid algorithms can be found in the work by *Winske et al.* [2003].

The fluid theory is the simple description of a plasma but ignores the important wave and particle interaction. Full kinetic simulation using particle-in-cell requires high cost of computer resources. Therefore, the hybrid model has the advantage of including important kinetic effects with a reasonable computational cost. The hybrid method is properly used in this work that solves plasma irregularities on ion scales (ion gyro-radius and ion inertial spatial scales) and do not necessarily solve processes on electron scales (e. g., electron gyroradius and electron Debye length scales, inverse electron gyrofrequency and electron plasma frequency time scales). Plasma irregularities on the ion scale are readily resolved by satellite instrumentation and ground radar measurement.

2.3.1 Electron Model

In a hybrid model, electrons are treated by the fluid method

$$\frac{\partial n_{\mathrm{e}}}{\partial t} + \nabla \cdot (n_{\mathrm{e}} \mathbf{v}_{\mathrm{e}}) = \frac{dn_e}{dt}|_{\mathrm{charge}} + P_e + L_e \tag{2.9}$$

$$\frac{\partial \mathbf{v}_{\mathrm{e}}}{\partial t} + (\mathbf{v}_{\mathrm{e}} \cdot \nabla)\mathbf{v}_{\mathrm{e}} = \frac{q_{\mathrm{e}}}{m_{\mathrm{e}}}(\mathbf{E} + \mathbf{v}_{\mathrm{e}} \times \mathbf{B}) - \frac{k_{\mathrm{B}} T_{\mathrm{e}}}{m_{\mathrm{e}}} \frac{\nabla n_{\mathrm{e}}}{n_{\mathrm{e}}} - \nu_{\mathrm{en}}(\mathbf{v}_{\mathrm{e}} - \mathbf{v}_{\mathrm{n}}) \tag{2.10}$$

where

$$\frac{dn_e}{dt}|_{\mathrm{charge}} = -\frac{1}{q_e}\frac{d\rho_{de}}{dt} \tag{2.11}$$

and ρ_{de} is the dust charge density due to electron charging current collection, P_e and L_e is the production and loss of electrons due to photoionization and dissociative recombination. In the present work, P_e and L_e were ignored because the photoemission effect could become negligible in a night experiment. Here, n_α, $\mathbf{v}_\alpha$, T_α are the density, velocity, and temperature of charged species α, denoting electrons, ions and dust, respectively. Here q_α and m_α are the charge and mass of α species, and $\mathbf{E}$ and $\mathbf{B}$ are the electric field and magnetic field. And $\mathbf{v}_\mathrm{n}$ is the neutral gas velocity, k_B is Boltzmann's constant and ν_en is the electron and neutral collision frequency.

For electron dynamics in the plane parallel to the magnetic field, the electron velocity is governed by

$$\frac{\partial \mathbf{v}_e}{\partial t} + (\mathbf{v}_e \cdot \nabla)\mathbf{v}_e = \frac{q_e}{m_e}\mathbf{E} - \frac{k_\mathrm{B}T_e}{m_e}\frac{\nabla n_e}{n_e} - \nu_\mathrm{en}(\mathbf{v}_e - \mathbf{v}_n) \tag{2.12}$$

For electron dynamics in unmagnetized plasma or along the magnetic field, if the electron inertial is ignored, the Boltzmann equation can be derived using parallel momentum equation

$$n_\mathrm{e} = n_{\mathrm{e}0}\exp(-e\phi/k_B T_\mathrm{e}) \tag{2.13}$$

For electron dynamics in the plane perpendicular to the magnetic field $\mathbf{B} = B\hat{z}$, ignoring electron inertial and assuming strongly magnetized electron, the zero order electron velocity is

$$\mathbf{v}_\mathrm{e} = \mathbf{v}_\mathrm{E} = \frac{\mathbf{E}\times\mathbf{B}}{B^2} \tag{2.14}$$

With electron inertial included, the first order electron velocity is

$$\mathbf{v}_e = \mathbf{v}_E + \mathbf{v}_D - \frac{1}{B}\frac{\nu_\mathrm{en}}{\Omega_\mathrm{ce}}(\mathbf{E} + \vec{v}_\mathrm{n}\times\mathbf{B}) - \frac{k_\mathrm{B}T_\mathrm{e}}{eB}\frac{\nu_\mathrm{en}}{\Omega_\mathrm{ce}}\nabla\ln n_\mathrm{e} + \frac{1}{B\Omega_\mathrm{ce}}(\frac{\partial}{\partial t} + \mathbf{v}_{\mathrm{e}0}\cdot\nabla)\mathbf{E} \tag{2.15}$$

where the diamagnetic term

$$\mathbf{v}_\mathrm{D} = -\frac{k_\mathrm{B}T_\mathrm{e}}{eB}\hat{z}\times\nabla\ln n_\mathrm{e} \tag{2.16}$$

The variability of electron models provides several possible options to obtain electron density and electron velocity quantities: (i) using Boltzmann's assumption for electrons without solving continuity and momentum equation; (ii) solving continuity equation or using the quasi-neutrality condition for electron density with the velocity expression without solving the momentum equation; (iii) solving both continuity and momentum equation.

2.3.2 Ion Model

To be consistent with the Hybrid model, the ions and dust particle are treated kinetically with the standard particle-in-cell method. The jth particle with the mass m_j and the charge q_j can be treated as

$$\frac{d\mathbf{v}_j}{dt} = \frac{q_j}{m_j}(\mathbf{E} + \mathbf{v}_j \times \mathbf{B}) \tag{2.17}$$

$$\frac{d\mathbf{x}_j}{dt} = \mathbf{v}_j \tag{2.18}$$

The particle information is collected at the grid points to determine the plasma number density n_j, charge density $n_\mathrm{j}q_\mathrm{j}$, flow velocity $\mathbf{v}_j$ and current density $\mathbf{J}_j = n_\mathrm{j}q_\mathrm{j}\mathbf{v}_j$. The dust species accumulates the quantities to quantity of the ion species. It is noted that the charge q_j may vary with time for the dust species.

Ignoring the the production P_i and loss L_i of ions due to photoionization and dissociative recombination, the ion density loss due the ion charging current collection is

$$\frac{dn_i}{dt}|_{\mathrm{charge}} = -\frac{1}{q_i}\frac{d\rho_{di}}{dt} \tag{2.19}$$

and ρ_{di} is the dust charge density due to ion charging current collection. A Monte Carlo model is adopted to realize the ion charging current collection.

2.3.3 Dust Charging Model

The standard particle-in-cell PIC method is used to model the dynamics of the dust particles by integrating the Lorentz force equation. The dust particle is assumed to have uniform mass and a time variable charge $q_d = Q_\mathrm{d}$. The dust grains in a dusty plasma is assumed weakly coupled, where the charged dust microspheres cannot strongly interact with each other. In this case, the Coulomb coupling parameter $\Gamma_\mathrm{d} = Q_\mathrm{d}^2 \exp(-a/\lambda_d)/aT_\mathrm{d} << 1$, where λ_d is the Debye length. Electrons and ion currents are collected by a spherical grain. The time dependent charge on the dust is described with the orbit-limited motion OLM approach [*Chen*, 1965]

$$\frac{dQ_\mathrm{d}}{dt} = I_\mathrm{e} + I_\mathrm{i} + I_\mathrm{p} \tag{2.20}$$

where I_e and I_i are the electron and ion currents collected by the dust grain and I_p is the photoemission current. Assuming negatively charged dust, the electron and ion currents on the dust grain are given by

$$I_\mathrm{e} = \sqrt{8\pi} r_\mathrm{d}^2 q_\mathrm{e} n_\mathrm{e} v_\mathrm{e} \exp\left[\frac{-q_\mathrm{e}\phi_\mathrm{f}}{k_\mathrm{B}T_\mathrm{e}}\right] \tag{2.21}$$

$$I_\mathrm{i} = \sqrt{8\pi} r_\mathrm{d}^2 q_\mathrm{i} n_\mathrm{i} v_\mathrm{i} \left[1 - \frac{q_\mathrm{i}\phi_\mathrm{f}}{k_\mathrm{B}T_\mathrm{i}}\right] \tag{2.22}$$

$$I_\mathrm{p} = -\pi r_\mathrm{d}^2 q_\mathrm{e} J_\mathrm{p} Q_\mathrm{ab} Y_\mathrm{p} v_\mathrm{i} \left[\frac{q_\mathrm{e}\phi_\mathrm{f}}{k_\mathrm{B}T_\mathrm{p}}\right] \tag{2.23}$$

where $v_{e(i)}$ is the electron (ion) thermal velocity and ϕ_f the floating potential on the dust grain given by $\phi_\mathrm{f} = Q_\mathrm{d}(t)/C = Q_\mathrm{d}(t)/4\pi\epsilon_0 r_\mathrm{d}$, where C is the grain capacitance. The photoemission current may be important in the daytime that could be included as above. Also, J_p, Q_ab, Y_p and T_p are the photon flux, photon absorption efficiency, photoelectron yield, and average photoelectron temperature. It is noted that the ion current for dusty plasma with streaming velocity will be modified approximately by replacing the ion thermal velocity v_i with the ion thermal velocity and dust streaming velocity $\sqrt{v_\mathrm{i} + V_\mathrm{d}}$. The OLM approach has three major assumptions (i) the dust grain is isolated; (ii) electrons and ions

do not experience collisions when approaching to the grain; (iii) the barriers in the effective potential are absent [*Fortov et al.,* 2005]. Then the cross sections for electron and ion collection are determined from the laws of conservation of energy and angular momentum. It is valid to use the standard currents, since the dust radius size r_d (assumed no more than several microns) is much less than the electron cyclotron radius, (which is of the order of millimeters) [*Patacchini and Hutchinson*, 2007].

2.3.4 Field Model

For the field representation, the electrostatic approximation is made. The ionosphere is a low-beta ($\beta \ll 1$) plasma, where β is the ratio of plasma pressure to magnetic pressure. The magnetic field is large so that the magnetic field fluctuations ($\frac{\partial \mathbf{B}}{\partial t} = 0$) can be ignored at all frequencies. Based on the Faraday law $\nabla \times \mathbf{E} = 0$, the electric field can be written as $\mathbf{E} = -\nabla\phi$. Substituting into the Gauss law, Poisson's equation is obtained

$$\epsilon_0 \nabla^2 \phi = -\sum_{j=1}^{n} q_{\mathrm{j}} n_{\mathrm{j}} \tag{2.24}$$

where ϕ is the electrostatic potential.

1). Without assuming quasi-neutrality, the electrostatic potential ϕ is governed by Poisson's equation

$$\epsilon_0 \nabla^2 \phi = -(q_e n_e + q_i n_i + Q_d n_d) \tag{2.25}$$

For small perturbation in the electron density, the Poisson's equation is modified to include the magnetic effect

$$\epsilon_0 \nabla^2 \phi = -(\frac{1}{\omega_{pe}^2 + \Omega_{ce}^2})(q_e n_e + q_i n_i + Q_d n_d) \tag{2.26}$$

where the electric field can be calculated by $\mathbf{E} = -\nabla\phi$.

2). Assuming quasi-neutrality condition, the current density $\mathbf{J}$ continuity equation is

$$\nabla \cdot \mathbf{J} + \frac{\partial \rho}{\partial t} = 0 \ \text{ or } \ \nabla \cdot (\mathrm{n_e q_e \mathbf{v}_e}) - \epsilon_0 \nabla^2 \frac{\partial \phi}{\partial \mathrm{t}} = \nabla \cdot \Gamma_{\mathrm{i}} \tag{2.27}$$

where $\mathbf{J}$, ρ and Γ_{i} is the current density, the charge density and plasma density (e.g., ion and dust) calculated from particle-in-cell method. Electron quantities are given by fluid equations in Section 2.3.1 and the ion and dust quantities are obtained from the particle methods described in Section 2.3.2. The nonlinear potential equation describes the electric field with an inclination angle of magnetic field effect as derived in the reference [*Scales et al.*, 2012].

2.4 Numerical Techniques

2.4.1 Spectral Method

Spectral methods are used to numerically solve certain differential equations using Fourier series. Spectral methods as a global approach use basis functions that are nonzero over the whole domain with periodic geometry problems. Spectral methods were developed by *Steven Orszag* in 1969 and pseudospectral methods for highly nonlinear problems were proposed by *Steven Orszag* in 1972.

The Fourier Transform equations in a continuous domain are

$$H(k) = \int_{-\infty}^{\infty} h(x) e^{2\pi i k x} \, \mathrm{d}x \tag{2.28}$$

$$h(x) = \int_{-\infty}^{\infty} H(k) e^{-2\pi i k x} \, \mathrm{d}k \tag{2.29}$$

If a function sampled at evenly spaced and discrete time intervals Δx, a continuous function $h(x)$ with a bandwidth less than the Nyquist critical wavenumber $k_{\mathrm{c}} = 1/2\Delta x$ is completely determined by its samples h_{n} based on the sampling theorem. The function $h(x)$ is defined by the formula

$$h(x) = \Delta x \sum_{n=-\infty}^{\infty} h_{\mathrm{n}} \frac{\sin[2\pi k_{\mathrm{c}}(x - n\Delta x)]}{\pi(x - n\Delta x)} \tag{2.30}$$

where

$$h_{\mathrm{j}} = h(x_{\mathrm{j}}),\ x_{\mathrm{j}} = j\Delta x,\ j = 0, 1, 2, \cdots, N-1 \tag{2.31}$$

The Fourier transform of a discrete sample by a discrete sample sum is

$$H(k_{\mathrm{n}}) = \int_{-\infty}^{\infty} h(x) e^{2\pi i k x}\,\mathrm{d}x \simeq \sum_{j=0}^{N-1} h_{\mathrm{j}} e^{2\pi i k_{\mathrm{n}} x_{\mathrm{j}}} \Delta x = \Delta x \sum_{j=0}^{N-1} h_{\mathrm{j}} e^{\frac{2\pi i j n}{N}} \tag{2.32}$$

yielding the Discrete Fourier Transform (DFT) of the N points h_{j}, denoted by H_{n}

$$H_{\mathrm{n}} = \sum_{j=0}^{N-1} h_{\mathrm{j}} e^{\frac{2\pi i j n}{N}} \tag{2.33}$$

The inverse Discrete Fourier Transform is derived as

$$h_{\mathrm{j}} = \frac{1}{N} \sum_{n=0}^{N-1} H_{\mathrm{n}} e^{\frac{-2\pi i j n}{N}} \tag{2.34}$$

The N-point DFT has been solved by Fast Fourier Transform (FFT), which is a fast and commonly used algorithm. The derivation of FFT is beyond the scope of this thesis.

The differentiation of a function in Fourier space is expressed

$$\frac{dh}{d\mathbf{x}} = i\mathbf{k}h_{\mathbf{k}} \tag{2.35}$$

The first order derivative and Laplacian coefficient in a continuous domain $\mathbf{k}$ and k^2 are replaced by κ and K^2 given by *Birdsall and Langdon*, [1991]. As the grid becomes finer $k\Delta x \to 0$, the discrete results approach to the continuous results.

The convolution in Fourier space arises from x space products of functions $u(x)$ and $v(x)$ in nonlinear equations. This can be expressed as

$$\hat{w}_{\mathrm{k}} = \sum_{m+n=k} \hat{u}_{\mathrm{m}} \hat{v}_{\mathrm{n}} \tag{2.36}$$

A pseudospectral technique is used to solve the convolution, which converts convolution in the spatial domain into multiplication in the spectral domain. The pseudospectral technique

will be referred to the work by *Orszag* [1971a; 1971b]. In the spectral analysis, the Gibbs phenomenon frequently may occur from discontinuity and steep gradient. A proper filter is required to smooth the boundary by attenuating higher order Fourier coefficients. Some structure from the Gibbs phenomenon needs to be distinguished and dealt with properly. Spectral methods has the advantage of handling nonlinearities. When there is not spatial nonlinearities, the finite difference methods are chosen because of simplicity.

2.4.2 Time Integration Method

The ordinary differential equation is

$$\frac{dn}{dt} = f(n,t) \tag{2.37}$$

A Taylor series expansion of a function at a point could be expressed by

$$n(t_0+\Delta t) = n(t_0) + \frac{\Delta t}{1!}(\frac{dn}{dt})_{t_0} + \frac{\Delta t^2}{2!}(\frac{d^2n}{dt^2})_{t_0} + \text{h.o.t} \tag{2.38}$$

So the first derivative is approximated by

$$(\frac{dn}{dt})_{t_0} = f(n_0^t) \approx \frac{n(t_0+\Delta t) - n(t_0)}{\Delta_t} + \text{o}(\Delta t) \tag{2.39}$$

This is known as the forward-difference method, which is not stable. However, this method describes the basic idea of the time integration method. The time integration methods involve explicit and implicit methods, and the first-order, the second-order and higher orders (e.g., fourth order Runge-Kutta method). Here a second order Adams-Bashfourth-Moulton predictor-corrector method and Leapfrog method are explained here, which are adopted in our work.

A second-order predictor-corrector method is a combination of an explicit predictor formula and an implicit correction formula. The approach can be described as following

$$n^{t+*} = n^t + \Delta t f(n^t) \tag{2.40}$$

$$f(n^{t+*}) \tag{2.41}$$

$$n^{t+\Delta t} = n^t + \Delta t f(n^{t+*}) \tag{2.42}$$

$$f(n^{t+\Delta t}) \tag{2.43}$$

A second-order leapfrog method is commonly used for solving particle motion in particle-in-cell method. The approach can be described as following

$$n^+ = n^{t-\Delta t} + 2\Delta t f(n^t) \tag{2.44}$$

$$f(n^*) = \frac{1}{2}(f(n^t) + f(n^+)) \tag{2.45}$$

$$n^{t+\Delta t} = n^t + \Delta t f(n^*) \tag{2.46}$$

2.4.3 Newton Iteration

When the field equation is nonlinear, the solution is usually obtained by an iterative application for the solution of a related linear problem. A nonlinear differential equation for the potential equation is written as

$$N(\phi) = 0 \tag{2.47}$$

Assuming the potential change $\Delta\phi = \phi^{t+\Delta t} - \phi^t$ small, one can obtain

$$N(\phi^t + \Delta\phi) = N(\phi^t) + (\frac{\partial N}{\partial \phi})_t \Delta\phi + \text{h.o.t.} \tag{2.48}$$

using known operators N and its derivative.

The first-order Newton iteration scheme is

$$(\frac{\partial N}{\partial \phi})_t \Delta\phi = -N(\phi^t) \tag{2.49}$$

or

$$(\frac{\partial N}{\partial \phi})_t \phi^{t+1} = -N(\phi^t) + (\frac{\partial N}{\partial \phi})_t \phi^t \tag{2.50}$$

This scheme will be adopted in our work for the potential field equation. This algorithm and a derivation example can be found in *Hockney and Eastwood* [1981].

Chapter 3

Ion Acoustic Instability in an Unmagnetized Homogeneous Dusty Plasma

In this chapter, we will investigate the ion acoustic instability due to streaming charged dust. With introduction in section 3.1, linear analysis will be given in section 3.2 to describe the ion acoustic instability. In section 3.3, a two-dimensional electrostatic computational model will be given, which treats Boltzmann electrons and ions and dust as discrete particles. Computational results are described in detail in this section. Section 3.4 will discuss useful parameter regimes for upcoming space experiment and related experimental observations. Summary will be given in section 3.5.

3.1 Introduction

The purpose of the recent Charged Aerosol Release Experiment (CARE) [*Bernhardt*, 2009; *Bernhardt et al.*, 2011] was to generate artificially-created dust clouds near the F-peak of

the ionosphere. Plasma irregularities in a dusty plasma may contribute to explaining the generation mechanism for enhanced radar echoes. In this sounding rocket experiment, the injected chemical release contains both dust grains (Al_2O_3) and neutral gases (e.g., H_2O, HCl, CO). The aluminum oxide is expected to coagulate into micron sized negative charged dust particles, forming a charged dust beam with the drift velocity about $2 \sim 3$ km/s with respect to the ionosphere. The charged dust beam serves as the driving mechanism for possible ion instabilities leading to plasma irregularities, which is the subject of this chapter 3. It can be also argued that an ion beam may also potentially form due to charge exchange between molecular gas in the release and ambient O^+ ions in the ionosphere. This mechanism may also drive instabilities near the dust plasma frequency range which is the subject of next chapter.

Ion acoustic mode instabilities may occur due to either ions or dust drifting during various types of ionospheric modification experiments. One type is the ion acoustic instability in presence of dust (dust ion acoustic) in expanding ion clouds. *Melrose et al.* [1986] gives a condition for the ion acoustic instability $v_\mathrm{i} < c_\mathrm{s} < V_\mathrm{d} << v_\mathrm{e}$, where v_i, c_s, V_d, v_e is the ion thermal speed, the ion sound speed and the ion drift speed relative to the electrons and the electron thermal speed. In space shuttle experiments, it is considered that weakly damped ion acoustic waves excited by the charge exchange between exhaust molecular beams and background ions may be an important factor for enhanced radar backscatter [*Bernhardt et al.*, 1995]. Such an ion acoustic instability is considered to be due to the relative electron and ion drift. Recently, it was pointed out that the ion acoustic instability may be driven by the charged dust beam, even when the electron temperature is approximately equal the ion temperature. The presence of negatively charged dust actually weakens ion Landau damping [*Rosenberg et al.*, 2011].

At a much lower frequency, the second type of acoustic instability is the dust acoustic instability due to electron and ion drift relative to dust grains. A one-dimensional hybrid model [*Winske and Rosenberg*, 1998] was used to investigate the dust acoustic instability due to the ion drift, which also shows the ion-neutral and dust-neutral collision effect on the

wave growth rate of the instability.

In laboratory plasmas, both the dust ion acoustic instability and dust acoustic instability can be excited using an applied electric field in an unmagnetized plasma at the same time [*Merlino et al.*, 1997]. In addition to that, such ion acoustic instabilities, potentially driving weak double layers, also arouse great interest in auroral applications [*Sato and Okuda*, 1981; *Barnes et al.*, 1985].

3.2 Linear Analysis

The plasma model consists of electrons, singly charged ions, and streaming dust grains with charge $Q_{\rm d} = -Z_{\rm d}e$. The dust grains are negatively charged due to attaching more electrons than ions, which are assumed to be of identical size for simplicity. The charge neutrality condition is

$$n_{\rm i} - n_{\rm e} - Z_{\rm d} n_{\rm d} = 0 \tag{3.1}$$

where $n_{\rm s}$ is the number density of charged species s, denoting electrons, ions and dust, respectively.

The linear dispersion for waves with complex frequency $\omega = \omega_{\rm r} + i\gamma$ and wave vector $\mathbf{k}$ is defined in terms of the streaming direction $\hat{x}$, such that $\mathbf{k}\cdot\hat{x} = k\cos\theta$. Note θ is the angle off from the streaming direction. The dispersion for the ion acoustic instability in unmagnetized plasmas driven by the charged dust relative to the background plasma with velocity $V_{\rm d}$ in the $\hat{x}$ streaming direction is written

$$1 + \chi_{\rm e} + \chi_{\rm i} + \chi_{\rm d} = 0 \tag{3.2}$$

where

$$\chi_{\rm e} = \frac{1}{k^2\lambda_{\rm De}^2}[1 + \xi_{\rm e} Z(\xi_{\rm e})]$$

$$\chi_{\rm i} = \frac{1}{k^2\lambda_{\rm Di}^2}[1+\xi_{\rm i}Z(\xi_{\rm i})][1+\frac{i\nu_{\rm in}}{\sqrt{2}kv{\rm i}}Z(\chi_{\rm i})]^{-1}$$

$$\chi_{\rm d} = \frac{1}{k^2\lambda_{\rm Dd}^2}[1+\xi_{\rm d}Z(\xi_{\rm d})]$$

Here, $\lambda_{{\rm d}\alpha} = (n_\alpha Z_\alpha^2 e^2/\epsilon_0 k_{\rm B} T_\alpha)^{-1/2}$, $v_\alpha = (k_{\rm B}T_\alpha/m_\alpha)^{1/2}$, $\nu_{\alpha{\rm n}}$ are the Debye length, thermal speed, and collision frequency, T_α, m_α are temperature and mass, respectively, and Z is the plasma dispersion function. Note $\xi_{\rm e} = \omega/(\sqrt{2}kv_{\rm e})$, $\xi_{\rm i} = (\omega + i\nu_{\rm in})/(\sqrt{2}kv_{\rm i})$, $\xi_{\rm d} = (\omega - kV_{\rm d}\cos\theta)/(\sqrt{2}kv_{\rm d})$.

The dust-neutral collisions are neglected because the collision frequency is relatively small to affect the wave growth rate for such instability, however, the ion-neutral collisions are necessarily included, that is important for the ion acoustic instability in the sense of impacting the wave growth rate [*Rosenberg et al.*, 2011].

Here, consider the wave frequency near the ion plasma frequency $\omega_{\rm pi}$ and greater than the dust plasma frequency $\omega_{\rm pd}$ for cold ions and cold dust without any collision in the limit $\xi_{\rm e} << 1$, $\xi_{\rm i} >> 1$, $\xi_{\rm d} >> 1$, the dispersion relation can be simplified as

$$0 = 1 + \frac{1}{k^2\lambda_{\rm de}^2} - \frac{\omega_{\rm pi}^2}{\omega^2} - \frac{\omega_{\rm pd}^2}{(\omega - kV_{\rm d}cos\theta)^2} \tag{3.3}$$

These are unmagnetized collisionless electrons. But even if the electrons are magnetized and undergo collisions, the Boltzmann electrons are still valid assumptions in the limit of kinetic electrons with smaller electron Larmor radius compared to the wavelength. If electrons are magnetized and undergo collisions, the Boltzmann assumption is valid since the dominant wavelength ($\sim$ 12 cm from the dispersion calculation) along the magnetic field is smaller than the electron-neutral mean free path ($\sim$ 25 cm based on the neutral gas density in the plume from *Rosenberg et al.*, 2011) and the wavelength is larger than the electron Larmor radius ($\sim$ 1.5 cm using a geomagnetic field $B \sim 0.5$ G). Therefore, the electrons can shield the ion space charge quickly without being affected by electron-neutral collisions. The linear analysis for cold plasma dispersion provides guidance for the computational model to be considered in the next section.

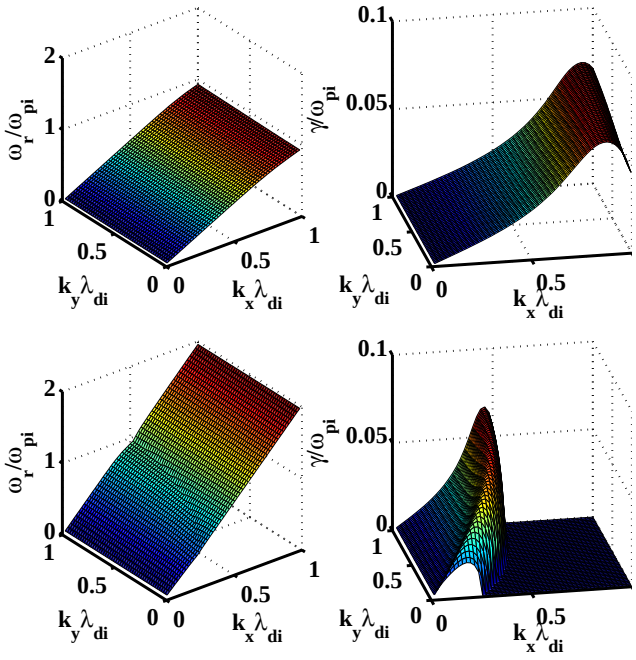

Figure 3.1: The dispersion and growth rate surfaces of ion acoustic instability for varying drift velocity $V_{\rm d}/v_{\rm i} = 1(top)$ and $V_{\rm d}/v_{\rm i} = 2(bottom)$. Other parameters are $T_{\rm e} = T_{\rm i} = T_{\rm d} = 0.1{\rm eV}, Z_{\rm d} = 200, n_{\rm d} = 0.0036 n_{\rm i}, m_{\rm d}/m_{\rm i} = 10^5$.

Considering the CARE experiment conducted in September 2009, the dispersion relation and growth rate is solved for parameters $V_{\rm d}/v_{\rm i} = 2, T_{\rm e} = T_{\rm i} = T_{\rm d} = 0.1\,{\rm eV}, Z_{\rm d} = 200, n_{\rm d} = 0.0036 n_{\rm i}, n_{\rm i} = 3 \times 10^{11}\,{\rm m}^{-3}, m_{\rm d}/m_{\rm i} = 10^5$ as shown in Figure 3.1. Except that the dust mass is artificially reduced to make simulation feasible (to be clarified later), this set of parameters may be considered representative of the artificial dust experiment injected into the ionosphere at about $\sim 280\,{\rm km}$ for the CARE experiment. As an example, the dust charge number equal to $Z_{\rm d} = 200$ corresponds to the dust radius approximately $r_{\rm d} \sim 0.8\,\mu{\rm m}$ [*Gosse et al.*, 2006; *Mueller and Kessler*, 1985]. The dust plasma frequency is $\omega_{\rm pd} \approx 0.038\omega_{\rm pi}$ in the case. The ion acoustic phase velocity $v_{\rm p}$ is estimated to be close to the ion acoustic sound speed by $C_{\rm s} \simeq (\sigma T_{\rm e}/m_{\rm i})^{1/2} \approx 1.8 v_{\rm i}$, where $\sigma = n_{\rm i}/n_{\rm e}$. For drift velocity $V_{\rm d}/v_{\rm i} = 1$, waves grow unstably at a relatively large wavenumber $k_{\rm x}$ range and smaller wavelength. The real frequency is less than ion plasma frequency. Note for $V_{\rm d}/v_{\rm i} = 2$, the most unstable modes from the linear analysis can exist at an angle off the streaming direction. The wave grows unstable rapidly in a certain range of wave vector $(k_{\rm x}, k_{\rm y})$ in this case, which implies important two dimensional behavior. The real frequency can be greater than the ion plasma frequency but smaller than about twice the ion plasma frequency for $V_{\rm d}/v_{\rm i} = 2$. Such characteristics are also true for higher drift velocities. It is should be noted that the dust grain to plasma ion mass ratio $m_{\rm d}/m_{\rm i}$ is on the order of 10^{10} in reality. As the dust to ion mass ratio increases, the maximum growth rate $\gamma/\omega_{\rm pi}$ actually decreases quantitatively from 10^{-1} to 10^{-3}. However, the characteristics of dispersion relation and growth rate surface do not change. Therefore, using a reduced mass ratio provides elucidation of the physics while allowing computational efficiency in such simulations [*Winske et al.*, 1995].

3.3 Computational Model and Results

In this section, a two-dimensional hybrid model is used to investigate the ion acoustic instability. Electrons as a charge neutralizing fluid are modeled as an isothermal Boltzmann relation, by assuming an adiabatic response for the electrons $n_{\rm e} = n_{\rm e0} \exp(-e\phi/k_{\rm B}T_{\rm e})$, which

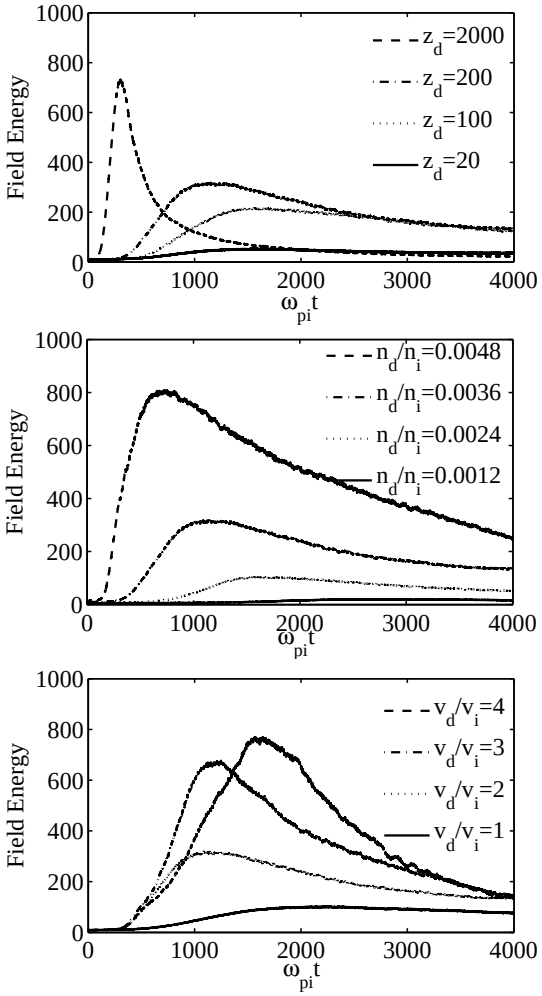

Figure 3.2: The energy history of the electrostatic waves (normalized) with varying parameters from the top: a) varying dust charge for $n_{\rm d}Z_{\rm d} = 0.72n_{\rm i}, V_{\rm d}/v_{\rm i} = 2$ b) varying dust density for $Z_{\rm d} = 200, V_{\rm d}/v_{\rm i} = 2$ while keeping $n_{\rm e0} > 0$ c) varying drift velocity for $n_{\rm d} = 0.0036n_{\rm i}, Z_{\rm d} = 200$.

gives the electron density as a function of electrostatic potential, where $k_{\rm B}$ is the Boltzmann constant and $n_{\rm e0}$ is obtained from the unperturbed qausi-neturality condition. The advantage for Boltzmann approximation is that the computation costs less in terms of increased time step by ignoring high electron plasma wave frequency. This Boltzmann approximation is also reasonable at the altitudes of interest where $\omega_{\rm pe}^2/\Omega_{\rm ce}^2 >> 1$ for studying nonlinear ion acoustic waves, where $\omega_{\rm pe}$ and $\Omega_{\rm ce}$ is electron plasma frequency and electron cyclotron frequency, respectively [*Barnes et al.*, 1985; *Karimabadi*, 1991;*Omidi and Akimoto*, 1988]. The Boltzmann assumption in an unmagnetized plasma is also possible to employ even for a magnetized plasma as long as the angle between the wavenumber vector of the electrostatic perturbation and the plane normal to the magnetic field is approximately larger than the the square root of the mass ratio of electrons to ions. Once the screening of charge for electrons as the dominant role is done, the electron obeys the Boltzmann law [*Tajima*, 1989].

The neutral dust particles injected from the rocket exhaust are assumed to charge to their equilibrium state in a much shorter time period than the wave growth period. The negatively charged dust is assumed to have fixed equilibrium dust charge number [*Winske et al.*, 1995]. The collisionless damping due to dust charging fluctuations is neglected here since the dust charge fluctuation damping rate β is less than the wave frequency, where $\beta = (I_{\rm e}/e)(n_{\rm d}/n_{\rm e}) \approx 10^{-1}\pi r_d^2 n_{\rm d} v_{\rm e}$, and $I_{\rm e}$ is electron current to the dust grain [*Jana et al.*, 1993].

Both dust and ions are modeled as discrete particles with the standard particle-in-cell PIC method [*Birdsall and Langdon*, 1991]. The full nonlinear Poisson's equation was solved for using the Newton iteration method [*Hockney and Eastwood*, 1981] combining with Successive Over relation Method.

The ion-neutral elastic scattering events are assumed to be hard sphere elastic collisions. A Monte Carlo Collision (MCC) model is used to treat ion and cold neutral collisions [*Birdsall*, 1991; *Vahedi*, 1994]. The collision probability for the i*th* particle is $P_{\rm i} = 1-\exp(-\Delta t \sigma_{\rm in} n_{\rm g} V_{\rm i})$, where $V_{\rm i}, \sigma_{\rm in}, n_{\rm g}$ is the velocity of particle, ion and neutral collision cross section and neutral gas density, respectively. A collision occurs when a uniformly distribution random number

on the interval [0 1] is less than the collision probability $P_{\rm i}$.

The simulation domain has $L_{\rm x} = 128\lambda_{\rm di}$ with 128 cells in length and $L_{\rm y} = 256\lambda_{\rm di}$ in width with 256 cells with both periodic boundary conditions. Based on the linear analysis, the unstable modes are well resolved into the simulation domain. In each grid cell $dx = dy = \lambda_{\rm di}$, there are 100 particles for each ion and dust species , respectively. The time step is chosen at $\omega_{\rm pi}\Delta t = 0.04$ in order to keep energy conversion and reduce noise level in the simulation.

Figure 3.2 shows the energy evolution of the electrostatic waves for varying dust charge number $Z_{\rm d}$, dust density $n_{\rm d}$ and dust expansion speed $V_{\rm d}$. The electrostatic wave energy is calculated by $\frac{1}{2}\int |\mathbf{E}|^2 dxdy$, where $\mathbf{E}$ is the electric field vector. The waves grow exponentially initially and saturate. Beyond the saturation time, the wave energy begins to damp due to wave-particle interactions. The streaming negatively charged dust is the source of free energy and starts to lose kinetic energy while the waves grow in the linear region and then begins to gain energy in the nonlinear process stage due to heating. The atomic oxygen ions O^+, continue to gain kinetic energy during the simulation due to heating. The growth rate is calculated from the mode energy for each case, which agrees well with the linear analysis result. In the CARE experiment, the dust size ranges from $\sim 100\,$nm to several μm, corresponding to dust charge number $Z_{\rm d}$ from 20 to 2000. As the dust charge increases and the dust density is reduced while keeping $n_{\rm d}Z_{\rm d} = 0.72$, we begin to see a higher growth rate for $Z_{\rm d} = 2000$, but the waves damp very rapidly after saturation. For the dust charge number $Z_{\rm d} = 20$, the ion acoustic instability becomes quite weak. Therefore the equilibrium dust charge, which depends on dust size, is a parameter of practical importance to be considered for strong excitation of the ion acoustic instability. To access the impact of variation of dust density, the dust charge number $Z_{\rm d}$ is held fixed at 200, and the expansion speed is taken to be equal to twice the ion thermal velocity. The electron percentage of course decreases as the dust density increases while keeping the equilibrium density $n_{\rm e0} \geq 0$. As the dust density increases, the wave field grows fast and tends to saturate at a higher level. When the dust density is of small percentage, the ion acoustic instability may be too weak to be observed. The dust density in the rocket exhaust does varying with time. The simulation covers the

dust density from $n_{\rm d}/n_{\rm i} \sim 0.0048$ to $n_{\rm d}/n_{\rm i} \sim 0.0012$ for the dust charge number $Z_{\rm d} = 200$, which corresponds to the maximum time $t \sim 0.5\,{\rm s}$ based on estimations by *Rosenberg et al.* [2011]. After the dust charges to its equilibrium state, the dust density for $n_{\rm d}/n_{\rm i} \sim 0.0036$ in the plume evolution corresponds to the real time $t \sim 0.2\,{\rm s}$. The dust density in the plume decreases with time, and if the dust density drops below a threshold, the instability may be too weak to be observed as shown in Figure 3.2. This maximum time in the simulation in terms of dust density is roughly estimated to be about $t \sim 0.5\,{\rm s}$. The dust drift velocity as another parameter is designed in the experiment on the order of the ion thermal velocity. As the drift velocity becomes larger than the ion acoustic sound speed $C_{\rm s}$, waves tend to propagate at a certain angle off the streaming direction, as will be shown later. The drift velocity $V_{\rm d}/v_{\rm i} = 3$ appears to be a particularly effective way in terms of extracting more dust kinetic energy into the electrostatic field energy with a higher wave growth rate and saturation level.

Figure 3.3 shows the temporal evolution of the electric field component $E_{\rm x}$, which is along the streaming direction, and also the electric field component $E_{\rm y}$ both at position $(x, y) = (64\lambda_{\rm di}, 128\lambda_{\rm di})$ on the simulation grid. The electric field component is normalized by $k_{\rm B}T_{\rm e}/e\lambda_{\rm di}$. In Figure 3.3, a noticeable feature is the bipolar $E_{\rm x}$ electric field component along the dust streaming direction $\hat{x}$. In the nonlinear stage, the spiky wave field is characterized with modulated wave packets in the $E_{\rm x}$ electric field time history. The spiky structure is clearly shown in the expanded views in Figure 3.3 and the waveform modulation period is related with the dust plasma period. Such a spiky waveform was explained by *Reddy et al.* [2002] , using an analytical model of the nearly parallel propagating waves to illustrate waveforms observed from the FAST satellite in the auroral region. Analytical results show that such waveforms develop from a current-driven instability and vary from a sinusoidal wave for low Mach number to sawtooth and highly spiky characteristics depending on the Mach number $M = v_{\rm p}/C_{\rm s}$, the driving field, and the bulk flow velocity. As the driving field and Mach number increases, the wave structure develops spiky characteristics. For the spiky parallel electric field waveform in Reddy's paper, a spectrum of spiky or bipolar electric field com-

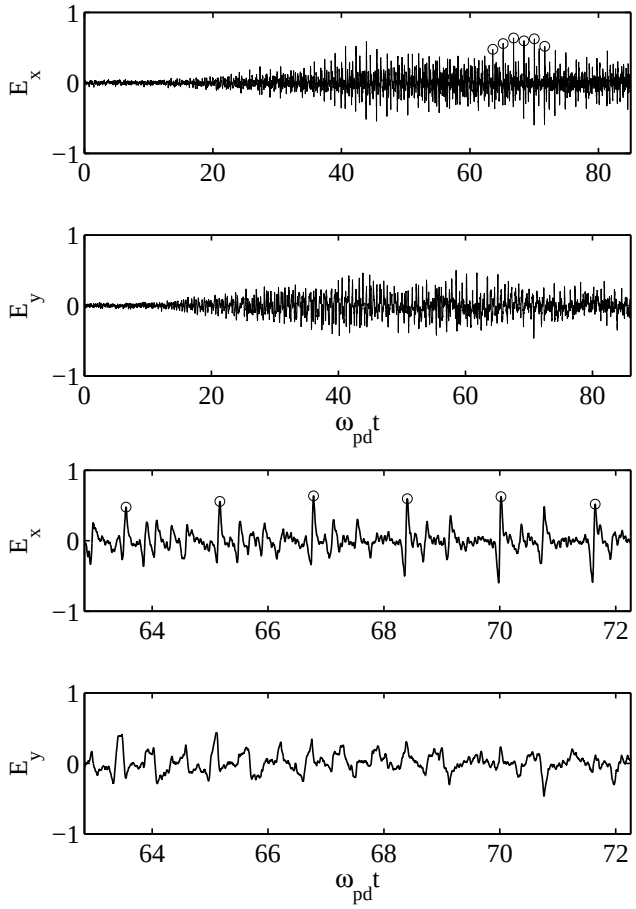

Figure 3.3: Temporal evolution of the electric field E_{x} and E_{y} (normalized by $k_{\mathrm{B}}T_{\mathrm{e}}/e\lambda_{\mathrm{di}}$) for $V_{\mathrm{d}}/v_{\mathrm{i}} = 3, Z_{\mathrm{d}} = 200, n_{\mathrm{d}} = 0.0036n_{\mathrm{i}}, m_{\mathrm{d}}/m_{\mathrm{i}} = 10^5, \nu_{\mathrm{in}}/\omega_{\mathrm{pi}} = 0$. Note the bipolar electric field E_{x} structure in the streaming direction and the bipolar structure period of the order of the dust plasma period where $\omega_{\mathrm{pd}} \approx 0.038\omega_{\mathrm{pi}}$.

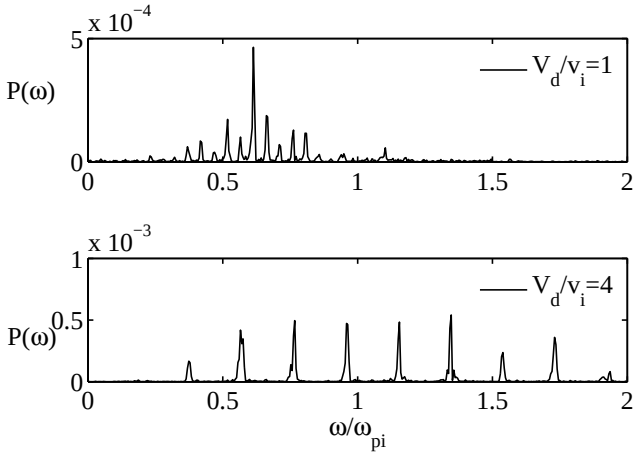

Figure 3.4: Frequency power spectrum $P(\omega)$ of the electric field $E_{\rm x}$ component for $V_{\rm d}/v_{\rm i} = 3, Z_{\rm d} = 200, n_{\rm d} = 0.0036 n_{\rm i}, m_{\rm d}/m_{\rm i} = 10^5, \nu_{\rm in}/\omega_{\rm pi} = 0$.

ponents exhibits a spiky frequency power spectrum. In other words, the time dependent electric field exhibits bipolar structure, leading to a spiky spectrum such as in Figure 3.4. It is true that the Fourier Transform of such spiky waves have an infinite number of harmonics and the phase and amplitude are dependent on the waveform of the original waves [*e.g.*, *Temerin et al.*, 1979].

In Figure 3.4, the frequency power spectrum is estimated by calculating the Fast Fourier Transform (FFT) using the time series of the field component $E_{\rm x}$ at a point $(x, y) = (64\lambda_{\rm di}, 128\lambda_{\rm di})$ for the period $15.2 \leq \omega_{\rm pd} t \leq 45.5$. The frequency power spectrum estimate is then $P(\omega) = |E_{\rm x}(\omega)|^2$. It is observed the power maximizes at several peaks near the ion plasma frequency. The frequency interval in the spectrum $\Delta\omega$ varies with drift velocity. For smaller drift velocity $V_{\rm d}/v_{\rm i} = 1$ in top panel of Figure 3.4, the frequency interval is about $\Delta\omega = 0.05\omega_{\rm pi}$, with most peaks located at frequency less than the ion plasma frequency. However, with the drift velocity increased to $V_{\rm d}/v_{\rm i} = 2 \sim 4$ in the bottom panel, the power spectrum maximizes at frequencies somewhat greater than the ion plasma frequency but smaller than twice the ion plasma frequency. This agrees with what linear analysis predicts, that is, the real frequency of such instability is greater than the ion plasma frequency

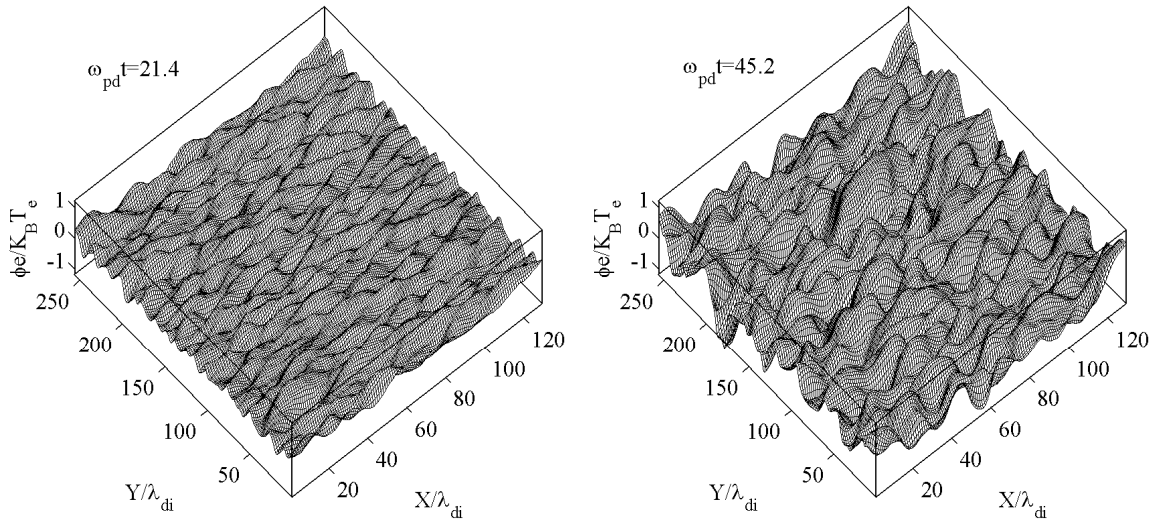

Figure 3.5: Electrostatic potential structure for the dust ion acoustic instability at $\omega_{\rm pd}t = 21.4$ and $\omega_{\rm pd}t = 45.2$ for parameters $V_{\rm d}/v_{\rm i} = 3, Z_{\rm d} = 200, n_{\rm d} = 0.0036n_{\rm i}, m_{\rm d}/m_{\rm i} = 10^5, \nu_{\rm in}/\omega_{\rm pi} = 0$.

but smaller than twice the ion plasma frequency in Figure 3.1. For $V_{\rm d}/v_{\rm i} = 4$, the power spectrum maximizes at frequency with interval increased to $\Delta\omega = 0.2\omega_{\rm pi}$.

The two-dimensional electrostatic potential $\phi(x, y)$ averaged over 100 iterations are shown at times $\omega_{\rm pd}t = 21.4$ and $\omega_{\rm pd}t = 45.2$ in Figure 3.5. The potential structure displays 2-D characteristics for such ion acoustic instability. Figure 3.6 shows the mode number spectrum by taking a two-dimensional FFT in spacial coordinates of $\phi(x, y)$, which results in $\phi(m_{\rm x}, m_{\rm y})$. The two-dimensional mode number power spectrum is $P(m_{\rm x}, m_{\rm y}) = |\phi(m_{\rm x}, m_{\rm y})|^2$. Note the relation for the wave number and the mode number is $k_{\rm x} = 2\pi m_{\rm x}/L_{\rm x}$ and $k_{\rm y} = 2\pi m_{\rm y}/L_{\rm y}$. At time $\omega_{\rm pd}t = 21.4$ in the linear growth stage, dominate modes, with larger growth rate, essentially exist at large angle with respect to the streaming direction as shown in Figure 3.6. The spectrum shows most unstable modes exist at an angle off the dust streaming direction, which on the other hand indicates the wave may propagate obliquely to the streaming direction. The strongest modes in the linear wave growth period are about at an angle $\theta = \arctan(k_{\rm y}/k_{\rm x}) \approx 50^o$. This can be explained by the resonance condition for such ion

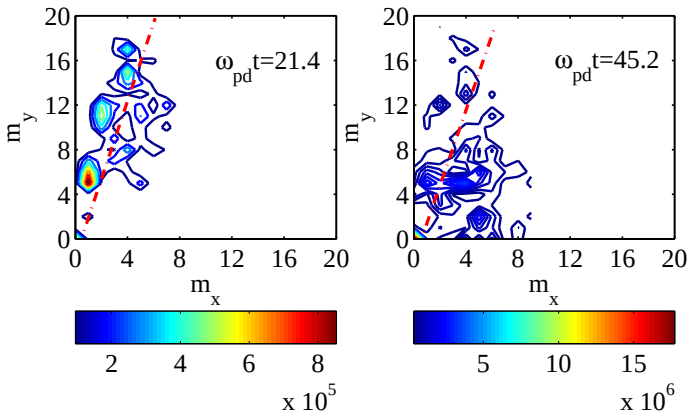

Figure 3.6: Mode number power spectrum $P(m_{\rm x}, m_{\rm y})$ of electrostatic potential at $\omega_{\rm pd}t = 21.4$ and $\omega_{\rm pd}t = 45.2$ for the same parameters as Figure 3.5.

acoustic instability proposed by *Rosenberg* [1996]. The dominant modes shown in Figure 3.6 correspond to modes with larger growth rate in the wave number space predicted by the linear analysis. In the later development of such instability, waves at smaller angles with respect to the streaming direction grow with a relatively smaller growth rate nonlinearly, which behaves similarly as the ion/ion acoustic instability [*Karimabadi et al.*, 1991]. The first set of growing modes still exist at time $\omega_{\rm pd}t = 45.2$ shown in the wave number power spectrum as such instability evolves, consequently, unstable modes becomes more spread in the nonlinear stage. Those modes in wave number spectrum are responsible for multiple peaks in the frequency spectrum.

The potential, ion density, dust density and dust in phase space at $y = 128\lambda_{\rm di}$ are shown from the top in each panel of Figure 3.7. Initially, the dust velocity is a drifting Maxwellian distribution with $V_{\rm d} = 3v_{\rm i}$. At early time $\omega_{\rm pd}t = 21.4$, the dust velocity in $v_{\rm x} - x$ phase space shows the onset of dust accelerating structure in the potential well. At time $\omega_{\rm pd}t = 45.2$, which is about the wave saturation time, the potential structure shows negative potential wells. The plasma density increases in these regions, which is true for both ion density and dust density. The dust becomes accelerated and thermalized by waves. When the electric field fluctuations become large as the waves grow, dust particles with smaller velocities

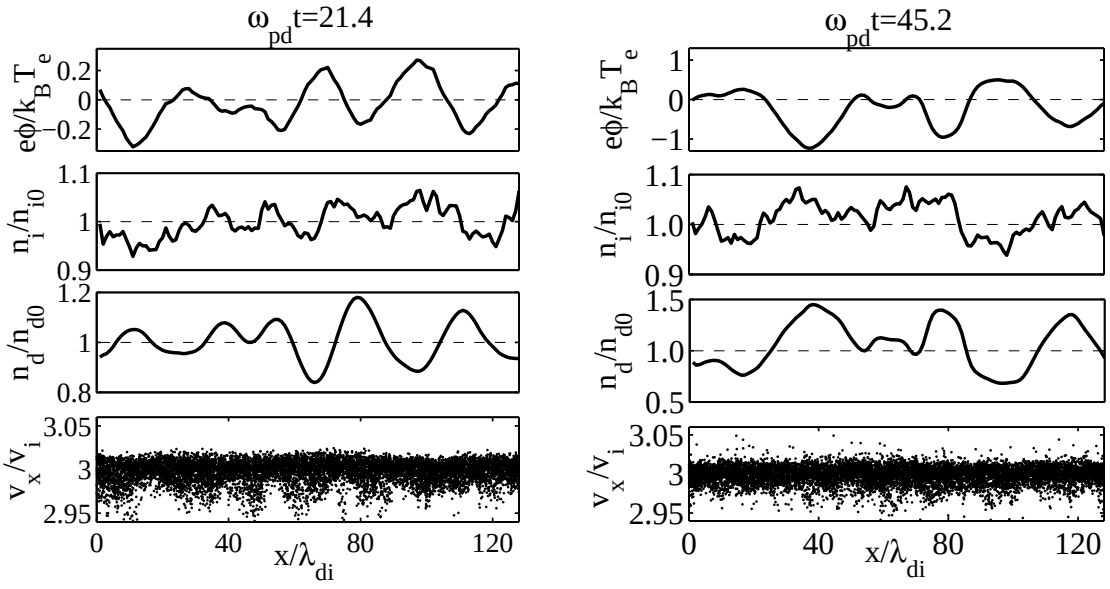

Figure 3.7: From the top, a) Potential, b) ion density, c) dust density and d) dust phase space at $\omega_{\rm pd}t = 21.4$ and $\omega_{\rm pd}t = 45.2$ for parameters $V_{\rm d}/v_{\rm i} = 3, Z_{\rm d} = 200, n_{\rm d} = 0.0036n_{\rm i}, m_{\rm d}/m_{\rm i} = 10^5, \nu_{\rm in}/\omega_{\rm pi} = 0$ for the same parameters as Figure 3.5.

relative to the wave phase velocity become accelerated by the wave potential. The trapping frequency is estimated to be about $\omega_{\rm T} = (ekE/m_{\rm d})^{1/2} \approx 0.2\omega_{\rm pd}$, where E is the electric field amplitude. The maximum acceleration of dust particle velocity from the drift velocity is about $\sim 0.03v_{\rm i}$ as shown in the dust velocity $v_{\rm x} - x$ phase space of Figure 3.7. However, since the dust is so heavy, the electrostatic potential($Z_{\rm d}e\phi/k_{\rm B}T_{\rm e} << 1$) is not sufficiently strong to fully trap the heavy dust particles.

To better understand the role of the wave and particle interaction in ion dynamics, the ion velocity distributions are shown in Figure 3.8 at different times. The velocity is normalized to the ion thermal velocity. In Figure 3.8, it is observed that the ions obtain a drift velocity in the streaming $\hat{x}$ direction that approaches the wave phase velocity and the relative drift between bulk ions and dust becomes smaller after nonlinear saturation. Also, the ion velocity distribution function shows a pronounced plateau near the phase velocity after the wave grows into the saturation phase in the $\hat{y}$ direction. It is clear that ions are bulk heated

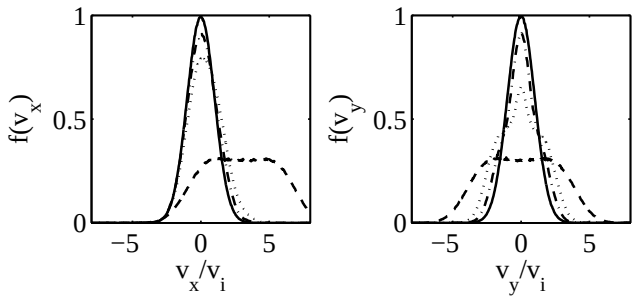

Figure 3.8: The ion velocity distribution function at times $\omega_{\rm pd}t = 0(solid), \omega_{\rm pd}t = 10.7(dot-dashed), \omega_{\rm pd}t = 14.5(dotted), \omega_{\rm pd}t = 88.6(dashed)$ for parameters $V_{\rm d}/v_{\rm i} = 3, Z_{\rm d} = 200, n_{\rm d} = 0.0036n_{\rm i}, m_{\rm d}/m_{\rm i} = 10^5, \nu_{\rm in}/\omega_{\rm pi} = 0$. Note ions develop a bulk drift in the streaming direction.

in both $\hat{x}$ and $\hat{y}$ direction due to the two-dimensional nonlinear wave-particle interaction. There is clearly no ion trapping structure.

As pointed above, ion-neutral collisions are an important factor for such an ion acoustic instability, so it is worthy to consider ion-neutral collisional effects. The ions and neutrals transfer momentum through an elastic scattering model here. The background ions will obtain the injected neutral gas speed in the collision process. The collision algorithm is described by [*Birdsall*, 1991; *Vahedi*, 1994] as following. The energy of the scattered ions is determined by $E_{\rm scat} = E_{\rm inc}\cos^2\chi$, where $E_{\rm inc}$ is the energy of the incident particle and χ is the scattering angle in the laboratory frame. Note $\cos^2\chi = 1 - \sin^2\chi; \sin^2\chi = 1/2(1-\cos 2\chi)$, where $2\chi = \Theta$ for equal masses, the center of mass scattering angle. Then $\cos\chi = \sqrt{1-R}$, where R is uniform random number $[-1, 1]$. The azimuthal scattering angle is determined uniformly by $\Phi = 2\pi R$. Note that no collision effects in the simulation have been included until this section.

There are two possible physical collision mechanisms between plasma ions and neutrals. One case is the collisions between the injected neutrals from the rocket exhaust, which serves to create the dust cloud, and background plasma ions. The physical situation is that the injected neutral gases moving with dust at approximately the same speed $V_{\rm g} = V_{\rm d}$ collide with background ions, in which neutral collisions with background ions play a role of reducing

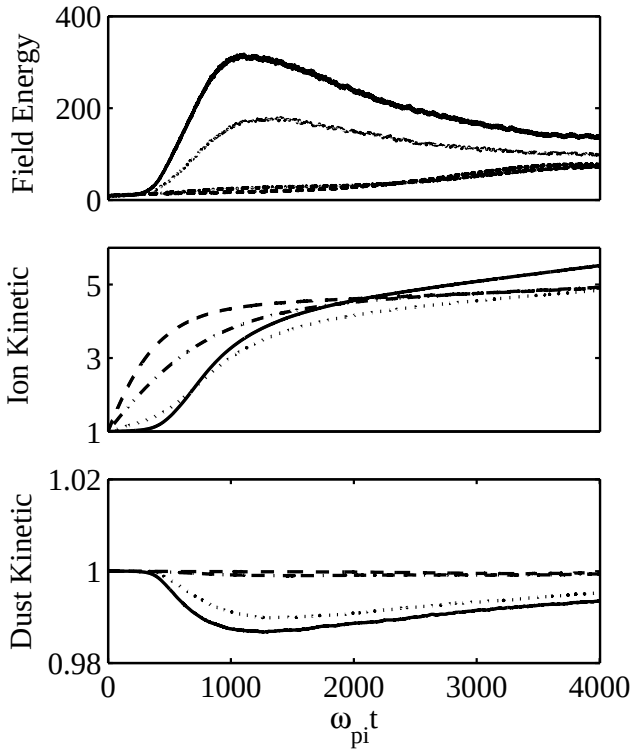

Figure 3.9: The energy histories of the electrostatic waves (normalized), the plasma kinetic ion energy, and the dust kinetic energy (normalized to its initial energy) with varying ion neutral collision frequency $\nu_{\rm in}/\omega_{\rm pi} = 0(solid), \nu_{\rm in}/\omega_{\rm pi} = 0.001(dot), \nu_{\rm in}/\omega_{\rm pi} = 0.005(dot - dashed), \nu_{\rm in}/\omega_{\rm pi} = 0.01(dashed)$ for parameters $V_{\rm d}/v_{\rm i} = 2, Z_{\rm d} = 200, n_{\rm d} = 0.0036 n_{\rm i}, m_{\rm d}/m_{\rm i} = 10^5$.

the relative drift between background ions and dust. The ion-neutral collisions are expected to reduce the growth rate of wave field because such collisions tend to transfer momentum from injected neutrals to background ions, weakening the relative drift velocity between injected dust and background ions. Another possible important mechanism is the collisions between the background stationary neutrals and background plasma ions. In this case, since collisions would not allow the ions to attain a drift in the direction of the moving dust, there may be a chance of enhancement of the instability since the relative drift between dust and ions is sustained.

As discussed by *Rosenberg et al.* [2011], considering the time scale $t \sim 1\,\mathrm{s}$ after release during the CARE experiment, the neutral gas density in the injected clouds may be an order of magnitude greater than the neutral gas density of the background atmosphere at about $\sim 250\,\mathrm{km}$. So, if we consider the time scale less than $\sim 1\,\mathrm{s}$, it is reasonable to assume that the former mechanism dominates the collision process since the injected neutral gas density is likely larger than the background ambient gas density. The role of the former collision mechanism is that ions acquire the neutral gas speed in a collision time scale. The ion and neutral collision frequency can be roughly estimated by $\nu_{\mathrm{in}} \approx \sigma_{\mathrm{in}} n_{\mathrm{g}} V_{\mathrm{d}}$ assuming the ion particle velocity is equal to the drift velocity $V_{\mathrm{i}} = V_{\mathrm{d}}$ although the velocity begins to change in the nonlinear wave stage. Assuming $\sigma_{\mathrm{in}} \sim 4 \times 10^{-15}\,\mathrm{cm}^2$, $V_{\mathrm{d}} = 2v_{\mathrm{i}} \sim 1.5\,\mathrm{km/s}$ and $n_{\mathrm{g}} \sim 1.2 \times 10^{12}\,\mathrm{cm}^{-3}$, then one obtains $\nu_{\mathrm{in}}/\omega_{\mathrm{pi}} \sim 0.004$ at time $t \sim 0.2\,\mathrm{s}$, which corresponds to $n_{\mathrm{d}}/n_{\mathrm{i}} \sim 0.0036$. After time $t \sim 1\,\mathrm{s}$, the dust density decreases substantially and on the other hand the second collision mechanism still plays a negligible role for a small collision frequency $\nu_{\mathrm{in}}/\omega_{\mathrm{pi}} \sim 0.0001$. Figure 3.9 shows the energy histories with varying collision frequencies. In the cases with $\nu_{\mathrm{in}}/\omega_{\mathrm{pi}} = 0.01$ and 0.005, the relative drift velocity between ions and dust becomes small quickly as shown in Figure 3.9 (middle panel) before the wave begins to grow. Ions gain momentum by the ion-neutral collision process quickly to the velocity of the neutral gas speed and the dust of the same drift velocity cannot transfer its kinetic energy to generate electrostatic waves with relative smaller velocity. If we consider the case with a relatively smaller value of collision frequency $\nu/\omega_{\mathrm{pi}} = 0.001$, which is less than the growth rate of the instability, it is noted that the instability continues still but the growth rate and saturation level of waves is decreased compared to that without collisions. In this case, the wave-particle interactions exceed the ion-neutral collisions. The ion heating level is maintained mainly due to wave-particle interaction. It is true that the sufficiently large ion-neutral collision will quench such instability. Therefore, it is important that the ion-neutral collision frequency should be less than the growth rate in order to excite ion acoustic waves. Also, the drift velocity between dust and ions is required to be large enough for the instability to develop. If the background and neutral collisions are sufficiently strong

in the ionosphere, the dust drift velocity and dust charge and density will serve as critical parameters for such an IA instability.

3.4 Discussion of Applications

With applications for active space experiments which release aerosol or dust clouds in the earths upper atmosphere. Specific characteristics for the recent Charged Aerosol Release experiment have been considered. Incoherent ion-acoustic waves with a broad k spectrum are observed in the simulation. The wave structure scale is about $\sim 30\lambda_{\rm di}$, the frequency is near the ion plasma frequency. Since this instability is quite strong, it is important to determine plasma parameters, which may guide design in the future experiments. The model also shows the nonlinear evolution of the system. In the early time of such instability, waves may initially propagate off the streaming direction when the drift velocity is greater than a critical drift velocity, which becomes quite obvious for the drift velocity $V_{\rm d} = 3v_{\rm i}$ and even larger. The dominant modes concentrate in a narrow region of the wave number spectrum, which indicates oblique propagation with respect to the dust streaming direction. We have performed a parameter study, including equilibrium dust charge, dust density, the dust drift velocity, on such ion acoustic instability. At a nonlinear stage, a more broad k spectrum is observed. The potential structure tends to show a net negative drop in this stage, that correlated with enhanced plasma density. Such instability can heat ions and dust through wave-particle interactions. Dust undergoes interaction with excited waves with acceleration by the potential wells while the bulk of plasma ions attains a drift near the wave phase velocity such that the relative drift between dust and plasma ions decreases.

The ion acoustic instability, that displays the spiky wave structure and waveform modulation observed in this simulation, may be similar in structure to auroral observations to some extent. *Mozer et al.* [1997] have observed the bipolar spiky parallel electric field structure and wave envelopes of parallel electric field in the auroral acceleration region based on Polar

Satellite data. The FAST satellite also observed the feature of spiky parallel electric field waveform and *Ergun et al.* [1998] has explained the solitary characteristic in supporting such parallel electric field. The recent analysis by *Reddy* [2002] explained the parallel electric field structure observed by Polar experiment, that shows the spiky waveform structure for ion acoustic waves. The upcoming CARE experiment will have the capability of in-situ measurements for the temporal behaviors of such electric field structures and additional VHF and UHF ground radars will be used for more comprehensive diagnostics as well.

3.5 Summary

A two-dimensional model is used to investigate the ion acoustic instability driven by streaming charged dust to understand the generation and the nonlinear evolution of electrostatic waves during active space experiments in which artificial aerosol clouds are created in the ionosphere. In the model, the plasma background ions and charged dust are treated as discrete particles while electrons are dealt with as a Boltzmann fluid. A Monte Carlo Collision (MCC) model is adopted to deal with the ion and neutral collisions. The simulation results show that the ion acoustic waves initially grow and propagate obliquely to the streaming direction with maximum growth. Nonlinear evolution shows saturation by acceleration of dust particles, background ion heating, and development of an ion bulk drift in the dust streaming direction. Spiky bipolar electric field field structures are also observed that are characteristics of ion acoustic-type waves observed during other space experiments. Important parameters of the dust cloud that impact the evolution of the waves are discussed.

Chapter 4

Dust Acoustic Instability in an Unmagnetized Homogeneous Dusty Plasma

In this chapter, we will investigate the dust acoustic instability due to an ion beam in an unmagnetized dusty plasma. With introduction section 4.1, linear analysis in section 4.2 will be given to describe the dust acoustic instability. A two-dimensional electrostatic computational model and results will be described similarly in section 4.3 as in Chapter 2. Section 4.4 will discuss useful parameter regimes for upcoming space experiment and related experimental observations. Summary will be given in section 4.5.

4.1 Introduction

Recently, an ionospheric sounding rocket experiment was performed in a controlled way to investigate the plasma irregularities in upper atmospheric dust layers [*Bernhardt*, 2009]. The Charged Aerosol Release Experiment (CARE) uses a rocket payload injection of particles

in the ionosphere to determine the mechanisms for enhanced radar scatter from plasma irregularities embedded in artificial dusty plasma in space. A dusty plasma environment is established when aluminum oxide dust grains accumulate background electrons and ions during the charging process. Charge exchange between the ambient ionospheric O^+ ions at about 280 km and exhaust neutral moleculars also yields an ion beam with relative drift to the dusty plasma environment [*Bernhardt et al.*, 1995; *Bernhardt et al.,* 2011]. The application of the dust acoustic instabilities driven by the ion beam by the CARE experiment in the ionosphere is the objective of this investigation. Another potential application of this instability may involve the planetary ring system of Saturn as discussed by *Winske and Rosenberg,* [1998].

Rosenberg [1993] theoretically analyzed that the dust acoustic instabilities could be generated by either electron or ion beam and meanwhile gave the dispersion for such dust acoustic instabilities. The analysis was provided for such dust acoustic instability driven by the ion beam using a one-dimensional model [*Winske and Rosenberg,* 1998; *Winske et al.*, 1995]. The two-dimensional nature of the ion-dust streaming instability was shown theoretically [*Rosenberg*, 1996]. Such a dust acoustic instability may actually propagate off the streaming direction. Dust density waves, similarly dust acoustic waves, which propagate at an oblique angle with respect to the ion streaming direction were observed by experiments [*Piel et al.,* 2006]. They were also theoretically analyzed for the drifting velocity effect on the angular distribution of unstable modes and the quenching of the instability by increasing the gas pressure [*Piel et al.,* 2008]. Also, nonlinear behavior of a Hall current instability of dust-acoustic type waves [*Rosenberg and Shukla*, 2000] has been investigated by a two-dimensional model [*Scales and Chae*, 2003; *Scales*, 2004a]. In this sense, a one-dimensional model cannot fully provide the information about such a dust acoustic instability.

In this chapter, a two-dimensional computational model is adopted to simulate the dust acoustic instability in unmagnetized plasmas for a broad range of parameters. The plasma background ions and charged dust are treated as discrete particles while electrons are dealt with as a Boltzmann fluid. The Boltzmann fluid assumption shows its advantage in terms

of simulating the ion/ion acoustic instability [*Karimabadi et al.,* 1991] to explain the observations of electrostatic waves in a variety of regions of space, such as the AMPTE releases in the solar wind [*Omidi et al.,* 1988]. In order to investigate the parameter regime for such a dust acoustic instability, the kinetic dispersion relation is numerically solved and several parameters are investigated including the equilibrium dust charge, dust density and the drift velocity, which clearly embraces two-dimensional characteristics. For a broad range of drift velocities, the simulation result shows the significantly different behavior from the one-dimensional model that the most unstable waves may propagate at an angle far off the streaming direction. The role of the ion and neutral collision damps the wave growth and may potentially lead to unstable waves propagating even further off the streaming direction.

4.2 Linear Analysis

The plasma model consists of electrons, singly charged streaming ions, and dust grains with charge $Q_{\rm d} = -Z_{\rm d}e$. The dust grains are assumed to be of identical size for simplicity. The charge neutrality condition is

$$n_{\rm i} - n_{\rm e} - Z_{\rm d} n_{\rm d} = 0 \tag{4.1}$$

where n_α is the number density of charged species α, denoting electrons, ions and dust, respectively.

The linear dispersion for waves with frequency ω and wave vector $\mathbf{B}$ is defined in terms of the streaming direction $\hat{x}$, such that $\mathbf{k} \cdot \hat{x} = k \cos\theta$. Note θ is the angle away from the streaming direction. The dispersion for the dust acoustic instability in unmagnetized plasmas driven by the ion beam relative to the background plasma with velocity $V_{\rm d}$ is written

$$1 + \chi_{\rm e} + \chi_{\rm i} + \chi_{\rm d} = 0 \tag{4.2}$$

where

$$\chi_{\rm e} = \frac{1}{k^2\lambda_{\rm De}^2}[1 + \xi_{\rm e} Z(\xi_{\rm e})] \tag{4.3}$$

$$\chi_{\rm i} = \frac{1}{k^2\lambda_{\rm Di}^2}[1 + \xi_{\rm i} Z(\xi_{\rm i})][1 + \frac{i\nu_{\rm in}}{\sqrt{2}kv_{\rm i}} Z(\xi_{\rm i})]^{-1} \tag{4.4}$$

$$\chi_{\rm d} = \frac{1}{k^2\lambda_{\rm Dd}^2}[1 + \xi_{\rm d} Z(\xi_{\rm d})] \tag{4.5}$$

Here, $\xi_{\rm e} = \omega/\sqrt{2}kv_{\rm e}, \xi_{\rm i} = \omega - kV_{\rm d}cos\theta + i\nu_{\rm in}/\sqrt{2}kv_{\rm i}, \xi_{\rm d} = \omega/\sqrt{2}kv_{\rm d}$.

These are unmagnetized collisionless electrons. But even if the electrons are magnetized and undergo collisions, the Boltzmann electrons are still valid assumptions in the limit of kinetic electrons with smaller electron Larmor radius compared to the wavelength and electron neutral collision mean free path. Therefore, the electrons can shield the ion space charge quickly without being affected by electro-neutral collisions. Consider the regime for the dust acoustic phase velocity $v_{\rm p}$ satisfying $v_{\rm d} << v_{\rm p} < v_{\rm i} << v_{\rm e}$, so we approximately obtain $\chi_{\rm e} = 1/k^2\lambda_{\rm De}^2$ and $\chi_{\rm d} = -\omega_{\rm pd}^2/\omega^2$ in the regime for $\chi_{\rm e} << 1$ and $\chi_{\rm d} >> 1$. The ion susceptibility is not simplified. The kinetic dispersion relation is solved in the frame where the dust is stationary and ions are drifting with $V_{\rm d} = 2 \sim 3v_{\rm i}$. Electrons are assumed at rest relative to the dust since the thermal velocity is greater than the ion drift velocity.

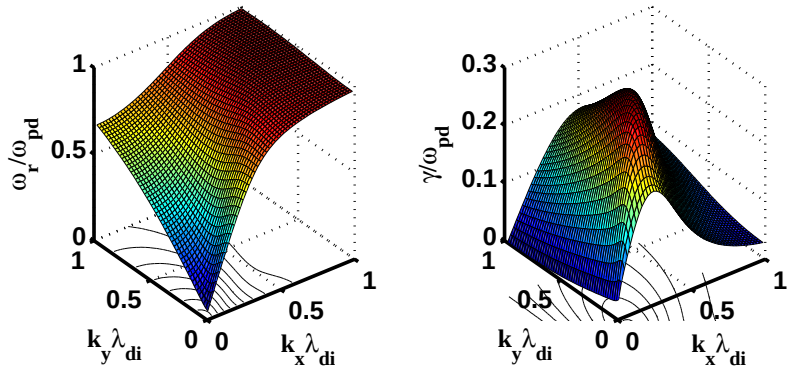

Figure 4.1: Dust acoustic instability dispersion relation (left) and growth rate (right) for parameters $V_{\rm d}/v_{\rm i} = 3, T_{\rm e} = T_{\rm i} = T_{\rm d} = 0.1{\rm eV}, Z_{\rm d} = 2400, n_{\rm d} = 0.0003n_{\rm i}, m_{\rm d}/m_{\rm i} = 10^5$.

The real frequency of the dust acoustic wave may be approximated for cold dust by the

expression $\omega = k\lambda_{\rm d}\omega_{\rm pd}/(1+k^2\lambda_{\rm D}^2)^{1/2}$, where $\lambda_{\rm D}^{-1} = (\lambda_{\rm Di}^{-2} + \lambda_{\rm De}^{-2})^{1/2}$ [*Rao et al.,* 1990]. The dust acoustic speed is written as $c_{\rm DA} = (k_{\rm B}T_{\rm d}/m_{\rm d}) + (n_{\rm d0}/n_{\rm i0}Z_{\rm d}^2)(k_{\rm B}T_{\rm i}/m_{\rm d})[1/(1+\delta T_{\rm i}/T_{\rm e})]$ [*Merlino*, 1998], ignoring the electron and the ion inertia, where $\delta = n_{\rm i0}/n_{\rm e0} = 1 + Z_{\rm d}n_{\rm d0}/n_{\rm e0}$, where $n_{\rm e0}$, $n_{\rm i0}$ and $n_{\rm d0}$ are the unperturbed equilibrium density. The analytical form of the growth rate is similar to that of a Buneman type instability, which may be written in the form $\gamma = (\sqrt{3}/2^{4/3})(1\sqrt{A})(\omega_{\rm pi}/\omega_{\rm pd})^{1/3}$, where $A = 1 + 1/k^2\lambda_{\rm De}^2$ [*Rosenberg*, 1996].

The dispersion relation and growth rate is solved numerically as shown in Figure 4.1 based on the parameters $V_{\rm d}/v_{\rm i} = 3$, $T_{\rm e} = T_{\rm i} = T_{\rm d} = 0.1\,{\rm eV}$, $Z_{\rm d} = 2400$, $n_{\rm d} = 0.0003n_{\rm i}$, $m_{\rm d}/m_{\rm i} = 10^5$. During the CARE experiment, the aluminum oxide particulates varies in the 100 nm to 10 micron size range with a peak in the size distribution at 1 micron [*Bernhardt et al.,* 2011]. The dust charge $Z_{\rm d} = 2400$ corresponds to a dust grain radius of 10 μm. The two-dimensional dispersion and growth rate calculation are qualitatively the same for $Z_{\rm d} = 2400$ and $Z_{\rm d} = 200$ except for the maximum value of growth rate as will shown in Figure 4.2. Without losing two-dimensional characteristics, we choose the maximum dust grain radius for $Z_{\rm d} = 2400$ with a larger wave growth rate to save computational time. Note the drift velocity here is $V_{\rm d}/v_{\rm i} = 3$, and shows the growth rate maximizes at an angle θ about 45^o with respect to the stream direction. When the drift velocity is increased to $V_{\rm d}/v_{\rm i} = 4$, the growth rate is becoming quite small in the streaming direction.

The relationship between the ion drift velocity and the angle θ corresponding to the growth rate maximized over wavenumber $(k_{\rm x}, k_{\rm y})$ is given in Figure 4.2. Three sets of parameters are chosen with varying the dust density and charge whereas keeping the dust charge density $n_{\rm d}Z_{\rm d} = 0.72n_{\rm i}$ constant. The dust charge $Z_{\rm d}$ as another parameter that affects the wave growth rate. As the dust charge increases while keeping $n_{\rm d}Z_{\rm d}$ constant, the phase velocity of the dust acoustic wave increases and is approximately proportional to $\sqrt{n_{\rm d}Z_{\rm d}^2}$. The dust Landau damping reduces since the phase velocity of dust acoustic wave increases. Note the modified ion acoustic speed is then $c_{\rm s} = \sqrt{\delta k_{\rm B}T_{\rm e}/m_{\rm i}} \simeq 1.9v_{\rm i}$. In Figure 4.2, it all shows that when the ion drift velocity $V_{\rm d}/v_{\rm i}$ is greater than approximately 2.0 near the ion acoustic speed $c_{\rm s}$, the most unstable wave may propagate obliquely with respect to the streaming

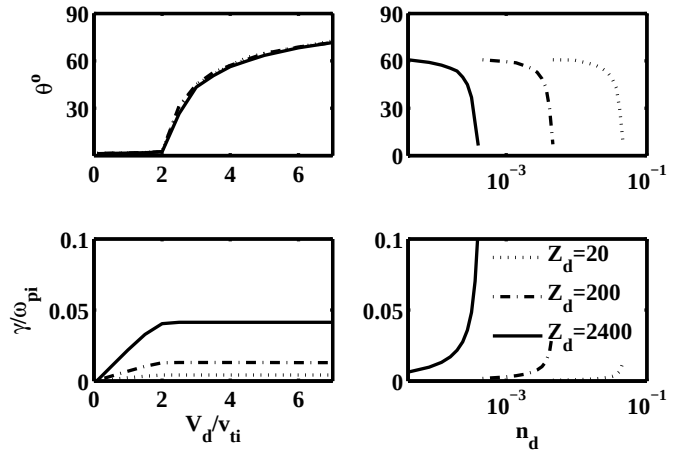

Figure 4.2: a)(left) Drift velocity effect on the growth rate (normalized to $\omega_{\rm pi}$) and the wave propagation angle to the streaming direction maximized over the wavevector $(k_{\rm x}, k_{\rm y})$ space without any collisions b) (Right) Dust density effect (normalized to $n_{\rm i}$, keeping $n_{\rm e} > 0$) on the growth rate and the wave propagation angle to the streaming direction maximized over the wavevector $(k_{\rm x}, k_{\rm y})$ space with the drift velocity $V_{\rm d}/v_{\rm i} = 3$.

direction. It is discussed by *Piel et al.*, [2008] that for dust density waves when the drift velocity approaches the Bohm velocity $v_{_{\rm b}} = \sqrt{k_{\rm B}T_{_{\rm e}}/m_{_{\rm i}}}$, the fastest growing modes will propagate obliquely. It can be explained by the resonance condition to some extent. The resonance condition for the Buneman type dust acoustic instability driven by the ion drift speed $V_{\rm d} >> v_{\rm i}$ is $\mathbf{k}\cdot\hat{x} = \omega_{\rm pi}/\sqrt{A}$, which can be further written $k^2\lambda_{\rm Di}^2 = {v_{\rm i}}^2/V_{\rm d}^2\cos^2\theta - T_{\rm i}/\delta T_{\rm e}$ [*Rosenberg*, 1996]. As the drift velocity increases, the angle needs to be increased to satisfy this condition. When the drift velocity is increased, the angle between the wave vector $\mathbf{k}$ and the drift velocity direction $\mathbf{x}$ is increased as seen in Figure 4.1 and Figure 4.2. When the ion beam becomes a supersonic flow, the maximum growth rates level off.

To show the role of the dust charge density on the waves, a broad range of varying dust density is studied as shown in Figure 4.2 with three cases of dust equilibrium charges. The growth rate increases a small amount with increasing dust density before the electron density constitutes a relatively small percentage of the ion density. Consider the limit, when the

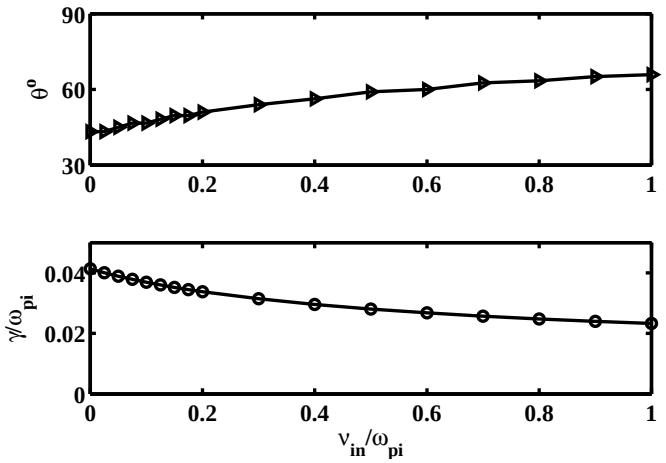

Figure 4.3: Growth rate maximized over the wave vector space $(k_{\rm x}, k_{\rm y})$ and the wave propagation angle as a function of ion-neutral collision frequency for parameters: $V_{\rm d}/v_{\rm i} = 3, T_{\rm e} = T_{\rm i} = T_{\rm d} = 0.1{\rm eV}, Z_{\rm d} = 2400, n_{\rm d} = 0.0003 n_{\rm i}, m_{\rm d}/m_{\rm i} = 10^5$.

electron density approaches zero, only positive ions and negatively charged dust exist in the system, and the growth rate increases significantly. The wave propagation angle changes rapidly and waves tend to propagate more parallel to the ion streaming direction. The results may indicate that the electron concentration plays an important role in determining both the wave propagation direction and the wave growth rate. From the resonance condition, when $\delta \to \infty$, the screening effect of the electrons disappears in the mode dispersion. The resonance condition can be easily satisfied even for smaller angle θ .

The ion-neutral collisions are thought to lead to additional damping effects in this regime [*Winske et al.,* 1995; *Rosenberg*, 1996]. In order to show the ion-neutral collision effect, we choose the case for $V_{\rm d}/v_{\rm i} = 3$, corresponding to waves which propagate at an angle about 45^o off the streaming direction. The growth rate decreases as the ion-neutral collision increases as the ion neutral collisions reduce the wave growth shown in Figure 4.3. It is also noted that the wave propagation angle increased if the ion and neutral collision frequency is increased. The dust and neutral collisions also affect the wave growth, but the dust-neutral effect is ignored, since it has minor effect on the waves we are concerned about for the CARE project.

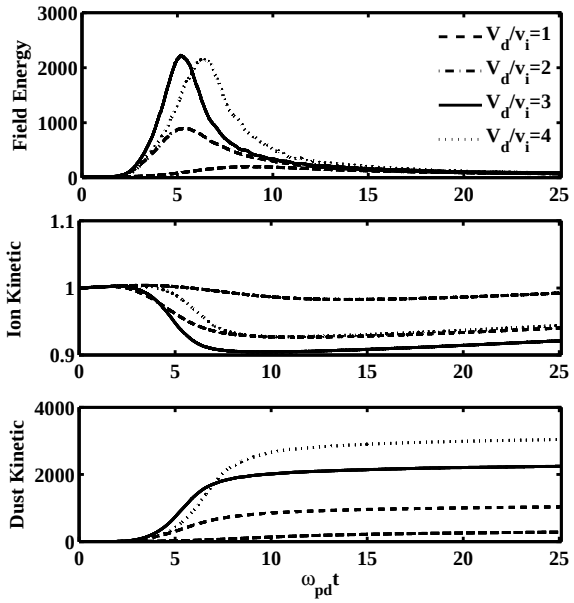

Figure 4.4: Energy histories of the electrostatic waves (normalized), the ion kinetic energy, and the dust kinetic energy (normalized to its initial energy) with varying ion drift velocity, other parameters are listed in the text.

4.3 Computational Model and Results

In this section, a two-dimensional hybrid model is used to investigate the dust acoustic instability. Electrons as a charge neutralizing fluid are modeled as an isothermal Boltzmann relation, by assuming an adiabatic response for the electrons $n_{\mathrm{e}} = n_{\mathrm{e0}} \exp(-e\phi/k_{\mathrm{B}}T_{\mathrm{e}})$, which gives the electron density as a function of electrostatic potential, where n_{e0} is obtained from the unperturbed qausi-neturality condition. The advantage for Boltzmann approximation is that the computation costs less by ignoring high frequency electron plasma wave. Both dust and ions are modeled as discrete particles with the standard particle-in-cell PIC method [*Birdsall and Langdon*, 1991]. The full nonlinear Poisson's equation is solved for using the Newton iteration method [*Hockney and Eastwood*, 1981] combining with Successive Over relation Method.

The ion-neutral elastic scattering events are assumed to be hard sphere collisions. A Monte

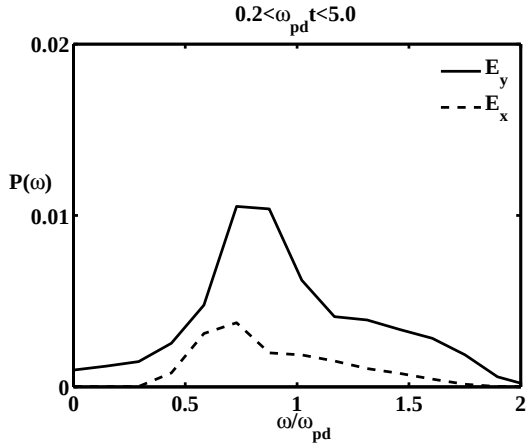

Figure 4.5: Frequency power spectrum $P(\omega)$ of the electric field $E_{\rm x}$ and $E_{\rm y}$ component for $V_{\rm d}/v_{\rm i} = 3, T_{\rm e} = T_{\rm i} = T_{\rm d} = 0.1{\rm eV}, Z_{\rm d} = 2400, n_{\rm d} = 0.0003 n_{\rm i}, m_{\rm d}/m_{\rm i} = 10^5$

Carlo Collision (MCC) model is used to treat ion and cold neutral collisions [*Birdsall and Langdon*, 1991; *Vahedi and Surendra*, 1995]. The simulation domain has $L_{\rm x} = 128\lambda_{\rm di}$ with 128 cells in length and $L_{\rm y} = 256\lambda_{\rm di}$ in width with 256 cells with both periodic boundary conditions. Based on the linear analysis, the unstable modes are well resolved into the simulation domain. In each grid cell, there are 100 particles for each ion and dust species , respectively. Considering the CARE parameters $n_{\rm i} = 3 \times 10^{11}\,{\rm m}^{-3}, T_{\rm e} = T_{\rm i} = T_{\rm d} = 0.1\,{\rm eV}$ at an altitude near 280 km, the ion plasma frequency is estimated about $\omega_{\rm pi} = 1.8 \times 10^5\,{\rm rad/s}$. The time step is chosen $\omega_{\rm pi} dt = 0.04$ in order to keep energy conversion and reduce noise level.

Figure 4.4 shows the energy evolution of the electrostatic waves, ions and dust. The ion kinetic energies are normalized to their initial values. The wave grows exponentially and saturates at time $\omega_{\rm pd} t \approx 5.0$. The growth rate for the case $V_{\rm d}/v_{\rm i} = 3$ is calculated to be $\gamma \approx 0.025\omega_{\rm pi}$, smaller than the maximum growth rate $\gamma \approx 0.04\omega_{\rm pi}$ in Figure 4.1. This is probably due to the fact that the simulation growth rate calculation is an averaged process, some other modes may also exist although weak but still can weaken the growth rate of the dominate mode to some extent. The simulation growth rate, although not exact as that from

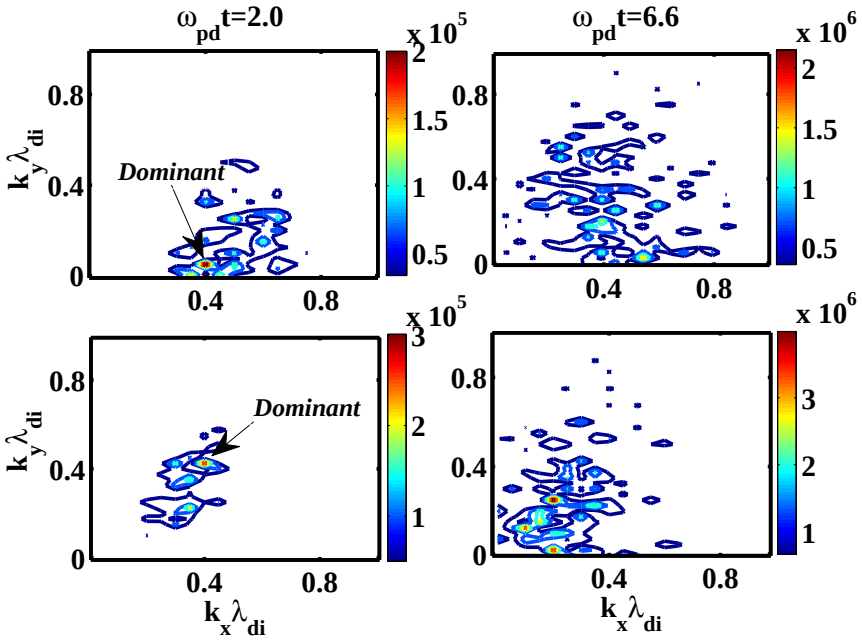

Figure 4.6: Wavenumber power spectrum $P(k_{\rm x}, k_{\rm y})$ of electron density for the drift velocity $V_{\rm d}/v_{\rm i} = 2(upper)$ and $V_{\rm d}/v_{\rm i} = 3(below)$ at different times, other paramters are $Z_{\rm d} = 2400, n_{\rm d} = 0.0003 n_{\rm i}, m_{\rm d}/m_{\rm i} = 10^5$. Note oblique propagation angle for lager drift velocity.

linear analysis, does give an very acceptable estimation of the analytical growth rate range. The drift velocity with $V_{\rm d}/v_{\rm i} = 3$ seems the most effective way to transfer more of the initial ion kinetic energy to electrostatic field energy. When the drift velocity becomes larger, it seems that ion kinetic energy will not be extracted more efficiently in the sense that the ion kinetic energy is used for heating dust more than generating much stronger electrostatic waves. The maximum saturation level increases if we compare the drift velocity for two cases $V_{\rm d}/v_{\rm i} = 2$ and $V_{\rm d}/v_{\rm i} = 3$. The saturation level keeps almost the same for $V_{\rm d}/v_{\rm i} = 3$ and $V_{\rm d}/v_{\rm i} = 4$, however, it may take a longer time for waves to grow with drift velocity $V_{\rm d}/v_{\rm i} = 4$. Beyond the saturation time, the wave begins to damp due to particle trapping.

Figure 4.5 shows the frequency power spectrum of the $E_{\rm x}$ and $E_{\rm y}$ electric field component at position (64,128), which represents components of wave field along and across the streaming

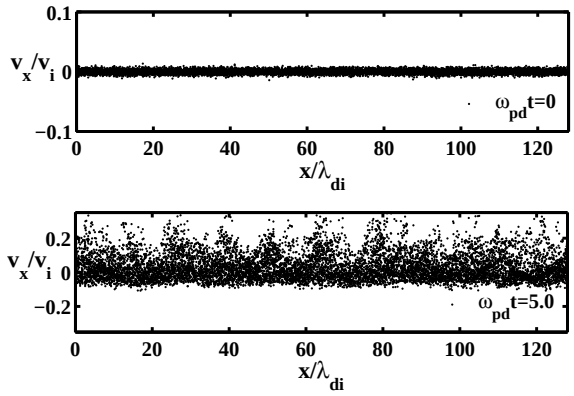

Figure 4.7: Dust dynamics in phase space for $V_{\rm x}-x$ for $V_{\rm d}/v_{\rm i}=3, T_{\rm e}=T_{\rm i}=T_{\rm d}=0.1{\rm eV}, Z_{\rm d}=2400, n_{\rm d}=0.0003n_{\rm i}, m_{\rm d}/m_{\rm i}=10^5$

direction. The power spectrum is estimated by calculating the Fast Fourier Transform (FFT) using the time series for the time period $0.1<\omega_{\rm pd}t<5.0$. The frequency power spectrum is then $P(\omega)=|E_{\rm x}(\omega)|^2$ or $P(\omega)=|E_{\rm y}(\omega)|^2$. It is observed that the frequency power spectral density maximizes near the frequency $\omega\approx 0.5\sim 0.7\omega_{\rm pd}$, which agrees with that obtained from the dispersion relation in Figure 4.1. The real frequency can be also verified using the dust acoustic dispersion relation and the wavenumber calculated from the simulation. The two-dimensional wavenumber power spectrum is also shown in Figure 4.6. at different times. The wavenumber spectrum is calculated by taking a two-dimensional FFT in spatial coordinates of $n_{\rm e}(x,y)$ which results in $n_{\rm e}(k_{\rm x},k_{\rm y})$. The two-dimensional wavenumber power spectrum is $P(k_{\rm x},k_{\rm y})=|n_{\rm e}(k_{\rm x},k_{\rm y})|^2$. In Figure 4.6, during the wave linear growth stage at $\omega_{\rm pd}t=2.0$, it is noted that one dominate mode exists near the streaming direction at this time for the case of the drift velocity $v_{\rm d}/v_{\rm i}=2$ as predicted by linear theory. There are also some other modes with small growth rate, most of which exist along an angle less than $\theta=45^o$. For the drift velocity $V_{\rm d}/v_{\rm i}=3$, the dominant mode always exists at an angle about $\theta=45^o$ in the linear stage, which agrees with results given as predicted by linear analysis in Figure 4.2. This indicates that waves may mainly propagate obliquely to the streaming direction when the drift velocity is greater than a threshold, which may be important for radar diagnostics. The wave propagation angle agrees well with the linear

analysis for varying drift velocity. After the wave saturation, the dominant mode is not so clear to be shown as that in the linear wave growth period.

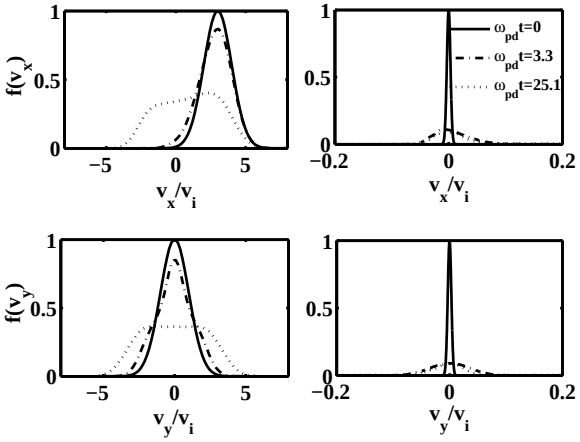

Figure 4.8: (Left) ion and (right) dust velocity distribution function at different times for $V_{\rm d}/v_{\rm i} = 3, T_{\rm e} = T_{\rm i} = T_{\rm d} = 0.1{\rm eV}, Z_{\rm d} = 2400, n_{\rm d} = 0.0003 n_{\rm i}, m_{\rm d}/m_{\rm i} = 10^5$

To better understand the role of the wave-particle interaction in dust dynamics, the dust phase space velocity in $V_{\rm x} - x$ is shown at time $\omega_{\rm pd} t = 0$ and $\omega_{\rm pd} t \approx 5.0$ in Figure 4.7. When the potential fluctuation becomes large as the wave grows, dust with smaller velocity relative to the wave become trapped and heated by waves. The maximum amplitude of dust velocity is less than $0.3 v_{\rm i}$ and the average velocity gets close to the dust phase speed, where the dust acoustic phase velocity $c_{\rm DA}$ is estimated about $0.06 v_{\rm i}$. It shows the onset of dust trapping with mode number 8 in the streaming $\hat{x}$ direction. The trapping structure may become less obvious as the dust becomes thermalized. The ion and dust velocity distribution function are shown in Figure 4.8 at different stages. At time $\omega_{\rm pd} t \approx 3.3$, we can see a small plateau near the wave phase velocity in the streaming $\hat{x}$ direction, due to the fact that the wave begins to trap particles. Particles with velocities near the wave phase velocity become trapped. Both ions and dust are heated in two dimensions as the wave grows. The physical situation producing ion and neutral collisions is that a portion of the injected neutral gas in the rocket exhaust may collide with the ion beam due to charge exchange. There is a relative drift

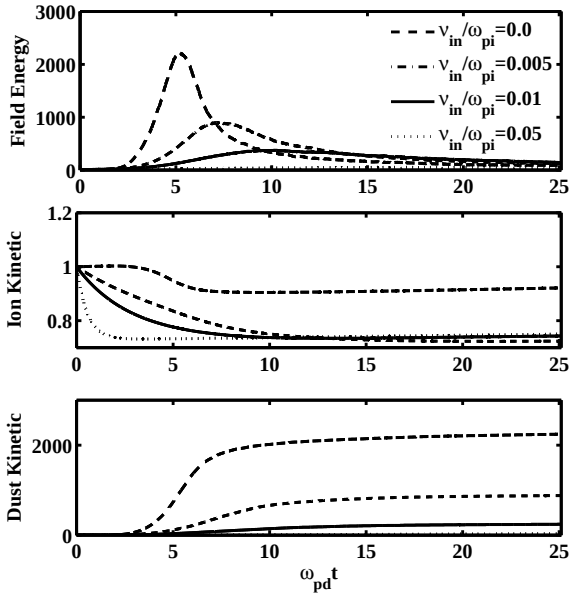

Figure 4.9: Energy histories of the electrostatic waves (normalized), the plasma kinetic ion energy, and the dust kinetic energy (normalized to its initial energy) with varying ion neutral collision frequency, other parameters are $V_{\rm d}/v_{\rm i} = 3, T_{\rm e} = T_{\rm i} = T_{\rm d} = 0.1{\rm eV}, Z_{\rm d} = 2400, n_{\rm d} = 0.0003 n_{\rm i}, m_{\rm d}/m_{\rm i} = 10^5$.

between neutrals and ions. The ion-neutral collisions are expected to reduce the growth rate of wave field according to the linear analysis. Figure 4.9 shows the time history of the energy for electrostatic waves and particle kinetic for varying ion and neutral collision frequency. The collisions actually reduce the electrostatic field energy fluctuation level. For the case $\nu_{\rm in}/\omega_{\rm pi} = 0.01$, corresponding to $\nu_{\rm in} = 0.08\omega_{\rm pd}$, the instability is becoming weak. When the ion and neutral collision frequency $\nu_{\rm in} > \gamma$, for the case $\nu_{\rm in}/\omega_{\rm pi} = 0.05$ corresponding to $\nu_{\rm in} = 0.38\omega_{\rm pd}$, one would expect a dissipative type instability and the maximum growth rate is $\gamma/\omega_{\rm pd} \approx (1/\sqrt{2}A^{3/4})(\omega_{\rm pi}/\nu_{\rm in})^{1/2}$ [*Rosenberg*, 1996]. The growth rate reduces as the ion neutral collision frequency as shown in Figure 4.3. It can be argued that as the neutral gas density is increasing, such an instability may quench.

4.4 Discussion of Applications

The principal application involves the Charged Aerosol Release Experiment (CARE) in the ionosphere but also potential applications are for the planetary ring system of Saturn and laboratory dusty plasma. A wide set of parameters has been investigated including equilibrium dust charge, dust density, the dust drift velocity using the kinetic plasma dispersion. The drift velocity, as one of the most important factors, affects the efficiency of energy extracted from the ion beam. The drift velocity range actually affects how strong such instability can be excited and the direction in which waves may grow into larger amplitudes. Moreover, the dust density percentage also determines the wave propagation angle. The most unstable dust acoustic wave may propagate obliquely to the streaming direction when the drift velocity is lager than twice ion thermal velocity. This conclusion is important for radar diagnostics and in-situ measurement in the future CARE experiment. The wave saturates by trapping dust.

It is important to note that the ion-neutral collision reduces and even quenches such instability. And as the ion neutral collision frequency increases, the wave may potentially propagate even further off the streaming direction before waves damp out. The simulation model also shows the nonlinear evolution of the system. As the wave develops into nonlinear stage, ions lost drift energy and transfer this energy to electrostatic waves. Such instability heats dust and ions in two dimensions. Another application is the role of such dust acoustic instability in the heating of ions to explain the observed radial increase of the ion temperature in the inner magnetosphere of Saturn [*Winske and Rosenberg*, 1998]. The kinetic computer simulation may also give certain comparison to the dust acoustic modes excited by an ion beam observed in laboratory experiments as well.

4.5 Summary

A model for investigating the dust acoustic instability driven by ion beam has been described for unmagnetized dusty plasmas. Such dust acoustic instability considered here may also occur along the geomagnetic field in magnetized dusty plasmas. A two-dimensional hybrid electrostatic model is used to investigate the dust acoustic instability driven by ion beam. To understand the generation and the nonlinear electrostatic waves, we investigate possible parameter regimes for the dust acoustic instability. The kinetic dispersion relation is solved numerically to investigate effects of the ion drift velocity and the dust charge and density on the wave growth rate and the wave propagation direction.

Chapter 5

Lower Hybrid Streaming Instability in a Magnetized Homogeneous Dusty Plasma

Plasma turbulence associated with the creation of an artificial dust layer in the earth's ionosphere is investigated. In this chapter, the lower hybrid streaming turbulence is considered as the dust is injected across the geomagnetic field into the background plasma. Section 5.2 describes the linear dispersion analysis for lower hybrid instability. A two-dimensional hybrid particle-in-cell model is developed in Section 5.3 to investigate the lower hybrid instability driven by the streaming charged dust beam. Section 5.4 present simulation results for a broad range of parameters of the dust cloud, that may impact nonlinear evolution of waves for the regimes of upcoming space experiments. Section 5.5 discusses similarities between past observations of lower hybrid turbulence observed during passive space experiments in the auroral region and lower hybrid turbulence generated by such active experiments. Section 5.6 will summarize useful parameter regimes for upcoming space experiments and comparisons with related experimental observations.

5.1 Introduction

The objectives of the recent Charged Aerosol Release Experiment (CARE) [*Bernhardt*, 2009; *Bernhardt et al.*, 2011] are to examine the effect of artificially-created, charged-particulate layers in the ionosphere on the scatter of UHF, L-Band and S-Band radars. This is motivated in part by the fact that natural dusty plasmas associated with polar mesospheric clouds are well known to enhance the scatter of radar echoes in the frequency range from several MHz to 900 MHz [*Balsley et al.*, 1983; *Cho and Kelley*, 1993]. This enhanced scatter is due to electron irregularities associated with the charged dust. The creation and evolution of plasma irregularities, which may impact the backscatter radar signals, is the purpose of this paper. The CARE I rocket experiment launched on 19 September, 2009 at 1946 EDT used a chemical release from a Nihka motor at 280 km altitude with 111 kg of aluminum oxide Al_2O_3 dust and 200 kg of exhaust molecule vapors. The Al_2O_3 dust attaches more electrons than ions to form a negatively charged streaming dust beam, which serves as the energy source of exciting plasma waves.

A wide range of plasma waves during a localized dust release can be excited depending on the geometry of the sounding rocket experiment [*Bernhardt et al.*, 2012]. The lower hybrid instability is one important possibility [*Rosenberg et al.*, 2011; *Bordikar and Scales*, 2012], which also includes ion acoustic and dust acoustic waves [*Scales et al.*, 2010; *Rosenberg et al.*, 2011; *Fu and Scales*, 2011; *Fu and Scales*, 2012; *Mahmoudian and Scales*, 2011]. With application to rocket exhaust as well as space shuttle exhaust, the lower hybrid streaming instability driven by a charged dust beam across the geomagnetic field has been investigated with linear plasma theory by *Rosenberg et al.* [1999], *Chae et al.* [2000], and *Rosenberg et al.* [2011]. The lower hybrid instability occurs in the dust plasma time scale after the dust reaches its equilibrium charge state. Note this is to be distinguished from the lower hybrid shear-driven instability in the dust cloud boundary layers which may also occur [*Scales et al.*, 2010; *Bordikar and Scales*, 2012]. During space experiments, however, the waves will most likely be in a nonlinear turbulent state. For more realistic study, the nonlinear evolution

of the lower hybrid streaming instability has been considered with hybrid computational models, which treat electrons and ions as fluid (dust as particle-in-cell PIC) with strongly magnetized electrons $\omega_{\rm pe}/\Omega_{\rm ce} \to 0$ [*Chae et al.*, 2000; *Scales et al.*, 2010; *Bordikar and Scales*, 2012], where $\omega_{\rm pe}$ and $\Omega_{\rm ce}$ are the electron plasma and cyclotron frequency, respectively. Also, since these models used fluid ions, important ion kinetic effects were ignored. These models, while providing initial progress, were inadequate for more careful investigation of nonlinear evolution and characterization of lower hybrid turbulence for upcoming space experiments. This is particularly true for describing spatial structure that it is possible to measure during in-situ observations.

A new hybrid model has developed in this chapter to investigate the lower hybrid instability due to streaming charged dust across a magnetic field, which includes both the electron inertial and ion kinetic effects. On one hand, the new model shows the advantage of investigating the more realistic ratio of $\omega_{\rm pe}/\Omega_{\rm ce}$ in the ionosphere as well as the real mass ratio between ions and electrons. The full electron dynamics provide more accurate characterization of spatial structures in electron density. On the other hand, kinetic ions play an important role in assessing nonlinear saturation and ion heating. A number of these characteristics have qualitative similarity to the nonlinear lower hybrid irregularities observed in the auroral region [e.g., *LaBelle et al.*, 1986; *Retterer*, 1997; *Schuck et al.*, 2003].

5.2 Linear Analysis

The plasma model consists of electrons, singly charged ions, and streaming dust grains with charge $Q_{\rm d} = -Z_{\rm d}e$. The dust grains are negatively charged due to attaching more electrons than ions, which are assumed to be of identical size for simplicity. The charge neutrality condition is

$$n_{\rm i} - n_{\rm e} - Z_{\rm d} n_{\rm d} = 0 \tag{5.1}$$

where n_α is the number density of charged species α, denoting electrons, ions and dust, respectively.

The linear dispersion for waves with complex frequency $\omega = \omega_\mathrm{r} + i\gamma$ and wave vector $\mathbf{k}$ is defined in terms of the streaming direction $\hat{x}$, such that $\mathbf{k}\cdot\hat{x} = k\cos\theta$. Note θ is the angle away from the streaming direction. The dispersion for the lower hybrid instability driven by the charged dust relative to the background plasma with drift velocity V_d in the $\hat{x}$ streaming direction is written

$$1 + \chi_\mathrm{e} + \chi_\mathrm{i} + \chi_\mathrm{d} = 0 \tag{5.2}$$

where $\chi_\mathrm{e}, \chi_\mathrm{i}, \chi_\mathrm{d}$ are susceptibilities defined as

$$\chi_\mathrm{e} = \frac{1}{k^2\lambda_\mathrm{De}^2}\left\{1 + \zeta_\mathrm{e0}\sum_{n=-\infty}^{n=\infty}\Gamma_\mathrm{n}(b_\mathrm{e})Z(\zeta_\mathrm{en})\right\}\left\{1 + \frac{i\nu_\mathrm{en}}{\sqrt{2}k_\parallel v_\mathrm{e}}\sum_{n=-\infty}^{n=\infty}\Gamma_\mathrm{n}(b_\mathrm{e})Z(\zeta_\mathrm{en})\right\}^{-1}$$

$$\chi_\mathrm{i} = \frac{1}{k^2\lambda_\mathrm{Di}^2}\left\{1 + \zeta_\mathrm{i0}\sum_{n=-\infty}^{n=\infty}\Gamma_\mathrm{n}(b_\mathrm{i})Z(\zeta_\mathrm{in})\right\}\left\{1 + \frac{i\nu_\mathrm{in}}{\sqrt{2}k_\parallel v_\mathrm{i}}\sum_{n=-\infty}^{n=\infty}\Gamma_\mathrm{n}(b_\mathrm{i})Z(\zeta_\mathrm{in})\right\}^{-1}$$

$$\chi_\mathrm{d} = \frac{1}{k^2\lambda_\mathrm{Dd}^2}\left\{1 + \zeta_\mathrm{d0}Z(\zeta_\mathrm{d})\right\}\left\{1 + \frac{i\nu_\mathrm{dn}}{\sqrt{2}kv_\mathrm{d}}Z(\zeta_\mathrm{d})\right\}^{-1}$$

Here $\Gamma_\mathrm{n}(b_\mathrm{e,i}) = I_\mathrm{n}(b_\mathrm{e,i})\exp(-b_\mathrm{e,i})$, where I_n is the modified Bessel function and $b_\mathrm{e,i} = (k_\perp\rho_{e,i})^2$ with $\rho_{e,i}$ as the electron gyroradius and ion gyroradius. Note $\zeta_\mathrm{en} = (\omega + i\nu_\mathrm{en} - n\Omega_{ce})/(\sqrt{2}k_\parallel v_\mathrm{e})$, $\zeta_\mathrm{in} = (\omega + i\nu_\mathrm{in} - n\Omega_{ci})/(\sqrt{2}k_\parallel v_\mathrm{i})$, and $\zeta_\mathrm{d} = (\omega - kV_\mathrm{d}cos\theta)/(\sqrt{2}kv_\mathrm{d})$. Here, $\lambda_{\mathrm{d}\alpha} = (n_\alpha Z_\alpha^2 e^2/\epsilon_0 k_\mathrm{B}T_\alpha)^{-1/2}$, $v_\alpha = (k_\mathrm{B}T_\alpha/m_\alpha)^{1/2}$, and $\nu_{\alpha\mathrm{n}}$ are the species Debye length, thermal speed, and collision frequency with neutrals. T_α and m_α are the species temperature and mass, respectively, and Z is the plasma dispersion function.

The dust-neutral collisions are neglected because the collision frequency is sufficiently small to affect the wave growth rate for such instability, however, the electron-neutral and ion-neutral collisions are necessarily included, which are important for the lower hybrid instability in the sense of impacting the wave growth rate.

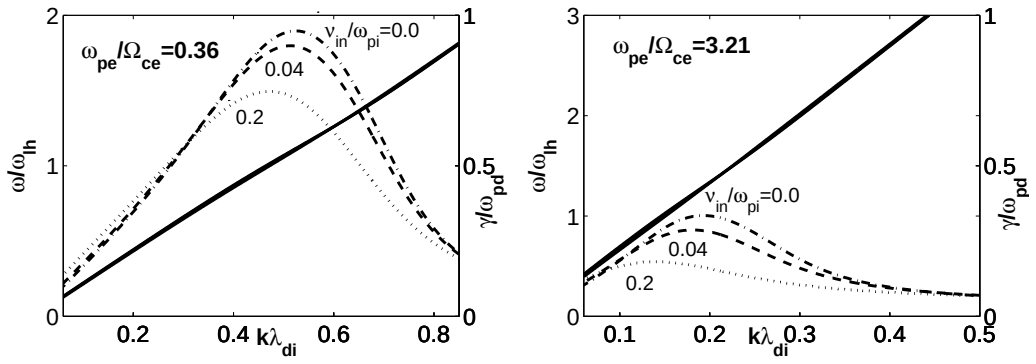

Figure 5.1: Dispersion relation $\omega_{\rm r}$ and wave growth rate γ versus $k\lambda_{\rm di}$ for parameters $\omega_{\rm pe}/\Omega_{\rm ce} = 0.36$ and $\omega_{\rm pe}/\Omega_{\rm ce} = 3.21$.

Considering lower hybrid waves propagating perpendicular to **B** in the limit $\zeta_{\rm e} >> 1$, one obtains $\chi_{\rm e} \simeq [1 - \Gamma_0(b_e)]/k^2\lambda_{\rm De}^2$, where $k_\parallel = 0$ and $k = k_\perp$. If $b_{\rm e} << 1$, then $\zeta_{\rm e} = \omega_{\rm pe}^2/\Omega_{\rm ce}^2$. The simplified plasma dispersion without any collisions for $\zeta_{\rm e} >> 1, \xi_{\rm i} >> 1, \xi_{\rm d} >> 1$ is shown by *Rosenberg et al.* [2011]

$$0 = 1 + \frac{\omega_{\rm pe}^2}{\Omega_{\rm ce}^2} - \frac{\omega_{\rm pi}^2}{\omega^2} - \frac{\omega_{\rm pd}^2}{(\omega - kV_{\rm d}cos\theta)^2} \tag{5.3}$$

where $\omega_{\rm p\alpha}$ and $\Omega_{\rm p\alpha}$ are the species plasma frequency and cyclotron frequency, respectively.

The lower hybrid frequency for a cold plasma is approximately

$$\omega_{\rm lh}^2 = (\omega_{\rm pi}^2 + \omega_{\rm pd}^2)/(1 + \omega_{\rm pe}^2/\Omega_{\rm ce}^2) \tag{5.4}$$

In the ionosphere, plasma parameters at the altitude $\sim 280\,$km are typically as follows. The dominant ion species is O^+, $m_{\rm i}/m_{\rm e} = 16\times1836$, $n_{\rm i} = 5\times10^{11}\,{\rm m}^{-3}$, $T_{\rm e} = T_{\rm i} = T_{\rm d} = 0.1\,$eV and $B = 0.5\,$G. For this case, the ratio $\omega_{\rm pe}/\Omega_{\rm ce}$ is equal to 3.21. In order to make the simulation feasible, the dust mass ratio is reduced from $\sim m_d/m_i = 10^{11}$ to $m_d/m_i = 10^4$ to include dust dynamics in the simulation without loss of generality. The dust parameter for the grain size $r_{\rm d} \sim 0.5\,\mu$m [*Gosse et al.*, 2006; *Mueller and Kessler*, 1985] as an example corresponds to the dust charge number $Z_d = 125$ and the dust density is chosen at $n_d = 0.004n_i$ and thus $n_e =$

$n_i + Z_d n_d = 0.5 n_i$. The ratio of $\omega_{\rm pd}/\omega_{\rm pi} = 0.079$ for this case. As the dust to ion mass ratio increases, the maximum growth rate $\gamma/\omega_{\rm pd}$ actually decreases quantitatively, however, the characteristics of dispersion relation and wave growth rate surface do not change. Therefore, using a reduced mass ratio provides elucidation of the physics while allowing computational efficiency in such simulations [e.g., *Winske et al.*, 1995; *Fu and Scales*, 2011]. The dispersion relation and wave growth rate for $\omega_{\rm pe}/\Omega_{\rm ce} = 3.21$ and $\omega_{\rm pe}/\Omega_{\rm ce} = 0.36$ ($n_{\rm i} = 1 \times 10^{11}\,{\rm m}^{-3}$ and $B = 2\,{\rm G}$) are shown in Figure 5.1 by solving (2) numerically. The real frequency, wave growth rate, the maximum wave growth rate and its corresponding wave numbers provide insight into the lower hybrid instability in the linear regime for guiding and interpreting nonlinear simulations.

The lower hybrid wave growth rate is maximized near the lower hybrid frequency. For $\omega_{\rm pe}/\Omega_{\rm ce} = 3.21$, the maximum wave growth rate is smaller than for the stronger magnetized case $\omega_{\rm pe}/\Omega_{\rm ce} = 0.36$. Also the wavelength of maximum growth is longer for $\omega_{\rm pe}/\Omega_{\rm ce} = 3.21$ and there is a more even distribution of wave growth over the wavenumber space. The stronger magnetized case shows the wave growth to be more strongly peaked near the wavenumber of maximum growth. This will be shown to have important effects on the nonlinear evolution shortly. The impact of ion neutral collisions on the growth rate is shown as well. It is noted that electron neutral collisions are observed to have a much smaller effect. Note there is negligible effect of the ion neutral collisions on the real frequency. Ion neutral collisions reduce the linear growth rate and increase the wavelength of maximum growth.

5.3 Computational Model

In this section, a two-dimensional hybrid model is described to investigate the lower hybrid instability in the plane perpendicular to the geomagnetic field. The inclination angle of magnetic field is ignored for the present investigation. The lower hybrid instability is stabilized due to electron Landau damping as the angle tilts significantly more than the

equal effective mass ratio angle $\sqrt{m_e/m_i}$ [*Bordikar and Scales*, 2012]. The growth rate variation from its maximum is small in this angular regime. Electron kinetic effects are also unimportant for the exactly perpendicular propagation case considered in the paper, which imply a fluid model is valid. The neutral dust particles injected from the rocket exhaust are assumed to charge to their equilibrium state in a much shorter time period than the wave growth period. The negatively charged dust is assumed to have fixed equilibrium dust charge number. The collisionless damping due to dust charge fluctuations is neglected here since the dust charge fluctuation damping rate β is less than the wave frequency, where $\beta = (I_{\rm e}/e)(n_{\rm d}/n_{\rm e}) \approx 10^{-1}\pi r_d^2 n_{\rm d} v_{\rm e}$, and $I_{\rm e}$ is electron current to the dust grain [*Jana et al.*, 1993].

Electrons are described by fluid equations in the frame of electrons rather than moving with the neutral wind

$$\frac{\partial n_{\rm e}}{\partial t} + \nabla \cdot (n_{\rm e}\mathbf{v}_{\rm e}) = 0 \tag{5.5}$$

$$\frac{D\mathbf{v}_{\rm e}}{Dt} = \frac{q_{\rm e}}{m_{\rm e}}(\mathbf{E} + \mathbf{v}_{\rm e} \times \mathbf{B}) - \frac{k_{\rm B}T_{\rm e}}{m_{\rm e}}\frac{\nabla n_{\rm e}}{n_{\rm e}} - \nu_{\rm en}(\mathbf{v}_{\rm e} - \mathbf{v}_{\rm n}) \tag{5.6}$$

where $\frac{D\mathbf{v}_{\rm e}}{Dt} = \frac{\partial \mathbf{v}_{\rm e}}{\partial t} + (\mathbf{v}_{\rm e} \cdot \nabla)\mathbf{v}_{\rm e}$. Equations 5.5 and 5.6 are solved spatially with pseudo-spectral methods and a second-order Adams-Bashfourth-Moulton predictor-corrector scheme is used for the time advance. Both dust and ions are modeled as discrete particles with the standard particle-in-cell PIC method [*Birdsall and Langdon*, 1991]. This method does not assume a quasi-neutrality condition, therefore, the full Poisson's equation $\epsilon_0\nabla^2\phi = -(q_e n_e + q_i n_i + Q_d n_d)$ was solved by spectral methods.

The ion-neutral elastic scattering events are assumed to be hard sphere elastic collisions. A Monte Carlo Collision (MCC) model is used to treat ion and cold neutral collisions [*Birdsall*, 1991; *Vahedi et al.*, 1994]. The collision probability for the i*th* particle is $P_{\rm i} = 1 - \exp(-\Delta t \sigma_{\rm in} n_{\rm g} V_{\rm i})$, where $V_{\rm i}, \sigma_{\rm in}, n_{\rm g}$ is the velocity of particle, ion and neutral collision

cross section and neutral gas density, respectively. A collision occurs when a uniformly distribution random number on the interval [0 1] is less than the collision probability $P_{\rm i}$.

5.4 Simulation Results

The simulation domain has $L_{\rm x} = 128\lambda_{\rm di}$ with 128 grid cells and $L_{\rm y} = 128\lambda_{\rm di}$ with 128 cells with periodic boundary conditions in both dimensions. Based on the linear analysis, the unstable modes are well resolved in the simulation domain. In each grid cell $dx = dy = \lambda_{\rm di}$, there are 100 particles for each species (i.e. ions and dust), respectively. The time step is chosen to be $\omega_{\rm pi}\Delta t = 0.001$ in order to insure adequate energy conservation and low noise level in the simulation.

5.4.1 Effect of the ratio $\omega_{\rm pe}^2/\Omega_{\rm ce}^2$

The factor of $\omega_{\rm pe}^2/\Omega_{\rm ce}^2$ varies with altitude in the ionosphere, which impacts electron dynamics. The ratio may vary due to the amount of charge on dust after release of dust particles. The factor of $\omega_{\rm pe}^2/\Omega_{\rm ce}^2$ categorizes electrons into two limiting cases: strongly magnetized electrons and weakly magnetized electrons, which behave quite differently from each other. Thus, it is important to investigate electron dynamics on the nonlinear evolution of the lower hybrid instability. Figure 5.2 shows the time history of the field energy, the plasma ion kinetic energy and the dust kinetic energy for three cases $\omega_{\rm pe}/\Omega_{\rm ce} = 0.36, 1.02, 3.21$. The simulations run for several wave growth periods depending on parameters. There are several ways of varying this ratio $\omega_{\rm pe}/\Omega_{\rm ce}$. The way of varying the ratio in this chapter is to adjust the magnetic field and electron density. For the three cases, the electron density is $n_{\rm e} = 1 \times 10^{11}, 1 \times 10^{11}, 5 \times 10^{11}\,{\rm m}^{-3}$ and the magnetic field is $B = 2, 7, 0.5\,{\rm G}$, respectively. The electrostatic field energy is calculated by $\frac{1}{2}\epsilon_0 \int |\mathbf{E}|^2 dxdy$, where $\mathbf{E}$ is the electric field vector. The free energy source is the charged streaming dust, which transfers its kinetic energy to excite lower hybrid waves. For now, collisional effects are neglected and will be

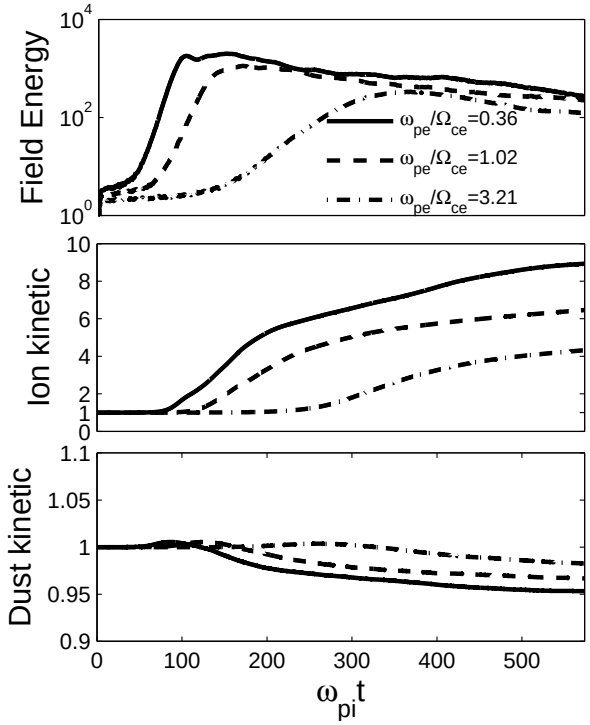

Figure 5.2: The energy histories of the electrostatic field energy(normalized), the plasma ion kinetic energy, and the dust kinetic energy (normalized to its initial energy).

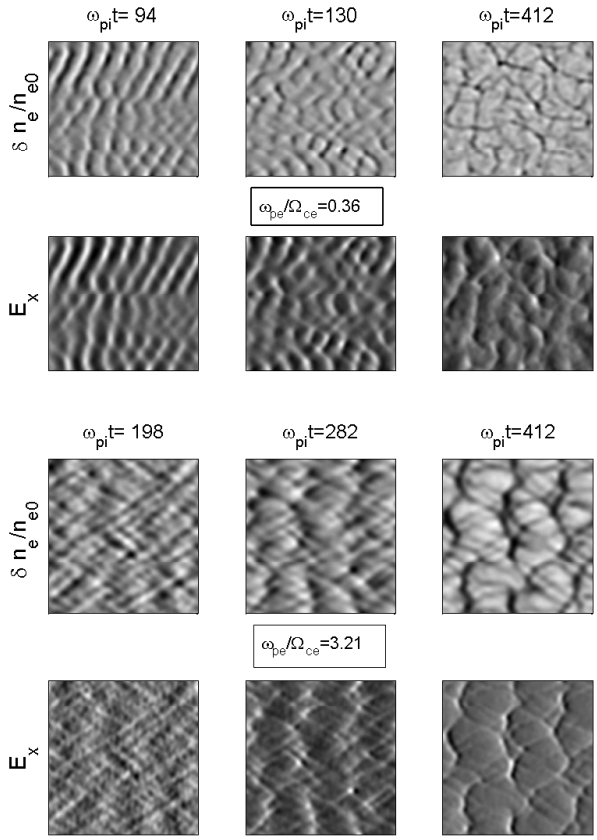

Figure 5.3: Two-dimensional electron density irregularity $\delta n_{\rm e}/n_{\rm e0}$ and the electric field $E_{\rm x}$ for the lower hybrid instability for $\omega_{\rm pe}/\Omega_{\rm ce} = 0.36$ and $\omega_{\rm pe}/\Omega_{\rm ce} = 3.21$.

considered shortly. The wave grows linearly initially and then saturates. The field energy for the case $\omega_{\rm pe}/\Omega_{\rm ce} = 0.36$, which corresponds to relatively strongly magnetized electrons, shows the maximum wave growth rate about $\gamma/\omega_{\rm pd} \sim 0.78$, which agrees favorably with linear theory. As the ratio of $\omega_{\rm pe}/\Omega_{\rm ce}$ increases to 3.21, which approximately corresponds to the F-peak of the ionosphere, the maximum wave growth rate reduces to $\gamma/\omega_{\rm pd} \sim 0.18$. The strongly magnetized electrons can transfer a larger percentage of dust kinetic energy to excite stronger electrostatic lower hybrid waves and also dust particles are heated by waves. The excited electrostatic lower hybrid waves cause transverse ion acceleration as will shown later in detail.

The two-dimensional electron density fluctuation $\delta n_{\rm e}/n_{\rm e0}$ and the electric field $E_{\rm x}$ (normalized by $k_{\rm B}T_{\rm e}/\lambda_{\rm di}e$) along the streaming direction are shown in Figure 5.3 at three different times for $\omega_{\rm pe}/\Omega_{\rm ce} = 0.36, 3.21$, where $n_{\rm e0}$ is the equilibrium electron density. It is clear that in the wave linear growth stage, the electron density fluctuation phase front changes as the ratio $\omega_{\rm pe}/\Omega_{\rm ce}$ changes, which is also true for the electric field. The wave phase front structure for $\omega_{\rm pe}/\Omega_{\rm ce} = 0.36$, the strongly magnetized case, looks similar to the case for $\omega_{\rm pe}/\Omega_{\rm ce} = 1.02$. The phase fronts change significantly if we compare these two cases: $\omega_{\rm pe}/\Omega_{\rm ce} = 0.36$ representing strongly magnetized case and $\omega_{\rm pe}/\Omega_{\rm ce} = 3.21$ representing weakly magnetized case. It is observed that the phase fronts change to propagate at an angle to the streaming direction in the weakly magnetized case. In other words, there is a transition of the field energy relative to the streaming direction. This is still true after nonlinear saturation. Figure 5.3 does show some sign of vortex formation in the density structures upon careful inspection for $\omega_{\rm pe}/\Omega_{\rm ce} = 0.36$. It should be noted that the fact that propagation is in the streaming direction at early times in the strongly magnetized case is consistent with past simulations, which assumed $\omega_{\rm pe}/\Omega_{\rm ce} \to 0$ [e.g., *Bordikar and Scales*, 2012]. For strongly magnetized electrons, the maximum electron density perturbation is about 10% percent, which is quite smaller than the 50% percent perturbation for the weakly magnetized case. In general, for the weakly magnetized case, relatively large electron density perturbations with weaker electric fields are produced, while for the strongly magnetized case, relatively small electron density perturbations with stronger electric fields are produced.

Figure 5.4 shows the mode number spectrum by taking a two-dimensional FFT in spatial coordinates of $\delta n_{\rm e}/n_{\rm e0}$, which results in $\delta n_{\rm e}/n_{\rm e0}(m_{\rm x}, m_{\rm y})$. The two-dimensional mode number power spectrum is defined as $P(m_{\rm x}, m_{\rm y}) = |\delta n_{\rm e}/n_{\rm e0}(m_{\rm x}, m_{\rm y})|^2$. Note the relation between the wave number and the mode number is $k_{\rm x} = 2\pi m_{\rm x}/L_{\rm x}$ and $k_{\rm y} = 2\pi m_{\rm y}/L_{\rm y}$. For the strongly magnetized electrons $\omega_{\rm pe}/\Omega_{\rm ce} = 0.36$, the dominant unstable mode exists for $m_{\rm x} \sim 8$ at an early time (before nonlinear saturation) $\omega_{\rm pi}t = 94$, indicating propagation primarily in the streaming direction $\hat{x}$. For weakly magnetized electrons $\omega_{\rm pe}/\Omega_{\rm ce} = 3.21$, most unstable modes exist in a line at an angle $\theta \simeq 66^o$ off the streaming direction at a early time (before

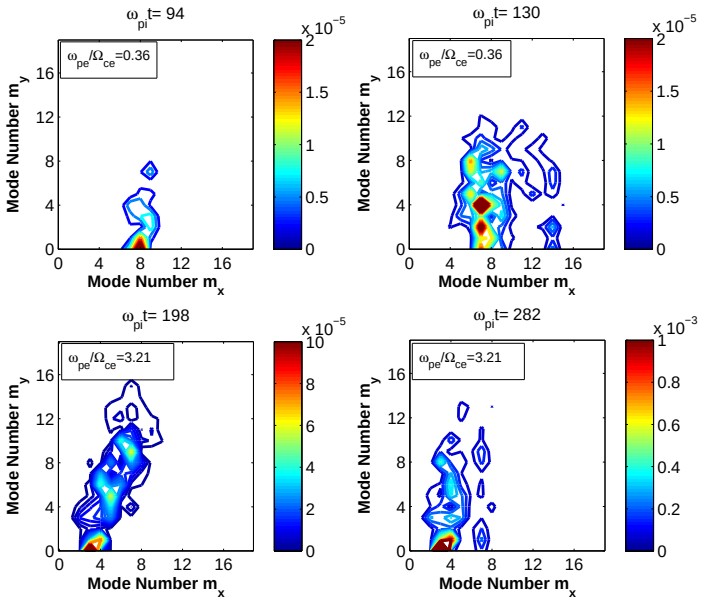

Figure 5.4: Mode number power spectrum $P(m_{\rm x}, m_{\rm y})$ of electron density irregularities $\delta n_{\rm e}/n_{\rm e0}$ for $\omega_{\rm pe}/\Omega_{\rm ce} = 0.36$ (top) and $\omega_{\rm pe}/\Omega_{\rm ce} = 3.21$ (bottom) at two different times. Note the dominant mode for $\omega_{\rm pe}/\Omega_{\rm ce} = 0.36$ is $m_{\rm x} = 8$ along the streaming direction while the dominant modes exists in a narrow range at $\theta = 66^o$ off the streaming direction at a linear stage for $\omega_{\rm pe}/\Omega_{\rm ce} = 3.12$. Larger modes appear in a later time for both.

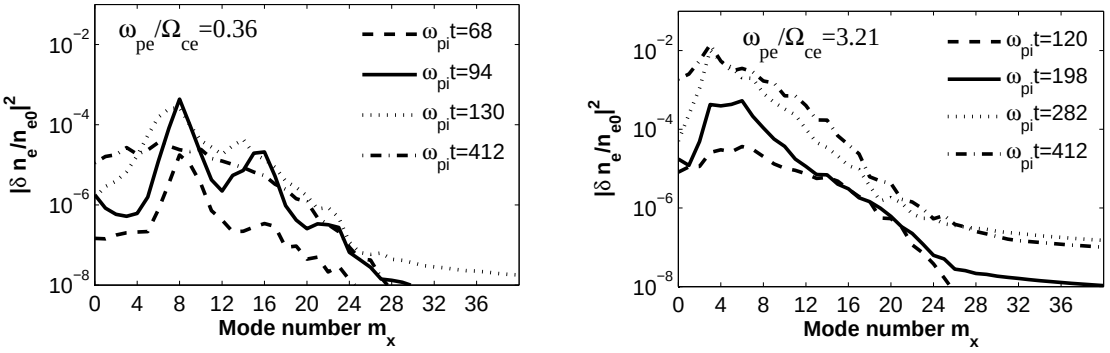

Figure 5.5: Averaged power spectra $P(m_{\rm x})$ of electron density irregularities $\delta n_{\rm e}/n_{\rm e0}$ for a) $\omega_{\rm pe}/\Omega_{\rm ce} = 0.36$ (left) and b)$\omega_{\rm pe}/\Omega_{\rm ce} = 3.21$ (right).

nonlinear saturation) $\omega_{\rm pi}t = 198$ with the strongest ones at $m_{\rm x} = 3 \sim 4$, which agrees with linear analysis. At a later time $\omega_{\rm pi}t = 130$ or $\omega_{\rm pi}t = 282$, it is observed in the wave number spectrum that the wave energy cascades continually from the k values of the linearly unstable modes toward larger k values, indicating shorter wavelength waves. Waves tend to propagate at an angle off the streaming direction when the electrons are weakly magnetized, which shows similar behavior as the ion acoustic instability driven by the dust beam in which electrons are unmagnetized [*Fu and Scales*, 2011]. The wave propagation angle satisfies the resonance condition [*Rosenberg et al.*, 2011].

Figure 5.5 show the transverse average mode power spectra of $\delta n_{\rm e}/n_{\rm e0}$ at four different times for $\omega_{\rm pe}/\Omega_{\rm ce} = 0.36$ and $\omega_{\rm pe}/\Omega_{\rm ce} = 3.21$, respectively. The power spectra is useful since the variation of irregularity amplitude with scale size in the experiment could be measured by power spectrum analysis techniques in the F region of ionosphere [*Dyson et al.*, 1974]. The transverse average power spectra is defined by $P(m_{\rm x}) = \sum_{m_{\rm y}} |P(m_{\rm x}, m_{\rm y})|$. At the linear stage, it is clear for both electron density and electric field spectra that the dominant mode number is $m_{\rm x} = 8$ for the strongly magnetized case in Figure 5.5a, and then larger mode numbers appear in the wavenumber spectrum. Peaks are observed at $m_{\rm x} = 16$ and $m_{\rm x} = 24$, which most likely indicate mode coupling processes in Fourier k space [e.g., *Seyler and Providakes*, 1987]. There are a number of modes $m_{\rm x} = 3 \sim 6$ that appear in the spectrum for the

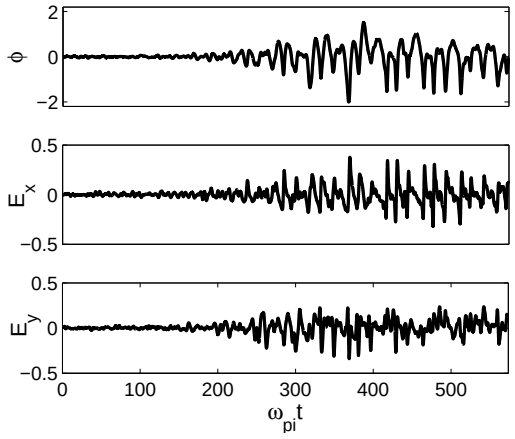

Figure 5.6: Temporal evolution of the electrostatic potential ϕ (normalized by $k_{\rm B}T_{\rm e}/e$)and the electric field $E_{\rm x}$ and $E_{\rm y}$ (normalized by $k_{\rm B}T_{\rm e}/\lambda_{\rm di}e$) for $\omega_{\rm pe}/\Omega_{\rm ce} = 3.21$.

weakly magnetized case in Figure 5.5b. Even in the nonlinear regime, we still can observe the strong mode $m_{\rm x} = 3$ and also other larger modes in the spectrum. It is also noted with less strongly magnetized electrons, the electron density fluctuations are larger but with smaller electric fields. It is true that background density fluctuation are not necessarily correlated with enhanced electric fields as observed in numerous examples during passive space experiments of lower hybrid structures in weakly magnetized regions [*McAdams et al.*, 1998]. The difference in structure of mode number spectrum in Figure 5.5 can be explained to some extent as being due to the more even distribution of linear growth in modes for the weaker magnetized case as shown in Figure 5.1. This fact also most likely precludes observing the distinct mode coupling harmonics for the weaker magnetized case.

Figure 5.6 shows the temporal history of the electrostatic potential ϕ and electric fields, $E_{\rm x}$ and $E_{\rm y}$ for $\omega_{\rm pe}/\Omega_{\rm ce} = 3.21$, respectively. The electrostatic potential is normalized by $k_{\rm B}T_{\rm e}/e$ and electric fields are normalized by $k_{\rm B}T_{\rm e}/\lambda_{\rm di}e$. The electric fields $E_{\rm x}$ show quite bipolar structure and there is unipolar electrostatic potential structure ϕ after the linear stage. Such spiky structure is associated with nonlinear particle acceleration in ion and dust dynamics as will be shown later. The spiky wave structures contribute to a broadband

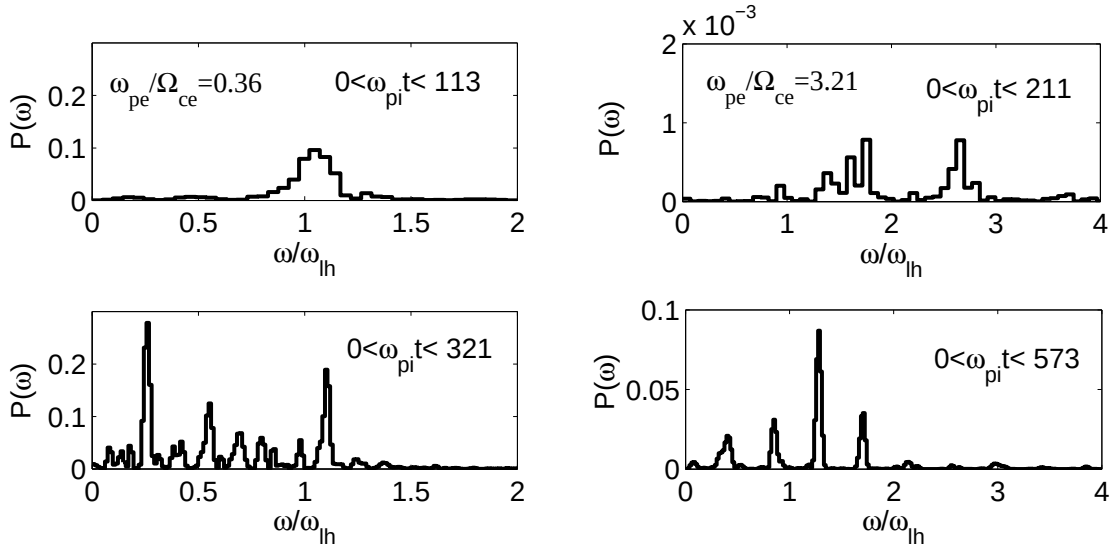

Figure 5.7: Frequency power spectrum of the electrostatic potential ϕ for case a) $\omega_{\rm pe}/\Omega_{\rm ce} = 0.36$ (left) and b) $\omega_{\rm pe}/\Omega_{\rm ce} = 3.21$ (right).

frequency spectrum.

Figure 5.7 shows the frequency power spectrum of the electrostatic potential ϕ for two cases $\omega_{\rm pe}/\Omega_{\rm ce} = 0.36$ and $\omega_{\rm pe}/\Omega_{\rm ce} = 3.21$. The power is maximum at the lower hybrid frequency during the linear growth period $0 < \omega_{\rm pi}t < 113$ and shows quite a wide spectrum for the time period $0 < \omega_{\rm pi} < 321$ for $\omega_{\rm pe}/\Omega_{\rm ce} = 0.36$. But as the ratio $\omega_{\rm pe}/\Omega_{\rm ce}$ increases to 3.21, the frequency spectrum becomes quite spiky if the spectrum is taken during the time period $0 < \omega_{\rm pi}t < 211$ and this harmonics structure becomes even more pronounced during the time period $0 < \omega_{\rm pi}t < 573$. The broadband spiky spectrum is associated with localized density structure as will be shown later in Figure 5.8. The $E_{\rm x}$ field along the streaming direction becomes comparable to the $E_{\rm y}$ field for the case of $\omega_{\rm pe}/\Omega_{\rm ce} = 3.21$ at the linear and nonlinear wave growing stage, while the $E_{\rm x}$ field is much stronger than the $E_{\rm y}$ field for the case $\omega_{\rm pe}/\Omega_{\rm ce} = 0.36$. The frequency spectrum is also related with the electron density fluctuation level as shown by *Seyler* [1994].

Figure 5.8 shows one-dimensional electron density, electrostatic potential, electric field, dust

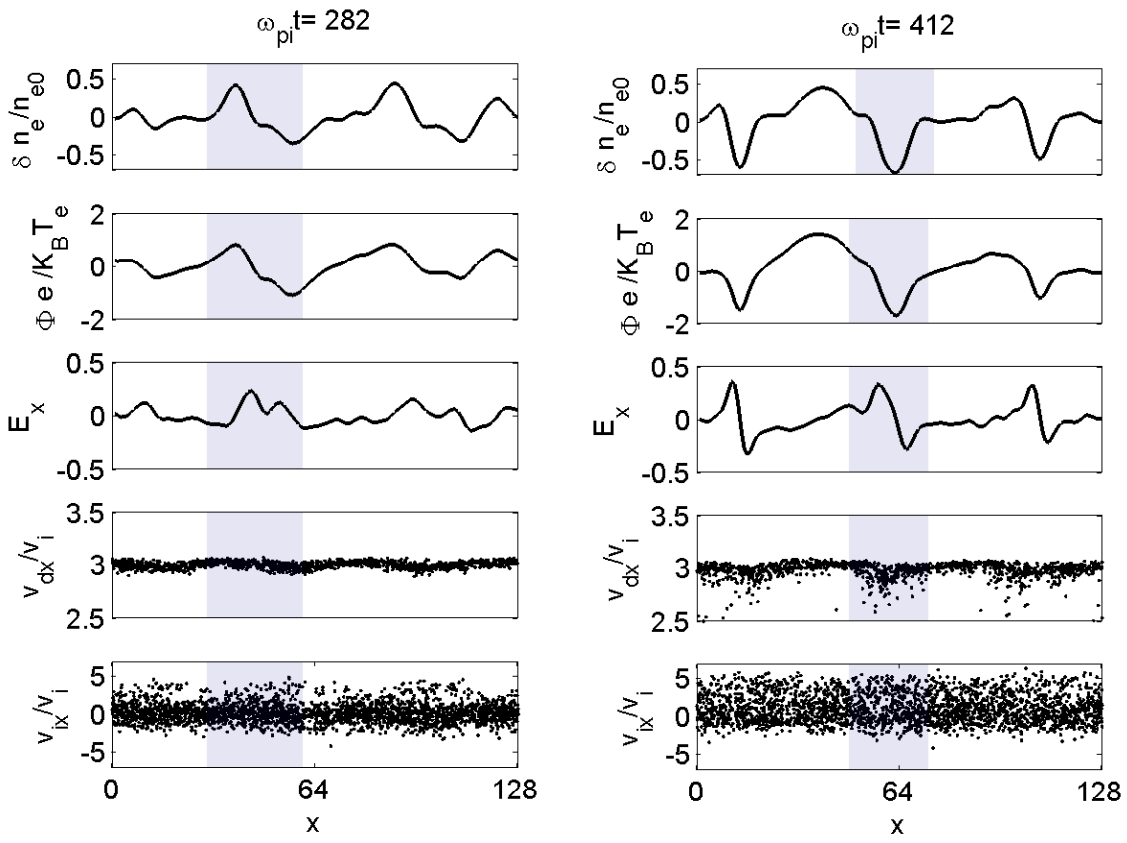

Figure 5.8: From the top: electron density fluctuation, potential, electric field, dust phase space, and ion phase space versus x (normalized by $\lambda_{\rm di}$) for $\omega_{\rm pe}/\Omega_{\rm ce} = 3.21$ at two different times. Note the electron density depletion corresponds to potential drop and enhanced electric field. Electron depletion regions clearly correlate with the dust dynamics in phase space.

and ion $x-v_{\rm x}$ phase space at position $y = 64\lambda_{di}$ at two times $\omega_{\rm pi}t = 282$ (top) and $\omega_{\rm pi}t = 412$ (bottom). At an early time $\omega_{\rm pi}t = 282$, it is found that there are three trapping structures in the ion phase space and dust acceleration. Correspondingly, electron density enhancement structures correlate with ion trapping structure. This can be explained from the electrostatic potential, which can trap ion particles with $e\phi/0.5m_{\rm i}(v_{\rm i} - v_{\rm p})^2 \sim 1$, where $v_{\rm p}$ is the phase velocity of lower hybrid waves. However, the electrostatic potential is not sufficiently strong to trap heavy dust particles $Z_{\rm d}e\phi/0.5m_{\rm d}(V_{\rm d} - v_{\rm p})^2 << 1$. At a late time $\omega_{\rm pi}t = 412$, it is found that there are three obvious localized density cavity structures, which all correspond to electrostatic potential drop and enhanced electric fields and simultaneously correlate with dust acceleration in phase space. It can be argued that the electron density enhancement or depletion is correlated with ion and dust dynamics in phase space. For instance during space experiments, ion phase space holes have been correlated with potential structures during the Viking satellite mission [*Koskenin et al.*, 1990]. It is clearly shown that the dust dynamics in phase space are correlated with the localized density cavity structures in the simulations. The ions are heated transversely by waves and become quite thermalized. The localized density depletion is solitary in space, referred to as lower hybrid solitary. Similar nonlinear structures associated with isolated localized regions of lower hybrid wave in field-aligned cylindrical plasma density depletions have been an intense area of investigation in space plasma for two decades [*Kintner et al.*, 1992]. They are associated with spiky electric field signatures described as lower hybrid 'spiklets' [*Labelle and Kintner*, 1986] similar to the electric field structure shown in Figure 5.6.

Two major competing theories have been developed to explain such lower hybrid solitary structures (LHSS). *Chang* [1993] and *Shapiro et al.* [1993] propose that LHSS are produced by the modulational instability and/or collapse of lower-hybrid waves. *Seyler* [1994] and *Schuck et al.* [1997] suggest the primary spectral features of LHSS are predicted by a linear theory of lower hybrid waves in a preexisting cylinder density depletion. The linear theory also predicts that large localized electric fields can be easily produced by this resonant mechanism. It is possible to use the theory by *Schuck et al.* [1997] to explain the density

depletion percentage and enhanced electric fields depending on the ratio ω_{pe}/Ω_{ce} as in Figure 5.8. The solution of potential structures rotates in angle around the center of the density depletion and the eigenfrequencies are discrete for $\omega < \omega_{lh}$ and $\omega > \omega_{lh}$ with $k_z = 0$. There is some evidence of the rotation in the structures of Figure 5.3 upon close examination, however, detailed study is beyond the scope the current investigation and will be left for a future investigation.

Shukla et al. [1999] also investigated the evolution of linearly unstable waves into nonlinear structures with enhanced electric fields in localized density depletions. A theory was developed for coherent nonlinear structures, which is capable of depicting several stationary nonlinear solutions, including dipolar vortices occurring in the presence of an equilibrium density inhomogeneity in a plasma embedded in a homogenous magnetic field. *Pokhotelov et al.* [1999] presents nonlinear equations of the drift-Alfven waves and also obtains the stationary solution to claim the existence of two scale dipolar vortices with application to dusty plasmas as is the case considered in this study. The nonlinear wave structures, such as dust acoustic solitary waves, are found to be affected by dust temperature and dust streaming (parameters of interest in this study) using the theory by *Maharaj et al.* [2004]. A knowledge of the saturation energy obtained from a nonlinear theory of instabilities in the lower hybrid frequency range could be used to determine the associated anomalous transport properties [e.g., *Huba et al.*, 1978; *Winske and Liewer*, 1978; *Bingham et al.*, 2004]. The primary saturation mechanism here is the heating of background ions which is further evidenced by the impact of collisional effects as will be discussed in next section.

5.4.2 Effect of Dust Parameters

In this section, dust parameters, including dust charge Z_d, dust density n_d, and dust expansion speed V_d are investigated for application to active experiments, which create localized dust clouds in the ionosphere. The typical parameters are chosen for the case $\omega_{pe}/\Omega_{ce} = 3.21$ as given. Figure 5.9 shows the energy history for the dust charge varia-

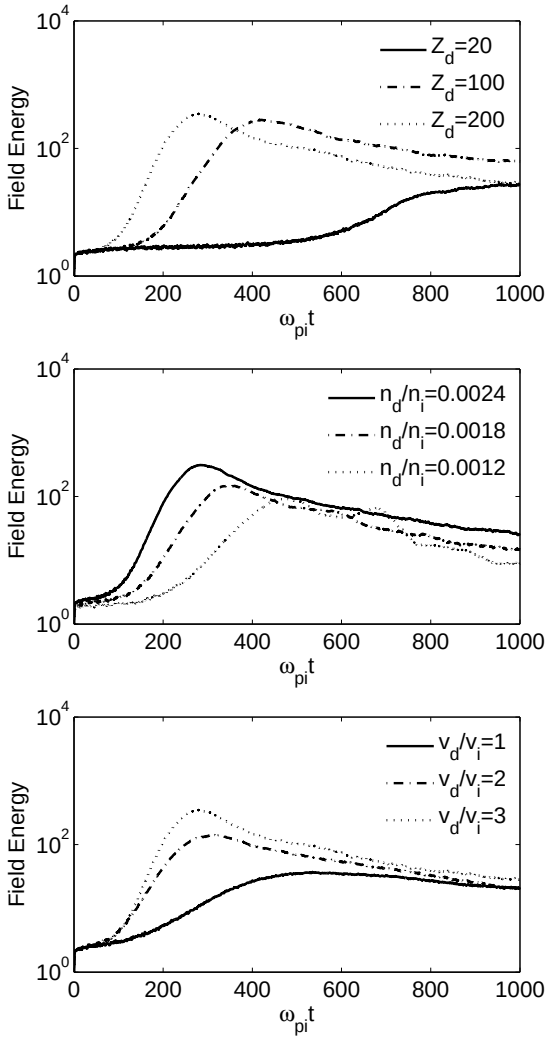

Figure 5.9: The energy history of the electrostatic waves (normalized) with varying dust parameters from the top : a) varying dust charge number Z_d for $n_\mathrm{d}Z_\mathrm{d} = 0.5n_\mathrm{i}$; b) varying dust density for $Z_\mathrm{d} = 200$ and c) varying dust expansion speed for $Z_\mathrm{d} = 200, n_\mathrm{d}Z_\mathrm{d} = 0.5n_\mathrm{i}$.

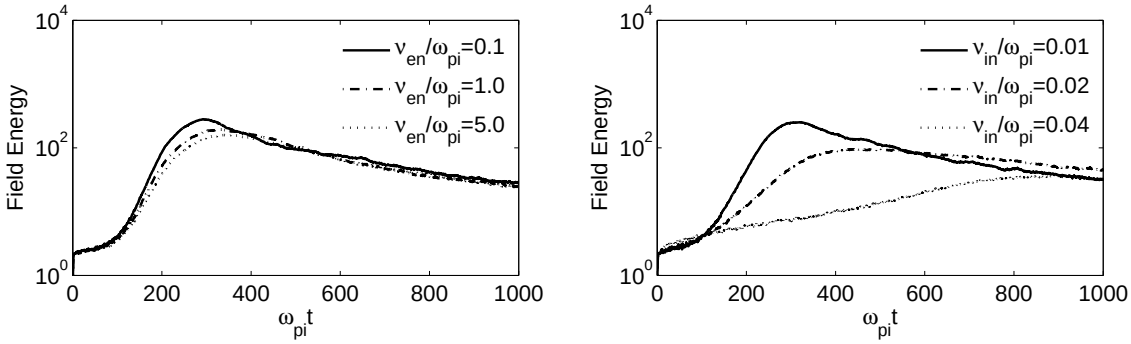

Figure 5.10: The energy history of the electrostatic waves (normalized) with varying electron-neutral and ion-neutral collision frequency for $\omega_{\rm pe}/\Omega_{\rm ce} = 3.21$ with $Z_{\rm d} = 200, n_{\rm d}Z_{\rm d} = 0.5n_{\rm i}$.

tion $Z_{\rm d} = 20, 100, 200$ (top) while keeping $n_e/n_i = 0.5$ and the dust density ratio variation $n_{\rm d}/n_{\rm i} = 0.0024, 0.0018, 0.0012$ for $Z_d = 200$ (middle) and finally the dust expansion speed variation $V_{\rm d}/v_{\rm i} = 1, 2, 3$ (bottom).

In the CARE experiment, the dust size ranges from $\sim 100\,$nm to several μm with peak density centered at about $1\,\mu$m, corresponding to dust charge number $Z_{\rm d}$ from 20 to 250 and more [*Bernhardt et al.*, 2011]. As the dust charge increases and the dust density is reduced while keeping $n_{\rm d}Z_{\rm d} = 0.5$, we begin to see a higher growth rate for $Z_{\rm d} = 200$, but the waves damp more rapidly after saturation. For the dust charge number $Z_{\rm d} = 20$, the lower hybrid instability becomes quite weak. The equilibrium dust charge, which depends on the dust grain radii with relation $Z_{\rm d} \propto r_{\rm d}$ by OLM theory, is an important factor. To access the impact of variation of dust density, the dust charge number $Z_{\rm d}$ is held fixed at 200, and the expansion speed is taken to be equal to three times the ion thermal velocity $V_{\rm d}/v_{\rm i} = 3$. The electron percentage decreases as the dust density increases. The wave field grows fast and tends to saturate at a higher level with higher dust density. When the dust density is of small percentage, the lower hybrid instability may be too weak to be observed. The dust density in the rocket exhaust varies with time. The simulation covers the dust density from $n_{\rm d}/n_{\rm i} \sim 0.0025$ to $n_{\rm d}/n_{\rm i} \sim 0.0012$ for the dust charge number $Z_{\rm d} = 200$, which corresponds to the maximum time $t \sim 0.4\,$s based on estimations by *Rosenberg et al.* [2011]. After

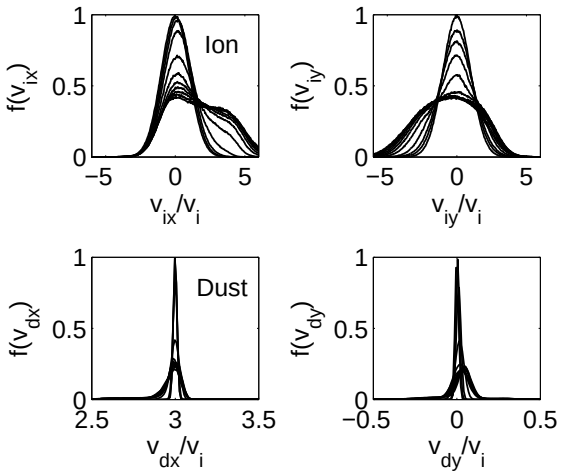

Figure 5.11: The ion-neutral collision effect on the ion and dust velocity distribution function at different times for $\nu_{\rm in}/\omega_{\rm pi} = 0.01$ in the range $0 < \omega_{\rm pi}{\rm t} < 700$ with interval $\omega_{\rm pi}\Delta t = 70$ between each curve.

the dust charges to its equilibrium state, the dust density for $n_{\rm d}/n_{\rm i} \sim 0.0025$ in the plume evolution corresponds to the real time $t \sim 0.25\,{\rm s}$. The dust density in the plume decreases with time, and if the dust density drops below a threshold, the instability may be too weak to be observed. This maximum time in the simulation in terms of dust density is roughly estimated to be about $t \sim 0.5\,{\rm s}$. The dust drift velocity as another parameter is designed in the experiment on the order of the ion thermal velocity. The drift velocity $V_{\rm d}/v_{\rm i} = 3$ appears to be a particularly effective way in terms of extracting more dust kinetic energy into the electrostatic field energy with a higher wave growth rate and saturation level.

5.4.3 Collisional Effects

Collisions with plume neutrals are considered to have an impact on such lower hybrid irregularities. The plume neutrals are taken to move together with the dust drift velocity from the rocket exhaust. Electron-neutral collisions affect the wave growth rate of the lower hybrid instability with the relation $\gamma/\omega_{\rm pd} \sim \frac{1+i}{\sqrt{2C}}(\omega_{\rm lh}/\nu_{\rm e})^{1/2}$ given by *Rosenberg et al.* [2011], where

$C = (1-\Gamma_0)/(k\lambda_{\rm de})$. Figure 5.10 shows the field energy for the electron and neutral collision $\nu_{\rm en}/\omega_{\rm pi} = 0.1, 1.0, 5.0$. The electron-neutral collision frequency $\nu_{\rm en}/\omega_{\rm pi} = 5.0$ corresponds to the maximum estimation value by *Rosenberg et al.* [2011]. The role of electron-neutral collisions damps the waves but it does not affect the wave growth as much as the ion-neutral collision does. Ion collisions with plume neutrals are also investigated for the effect on the instability. The ion and neutral collisions transfer momentum through an elastic scattering model here. The background ions will obtain the injected neutral gas speed in the collision process. The collision algorithm is described by *Birdsall* [1991] and *Vahedi et al.* [1994]. The important factor is the ion and neutral collision frequency relative to the wave growth rate. Within the wave growth period, when the relative drift between background ions and injected dust becomes quite small, the lower hybrid waves are difficult to observe. Considering that ion and plume neutral collisions vary with time, the field energy for the ion-neutral collisions $\nu_{\rm in}/\omega_{\rm pi} = 0.01, 0.02, 0.04$ are shown in Figure 5.10.

In general, the nonlinear spatial structures are less pronounced structure when plume neutral collisions are incorporated, and the growth rate and saturation amplitude are not substantially reduced for $\nu_{\rm in}/\omega_{\rm pi} < 0.01$. When the collision frequency becomes larger than the wave growth rate $\gamma/\omega_{\rm pi} \sim 0.02$ ($\nu_{\rm in}/\omega_{\rm pi} = 0.04$), the lower hybrid instability is stabilized. Figure 5.11 shows the ion-neutral collision effect for $\nu_{\rm in}/\omega_{\rm pi} = 0.01$ from the perspective of ion and dust particle velocity distribution varying with time. Without ion-neutral collisions, we observe the plateau in the ion velocity distribution near the wave phase velocity and dust particle heating when the lower hybrid instability develops. The collision effect shows up after waves saturate, which drive background ions to the neutral speed. However, for collision frequency $\nu_{\rm in}/\omega_{\rm pi} = 0.04$, the ions acquire a drift velocity in the streaming $\hat{x}$ direction in a timescale less than the wave growing period due to the exhaust neutral and ion collisions. The relative drift between the streaming dust and ion particles is relatively small, and is not sufficiently large enough to generate the lower hybrid instability. The ions are still heated due to ion and exhaust neutral collision effect but the dust heating due to wave and particle interaction is quite minor. Note if the neutral speed were assumed smaller than the dust

speed, then the wave growth rate and saturation amplitude are expected to be larger since the ion (or electron) and neutral collision frequency will be smaller.

5.5 Discussion of Applications

Lower hybrid turbulence with similarities predicted by active dust cloud releases in this work have been an intense area of investigation for the past two decades. Localized electrostatic wave packets near the lower hybrid frequency or lower hybrid cavitons were detected by the MARIE sounding rocket [*Labelle et al.*, 1986]. The TOPAZ-III sounding rocket [*Vago et al.*, 1992 ; *Kintner et al.*, 1992] and later the FREJA satellite [*Eriksson et al.*, 1994; *Pcseli, et al.*, 1996] show correlation between the associated small-scale density depletions and enhanced electric field activity. These were described as lower hybrid solitary structures, distinctively characterized as long-lived structures organized around cylindrical density cavities and solitary only in space [*Chang*, 1993; *Kintner et al.*, 2000; *Schuck et al.*, 2003]. But it was unclear how such structure were originally formed.

Similar spiky electric fields are observed in Polar electric field measurements [*Gurnett et al.*, 1995] by Polar and FAST satellites, which show bipolar structure in the parallel direction and unipolar in the perpendicular direction. One explanation for spiky electric fields involves electron phase-space hole observations, which is a depletion in the electron distribution function that is localized in both position space and velocity space.

Upcoming active experiments may provide opportunity to study aspects of generation of lower hybrid irregularities and nonlinear evolution of the lower hybrid turbulence due to the qualitative similarities just described. The CARE II sounding rocket experiment is planned to be conducted in the F-layer of ionosphere with electric field measurements and particle detectors for the in-situ measurement. First of all, it is important to measure the electric field vector with plasma probes. Three orthogonal electric dipole antennas are expected to measure electric fields simultaneously. The lower hybrid structures excited by the charged

negative dust beam are expected to be observed with spiky electric fields and broad band spectrum near the lower hybrid frequency. The spiky electric fields are expected to be observed by plasma wave detectors. Also, dust particle detectors may measure the dust mass, velocity and mass, which can help understand the dust charging process. In addition to in-situ measurements, the ground-based UHF radars measure electron density irregularities based on Bragg scattering conditions. The electron density and temperature profile in the ionosphere will also be measured simultaneously by radar facilities. Finally, the dust clouds will be observed by optical images. As an active modification experiment in the ionosphere, the CARE II experiment has potential to shed light on a new way of investigating natural phenomena with these diagnostics techniques.

For more applications, the new model could be also extended to study the lower hybrid turbulence generated by ion ring beam in a magnetoplasma [*Scales et al.,* 2012; *Winske and Daughton*, 2012].

5.6 Summary

A computational model for the lower hybrid instability driven by a supersonic charged dust beam is considered in this paper, with inclusion of realistic $\omega_{\rm pe}/\Omega_{\rm ce}$ effects. The nonlinear evolution of such a lower hybrid instability shows the formation of localized electron density depletions coincident with enhanced electric fields. The electron density fluctuation level depends on the ratio of $\omega_{\rm pe}/\Omega_{\rm ce}$. In the parameter regime of the F-layer of the upcoming CARE II experiment, the ratio $\omega_{\rm pe}/\Omega_{\rm ce}$ is about 3, the electron density fluctuation level is predicted to be of order 10%. The electron irregularity size is of the order of $\sim 60\lambda_{di} = 30\,\mathrm{cm}$, which may be measured by ground based UHF radars and propagate off the streaming direction. The characteristics of plasma wave electric fields measured by in-situ plasma probes are predicted to be spiky in structure. The maximum amplitude of the electric fields can be up to $200\,\mathrm{mV/m}$, which is comparable to the maximum electric field amplitude

for spikelet events observed during the MARIE rocket flight [*LaBelle et al.*, 1986]. The temperature increase in ions and dust are also an important factor to measure by in situ measurements. Particle detectors, including ion and dust particles may measure the ion and dust velocity distribution functions. The dust parameters can be measured during the experiment to determine the dust charge properties for accessing irregularity behavior. The in-situ plasma wave investigations measure the spectral and wave vector characteristics of electrostatic waves generated by active sounding rocket experiments predicted here. Ground-based radars may simultaneously measure plasma parameters modified by the injection of the dust grain particles.

A computational model for the lower hybrid streaming instability is the topic of this chapter. The model may also be extended to investigate irregularities at the ion gyro frequency. However if the dust steaming speed is supersonic as is the case considered here, the lower hybrid instability is expected to have the larger wave growth rate. It is also noted if the dust beam is not injected perpendicular to the geomagnetic field, the ion acoustic instability may occur, which has been considered in Chapter 3. The shear-driven instability in the dust cloud boundary [*Bordikar and Scales*, 2012] may drive turbulence near the lower hybrid frequency on shorter time scales such that dust charging is important and will be the subject of Chapter 6.

Chapter 6

Instabilities in an Inhomogeneous Magnetized Dusty Plasma

Plasma irregularities could arise from the boundary layer region between the charged dust clouds and background plasma. In section 6.2, a self-consistent two-dimensional computational model is developed to study irregularities across a magnetic field in an inhomogeneous dust boundary layer in this chapter. The charging process of dust particles has been included in this model, which produces a boundary layer as the source for exciting plasma irregularities. The ambipolar electric field across the boundary provides the source energy for low frequency dust acoustic waves, which may be affected by the magnetic field. The dust acoustic instability occurring at the edge of the cloud boundary layer may lead to dust cloud cross-field diffusion. The ambipolar electric field $\mathbf{E}$ with the magnetic field $\mathbf{B}$ can possibly produce a high electron $\mathbf{E}\times\mathbf{B}$ flow velocity along the boundary (y-direction), which provides energy for high frequency plasma irregularities in the lower hybrid range. Section 6.3 describes computational results for the dust acoustic instabilities (x-direction) in Section 6.3.1 and possible instabilities in y-direction at a later time in Section 6.3.2. The discussion of applications will be given in Section 6.4 and summary will be given in Section 6.5.

6.1 Introduction

When dust cloud particulates exist spatially localized in a plasma background, the dust particles start to charge up to form a boundary layer. The gradient in the density of charged plasma species arises from the charge neutrality at the edge of the dust cloud. When dust clouds start to charge negatively and cause electron density depletion, the ambipolar electric field in the dust could provide source for exciting irregularities.

The dust acoustic wave excitation in the boundary layer in unmagnetized dusty plasmas has been investigated and reported in experiment by several papers [e.g., *Rao et al.*, 1990; *Barkan et al.*, 1995; *Fortov et al.*, 2000; *Trottenberg et al.*, 2006]. In laboratory dusty plasma experiments, the self-excited dust acoustic waves were considered by streaming ions and electrons with ion velocity on the order of the ion acoustic speed along the magnetic field [e.g., *Rosenberg, 1993*; *Rosenberg*, 1996]. *Mahmadian and Scales* [2012] proposed that the dust acoustic wave in an unmagnetized boundary layer plasma could be possibly generated due to electron flow across the boundary using a one-dimensional model. Nevertheless, self-excited dust acoustic wave excitation is attributed to the electric field. With the magnetic field, electrons could be strongly magnetized. In such condition, the cross-field dust acoustic instability may behave quite differently from the unmagnetized dusty plasma. *Rosenberg and Shukla* [2004] examined the effect of a strong magnetic field on the dust acoustic instability by ion streaming along the magnetic field and showed that the growth rate could be reduced under certain conditions.

Plasma instabilities in the lower hybrid frequency range could also occur due to $\mathbf{E}\times\mathbf{B}$ flow and diamagnetic drifts. The dust acoustic turbulence may possibly generate diffusion in the order of ion thermal speed in perpendicular to the magnetic field. The dust expansion across the magnetic field may produce a condition for generating irregularities in the lower hybrid frequency range including electron-ion hybrid (EIH) or shear-driven instability [*Romero et al.,* 1992a; *Romero et al.,* 1992b; *Romero and Ganguli*, 2003; *Scales et al.,* 2012] and the lower-hybrid drift instability [*Davidson et al.*, 1977; *Drake et al.*, 1984; *Winske et*

al., 1989]. Plasma instabilities in the lower hybrid frequency range occurs due to $\mathbf{E}\times\mathbf{B}$ flow and diamagnetic drifts, which will be also investigated in this work.

6.2 Computational Model

In this section, a two-dimensional hybrid model is described to investigate plasma instabilities associated with a dust boundary layer with a charging model, which is extended based on models described in Chapter 5.

Electrons are described by fluid equations in the frame of electrons

$$\frac{\partial n_{\mathrm{e}}}{\partial t} + \nabla \cdot (n_{\mathrm{e}}\mathbf{v}_{\mathrm{e}}) = \frac{dn_e}{dt}|_{\mathrm{charge}} + P_e + L_e \tag{6.1}$$

where

$$\frac{dn_e}{dt}|_{\mathrm{charge}} = -\frac{1}{q_e}\frac{d\rho_{de}}{dt} \tag{6.2}$$

and ρ_{de} is the dust charge density due to electron charging current collection, P_e and L_e is the production and loss of electrons due to photoionization and dissociative recombination. P_e and L_e were ignored in the present work.

The momentum equation of electrons

$$\frac{\partial \mathbf{v}_{\mathrm{e}}}{\partial t} + (\mathbf{v}_{\mathrm{e}} \cdot \nabla)\mathbf{v}_{\mathrm{e}} = \frac{q_{\mathrm{e}}}{m_{\mathrm{e}}}(\mathbf{E} + \mathbf{v}_{\mathrm{e}} \times \mathbf{B}) - \frac{k_{\mathrm{B}}T_{\mathrm{e}}}{m_{\mathrm{e}}}\frac{\nabla n_{\mathrm{e}}}{n_{\mathrm{e}}} - \nu_{\mathrm{en}}(\mathbf{v}_{\mathrm{e}} - \mathbf{v}_{\mathrm{n}}) \tag{6.3}$$

Equations 6.1 and 6.3 are solved spatially with pseudo-spectral methods and a second-order Adams-Bashfourth-Moulton predictor-corrector scheme is used for the time advance. The full Poisson's equation $\epsilon_0\nabla^2\phi = -(q_e n_e + q_i n_i + q_d n_d)$ was solved by spectral methods and the electric field was obtained $\mathbf{E} = -\nabla\phi$.

The dynamics of ions are modeled as discrete particles with the standard particle-in-cell PIC method [*Birdsall and Langdon*, 1991] by integrating the Lorentz force equation. Ignoring the

the production P_i and loss L_i of ions due to photoionization and dissociative recombination, the ion density loss due the ion charging current collection is

$$\frac{dn_i}{dt}|_{\text{charge}} = -\frac{1}{q_i}\frac{d\rho_{di}}{dt} \tag{6.4}$$

and ρ_{di} is the dust charge density due to ion charging current collection. A Monte Carlo model is adopted to realize the ion charging current collection. The probability for removing the jth ion particle is $P_{\text{j}} = dn_{\text{i}}/n_{\text{i}}$, where dn_{i} and n_{i} is the information at the jth particle position. The information at the jth particle position are obtained based on weighted information from neighboring nodes as adopted in PIC method. An event occurs when a uniformly distribution random number on the interval [0 1] is less than the collision probability P_{i}.

The dynamics of dust are modeled as discrete particles with the standard particle-in-cell PIC method. Note the dust has a time variable charge $q_{\text{d}} = Q_{\text{d}}(t) = -Z_{\text{d}}e$. Electrons and ion currents are collected by a spherical grain. In the condition of the dust grain radius less than the shielding length $r_{\text{d}} < \lambda_{\text{d}}$, the time dependent charge on the dust is described with the orbit-limited motion approach [*Bernstein and Rabinowitz*, 1959; *Chen*, 1965]

$$\frac{dQ_{\text{d}}}{dt} = I_{\text{e}} + I_{\text{i}} + I_{\text{p}} \tag{6.5}$$

where I_e and I_i are the electron and ion currents collected by the dust grain and I_p is the photoemission current. Assuming negatively charged dust, the electron and ion currents on a dust grain are given by

$$I_{\text{e}} = \sqrt{8\pi}r_{\text{d}}^2 q_{\text{e}} n_{\text{e}} v_{\text{e}} \exp\left[\frac{-q_{\text{e}}\phi_{\text{f}}}{k_{\text{B}}T_{\text{e}}}\right] \tag{6.6}$$

$$I_{\text{i}} = \sqrt{8\pi}r_{\text{d}}^2 q_{\text{i}} n_{\text{i}} v_{\text{i}} \left[1 - \frac{q_{\text{i}}\phi_{\text{f}}}{k_{\text{B}}T_{\text{i}}}\right] \tag{6.7}$$

$$I_{\text{p}} = -\pi r_{\text{d}}^2 q_{\text{e}} J_{\text{p}} Q_{\text{ab}} Y_{\text{p}} v_{\text{i}} \left[\frac{q_{\text{e}}\phi_{\text{f}}}{k_{\text{B}}T_{\text{p}}}\right] \tag{6.8}$$

The photoemission current is ignored for present work. The equilibrium grain surface floating potential ϕ_{f} is $-3.6k_{\text{B}}T_{\text{e}}/e$ for oxygen plasma and $-2.5k_{\text{B}}T_{\text{e}}/e$ for hydrogen plasma. The equilibrium dust charge state is given by OLM theory as $Z_{\text{d}} \propto r_{\text{d}}|\phi_{\text{f}}/e|$.

In this model, electron and ion densities are taken to be uniform initially. The profile of the dust cloud density is considered in the form

$$n_{\rm d} = n_{\rm d0}[\tanh(\frac{x-x_1}{w}) - \tanh(\frac{x-x_2}{w})] \tag{6.9}$$

where $n_{\rm d0}$ is the unperturbed density of uncharged aerosols, x_1 and x_2 are the location of the right and left boundary of dust cloud respectively, and w is the scale length of the boundary. Aerosols are assumed to have uniform dust radius and mass.

6.3 Simulation Results and Analysis

In this model, the electron and ion density are initialized with equal unperturbed background density $n_{\rm i0} = n_{\rm e0}$. The dust density relative to background plasma density may vary with time depending on applications. An important application is for the ionospheric modification experiment. Plasma parameters at the altitude $\sim 280\,$km are typically as follows. The dominant ion species is O^+, $m_{\rm i}/m_{\rm e} = 16 \times 1836, n_{\rm e0} = n_{\rm i0} = 3 \times 10^{11}\,{\rm m}^{-3}, {\rm T_e} = {\rm T_i} = {\rm T_d} = 0.1\,$eV and $B = 0.5\,$G. The ion Debye length is $\lambda_{\rm di} \sim 0.4\,$cm in the unperturbed plasma and the ion plasma frequency is $\omega_{\rm pi} \sim 1.8 \times 10^5\,$rad/s. The dust charging time could be roughly estimated based on $\tau_{\rm c} = \omega_{\rm pi}^{-1}(\lambda_{\rm d}/r_{\rm d})$ [see e.g., *Shukla and Mamun*, 2002; *Rosenberg et al.,* 2011]. The charging time is $\sim 0.005\,$s for a dust grain of radius $r_{\rm d} = 4\,\mu$m, that corresponds to the equilibrium charge number $Z_{\rm d0} = 1000$ correspondingly. The charging time is $\sim 0.02\,$s for $r_{\rm d} = 1\,\mu$m, which corresponds to the equilibrium charge number $Z_{\rm d0} = 250$. The dust plasma frequency $\omega_{\rm pd}$ is $\sim 52.6\,$rad/s for the dust mass $m_{\rm d} = 10^{10} m_{\rm i}$, the dust density $n_{\rm d} = 0.00085 n_{\rm e}$, and the dust charge number $Z_{\rm d} = 1000$. The dust time scale is estimated to be $\sim 0.019\,$s while the ion time scale is $\sim 5.5 \times 10^{-6}\,$s. The dust charging time is therefore approximately on the order of the dust time scale.

All quantities in the simulation are normalized to the ion initial quantities. Lengths are normalized to the ion Debye length, temperature to the initial ion temperature, frequencies or time to the initial ion plasma frequency, and velocities to the initial ion thermal velocity. In

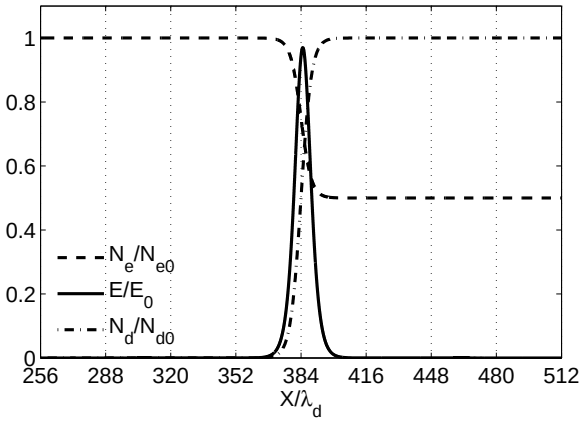

Figure 6.1: Schematic representation of the boundary layer problem in the X-Z simulation plane.

the simulation, the simulation domain has $L_{\rm x} = 1024\lambda_{\rm d}$ with 1024 grid cells and $L_{\rm y} = 256\lambda_{\rm d}$ with 256 cells with periodic boundary conditions in both dimensions. In each grid cell $dx = dy = \lambda_{\rm d}$, there are 25 particles for each species (i.e. ions and dust), respectively. The initially uncharged dust cloud occupies about $256\lambda_{\rm d} \times 256\lambda_{\rm d}$ with a certain boundary scale length. Figure 6.1 shows a schematic representation of the dust boundary layer simulation sketching the profile of electron density, the ambipolar electric field, and dust density with a scale length $w = 5.12\lambda_{\rm d}$. The ambipolar electric field rises on the edge of the boundary layer and becomes stronger with a sharp gradient.

To make the simulation feasible, we choose the ion and electron mass ratio $m_{\rm i}/m_{\rm e} = 1836$ for H^+ and the dust and ion mass ratio $\sim m_d/m_i = 10^5$ to include the dust dynamics in the simulation without loss of generality. Results are consistent with cases for atomic hydrogen H^+ and atomic oxygen O^+. The ratio of the dust plasma frequency to the ion plasma frequency $\omega_{\rm pd}/\omega_{\rm pi}$ is 0.092 in the simulation. The time step is chosen to be $\omega_{\rm pi}\Delta t = 0.004$ in order to insure adequate energy conservation and low noise level in the simulation.

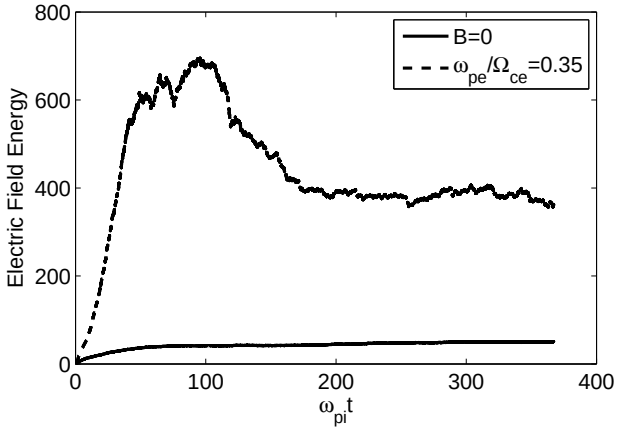

Figure 6.2: The time evolution of the electrostatic field energy(normalized) for three different values of the ratio $\omega_{\rm pe}/\Omega_{\rm ce} \to \infty (B = 0)$, and $\omega_{\rm pe}/\Omega_{\rm ce} = 0.35$ with electron and neutral collision frequency $\nu_{\rm en}/\omega_{pi} = 0.1$.

6.3.1 Dust Acoustic Instability

The time evolution of the total electrostatic field energy is shown in Figure 6.2 for $\omega_{\rm pe}/\Omega_{\rm ce} \to \infty (B = 0)$ and $\omega_{\rm pe}/\Omega_{\rm ce} = 0.35$ with electron and neutral collision frequency $\nu_{\rm en}/\omega_{\rm pi} = 0.1$. The variation of the ratio $\omega_{\rm pe}/\Omega_{\rm ce}$ is achieved by changing the magnetic field only. The wave energy mainly concentrates in the $\hat{x}$ direction, which is the density gradient direction across the boundary layer. One of the features observed is that the time to obtain the maximum electrostatic energy reduced if the magnetic field is included. The required time continues to decrease further with the frequency ratio $\omega_{\rm pe}/\Omega_{\rm ce}$ reduced. Results indicate that if a ratio $\omega_{\rm pe}/\Omega_{\rm ce} \gg 1$, it will produce the field energy development similarly as the unmagnetized case. The maximum electrostatic field energy saturates at a high level by enhancing the magnetic field.

For the case unmagnetized $B = 0$ **or** $\omega_{\rm pe}/\Omega_{\rm ce} >> 1$

In an unmagnetized dusty plasma, for the dust acoustic wave in the regime $\omega \gg kv_{\rm d}$, the dust acoustic wave frequency

$$\omega = kc_{\rm D}/(1 + k^2\lambda_{\rm D}^2)^{1/2} \tag{6.10}$$

where $c_{\rm D} = \omega_{\rm pd}\lambda_{\rm D}$ is the dust acoustic speed. In the long wavelength $k^2\lambda_{\rm D}^2 \ll 1$, the dust acoustic frequency is $\omega = kc_{\rm D}$ [*Rao et al.*, 1990]. The wavelength of the dust acoustic wave is of the order $\sim 10\lambda_{\rm di}$ in the simulation. The frequency power spectrum of the electric field for the dust acoustic wave is maximized near the dust plasma frequency. Using these parameters, the dust acoustic phase velocity in the simulation is $v_{\rm p} = \omega/k \simeq 0.5\omega_{\rm pd}/k_{\rm x} = 0.0918v_{\rm i}$, which agrees with the dust acoustic phase speed approximately given by $c_{\rm DA} = Z_{\rm d0}v_{\rm i}(n_{\rm d0}/n_{\rm i0})^{1/2}(m_{\rm i}/m_{\rm d})^{1/2} = 0.0922v_{\rm i}$ in the long-wavelength limit $k^2\lambda_{\rm D}^2 \ll 1$ [*Shukla and Mamun*, 2002].

Figure 6.3 depicts a one-dimensional X cross section of electron density $n_{\rm e}/n_{\rm e0}$, ion density $n_{\rm i}/n_{\rm i0}$, dust density $n_{\rm d}/n_{\rm d0}$, and the density difference $(n_{\rm e} - n_{\rm i} + n_{\rm d}Z_{\rm d})/n_0$, and the ambipolar electric field $E_{\rm x}$ in the top panel and electron flow velocity $v_{\rm ex}$, ion flow velocity $v_{\rm ix}/v_{\rm i}$ and dust flow velocity $v_{\rm dx}/v_{\rm i}$ for $\omega_{\rm pe}/\Omega_{\rm ce} \to \infty (B = 0)$ with $\nu_{\rm en}/\omega_{\rm pi} = 0.1$. In general, when the dust start to charge negatively, the electron density depletion forms with a boundary layer while the ion density depletion percentage is relatively small because of lower mobility. Note the maximum electric field corresponds to where the total plasma density profile changes sign based on Gauss's law. The wave electric field to the first order charge densities is $\partial E/\partial x = (e/\epsilon_0)(n_{\rm i} - n_{\rm e} - n_{\rm d}Z_{\rm d})$. The resulting charge separation gives rise to an electric field pointing inward the center of the dust clouds. The maximum electric fields correspond to the maximum negative electron flow velocity in the $\hat{x}$ direction before waves develop. The dust density inhomogeneity provides the ambipolar field as the energy source for wave instabilities. For Boltzmann behavior for the electrons, the electric field in the $\hat{x}$ direction is approximately $E_x \approx (k_{\rm B}T_{\rm e}/q_{\rm e})(\partial \log n_{\rm e}/\partial x)$[*Scales and Ganguli*, 2004b]. The electron drift flow velocity in the $\hat{x}$ direction is approximately given by $v_{\rm ex} = q_{\rm e}E_{\rm x}/m_{\rm e}\nu_{\rm en}$ in an

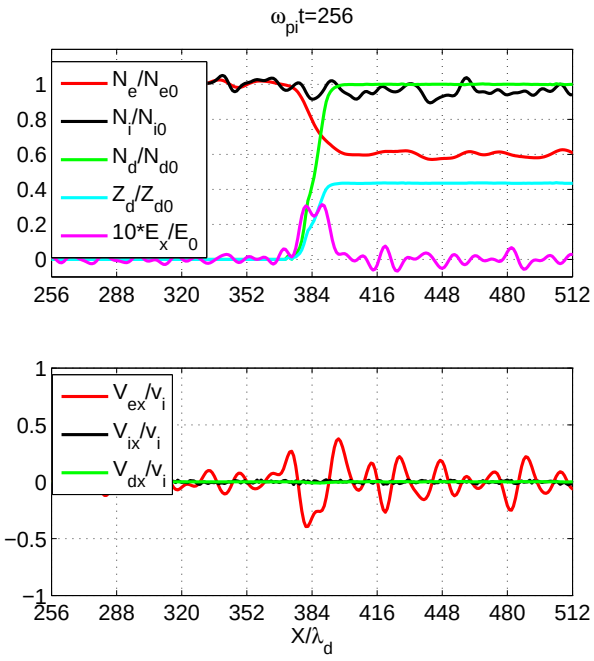

Figure 6.3: One-dimensional X cross section of electron density, ion density, dust density, dust charge number density, the density difference, electric field (top) and the electron flow velocity, ion flow velocity and the dust flow velocity (bottom) for $\omega_{\rm pe}/\Omega_{\rm ce} \to \infty (B = 0)$.

unmagnetized plasma.

When waves start to develop at time $\omega_{\rm pi}t = 256$, the electron flow velocity $v_{\rm ex}$ is $0.5v_{\rm i}$ above the dust acoustic phase speed as shown in Figure 6.3. At this time, there is no obviously net ion flow and dust flow simultaneously in the boundary regime. The dust acoustic wave starts to develop initially at the point where the ambipolar field is the maximum and then propagates inwards the dust clouds as will shown later. The mechanism for exciting the dust acoustic wave is possibly the electron flow velocity driven by sufficiently large electric field in unmagnetized dusty plasmas, which agrees with work by *Mahmadian and Scales* [2011].

The linear analysis described by *Mahmadian and Scales* [2011] shows that the threshold for exciting the dust acoustic instability is the electron flow velocity above the dust acoustic phase speed. The linear dispersion relation

$$1 + \chi_{\rm e} + \chi_{\rm i} + \chi_{\rm d} = 0 \tag{6.11}$$

where

$$\chi_{\rm e} = \frac{1}{k^2\lambda_{\rm De}^2}[1 + \xi_{\rm e}Z(\xi_{\rm e})][1 + \frac{i\nu_{\rm en}}{\sqrt{2}kv_{\rm e}}Z(\chi_{\rm e})]^{-1}$$
$$\chi_{\rm i} = \frac{1}{k^2\lambda_{\rm Di}^2}[1 + \xi_{\rm i}Z(\xi_{\rm i})][1 + \frac{i\nu_{\rm in}}{\sqrt{2}kv_{\rm i}}Z(\chi_{\rm i})]^{-1}$$
$$\chi_{\rm d} = \frac{1}{k^2\lambda_{\rm Dd}^2}[1 + \xi_{\rm d}Z(\xi_{\rm d})][1 + \frac{i\nu_{\rm dn}}{\sqrt{2}kv_{\rm d}}Z(\chi_{\rm d})]^{-1}$$

Here, $\lambda_{{\rm d}\alpha}$, v_α, $\nu_{\alpha{\rm n}}$ are the Debye length, thermal speed, and collision frequency, T_α, m_α are temperature and mass, respectively, and Z is the plasma dispersion function. Note $\xi_{\rm e} = (\omega - kv_{\rm ex} + i\nu_{\rm en})/(\sqrt{2}kv_{\rm e})$, $\xi_{\rm i} = (\omega - kv_{\rm ix} + i\nu_{\rm in})/(\sqrt{2}kv_{\rm i})$, $\xi_{\rm d} = (\omega - kv_{\rm dx} + i\nu_{\rm dn})/(\sqrt{2}kv_{\rm d})$, where $v_{\alpha{\rm x}}$ is the flow velocity of the α plasma species.

For the case $\omega_{\rm pe}/\Omega_{\rm ce} < 1$

Assuming $\omega_{\rm pe}/\Omega_{\rm ce} << 1$, electrons are strongly magnetized. Magnetic fields confine electrons moving cross the magnetic field. Figure 6.4 shows one-dimensional X cross section plot of

electron density n_e/n_{e0}, ion density n_i/n_{i0}, dust density n_d/n_{d0}, and the density difference $(n_e - n_i + n_d Z_d)/n_0$, the electric field E_x/E_0 and the electron, ion and dust flow velocity for $\omega_{pe}/\Omega_{ce} = 0.35$ with electron and neutral collision frequency $\nu_{en}/\omega_{pi} = 0.1$ at time $\omega_{pi}t = 88$. This time corresponds to that when the dust acoustic wave starts to develop. The maximum amplitude of the ambipolar electric field becomes stronger in comparison to the unmagnetized case in Figure 6.3. The electric field E_x becomes stronger while the electron flow velocity v_{ex} in the $\hat{x}$ direction becomes smaller using the perpendicular electron flow velocity approximately $v_{ex} = E_y/B_z + (k_B T_e/n_e m_e)(\partial n_e/\partial y)$ without any collisions. The density fluctuation level in the linear regime is suppressed if the frequency ratio ω_{pe}/Ω_{ce} further reduces. For the strongly magnetized case $\omega_{pe}/\Omega_{ce} = 0.35$ with $\nu_{en}/\omega_{pi} = 0.1$, the electron flow velocity threshold drops to $v_{ex}/v_i = 0.05$ below the dust acoustic sound speed. For a even smaller ratio $\omega_{pe}/\Omega_{ce} < 0.2$ without any electron and neutral collisions, there is no substantial net electron and ion flow, but a dust drift velocity is observed. When electrons are unable to traverse across the magnetic field, we propose that the dust flow velocity could possibly provide the energy source for exciting dust acoustic waves. Further theory will be developed in the future work.

Figure 6.5 shows a two-dimensional plot of electron density n_e/n_{e0}, ion density n_i/n_{i0}, dust density n_d/n_{d0} and the dust charge number Z_d/Z_{d0} for $\omega_{pe}/\Omega_{ce} = 0.35$ at two different times $\omega_{pi}t = 160$ and $\omega_{pi}t = 336$. At a linear time stage $\omega_{pi}t = 160$, the dust acoustic density fluctuation start to be observed, which propagates towards the dust boundary layer center. As the dust acoustic wave develops, such dust density wave structures in the boundary layer will lead to diffusion of dust clouds across the magnetic fields. For a strongly magnetized case, the dust acoustic instability results in a fast diffusion rate of the dust clouds across the magnetic field. The resulting dust diffusion velocity could be a portion of the ion thermal velocity. The dust acoustic wave development causes the dust cloud layer expanding, that leads to the formation of a negatively charged dust drift beam as potential important factor for exciting instabilities in the $\hat{y}$ direction. At a later time $\omega_{pi}t = 336$, it is noted that electron density structure may appear in the $\hat{y}$ direction simultaneously with the dust acoustic wave,

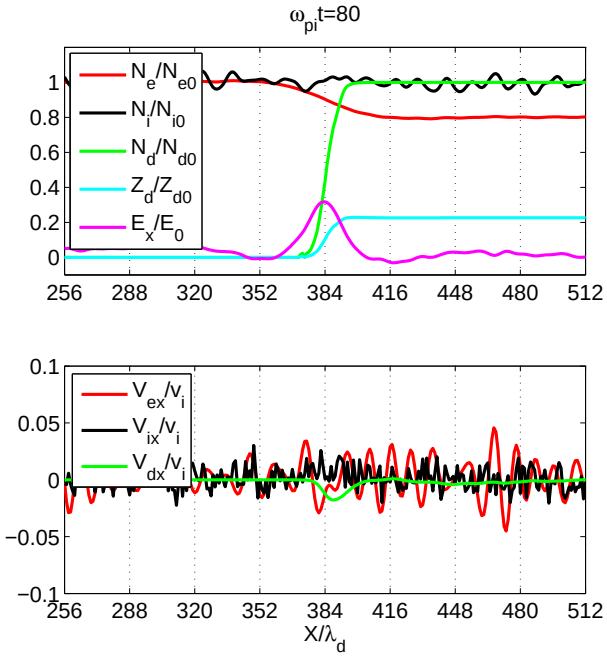

Figure 6.4: One-dimensional X cross section of electron density, ion density, dust density, dust charge number density, the density difference, electric field (top) and the electron flow velocity, ion flow velocity and the dust flow velocity for $\omega_{\rm pe}/\Omega_{\rm ce} = 0.35$ (bottom).

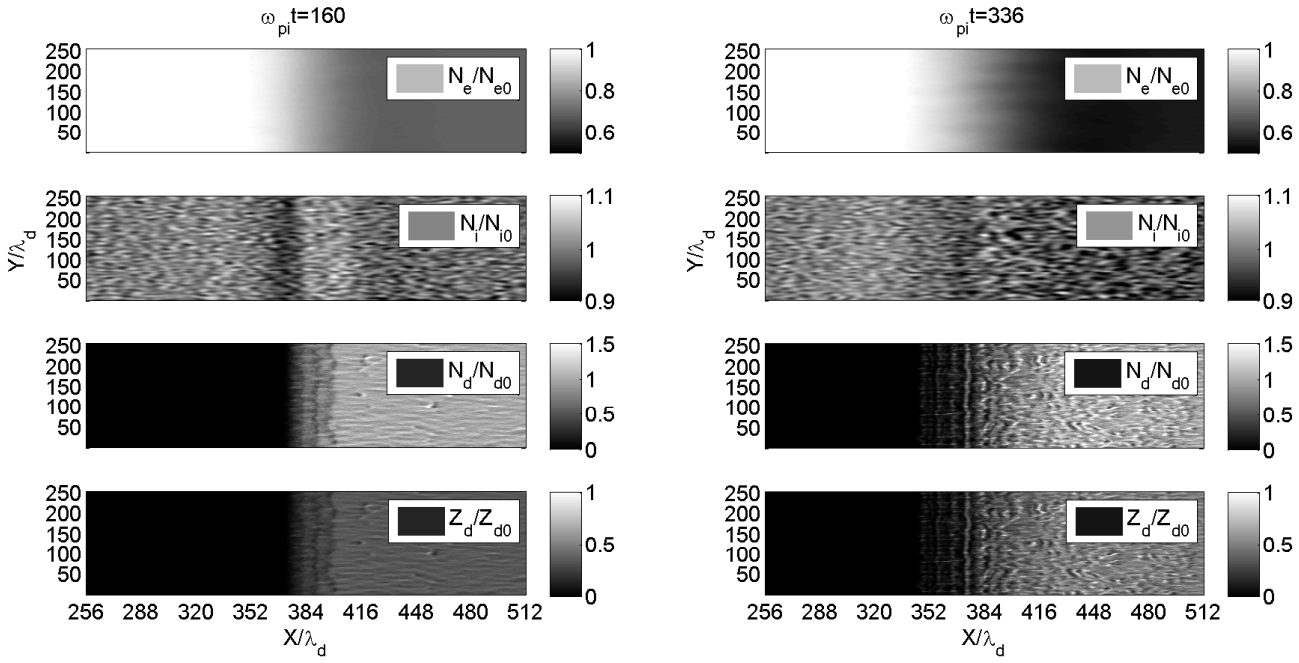

Figure 6.5: Two-dimensional plot of electron density, ion density, dust density and dust charge number density at two different times $\omega_{\rm pi} = 160$ (left) and $\omega_{\rm pi} = 336$(right).

which exhibits similar characteristics for instabilities due to electron flow as will discussed in the next section.

Electron magnetization plays an important role on the evolution of the dust acoustic waves. The excitation mechanism in a magnetized dusty plasma for the dust acoustic waves may be distinguished from the unmagnetized dusty plasma. The transition of strongly magnetized electron to weakly magnetized electrons could be achieved through varying the magnetic field amplitude and the ratio $\omega_{\rm pe}/\Omega_{\rm ce}$ correspondingly. Another important factor of impacting electron dynamics is the electron and neutral collision effect, particularly for a strongly magnetized case $\omega_{\rm pe}/\Omega_{\rm ce} = 0.35$ as shown in Figure 6.6. When $\nu_{\rm en}/\omega_{\rm pi} >> 1$, the dynamics of a strongly magnetized electron suffices to an unmagnetized electron dynamics. The electron and neutral collision frequency behaves differently for the electron motion in the unmagnetized case and magnetized case. Electron and neutral collisions weaken the maximum amplitude of ambipolar electric field and enhances the electron diffusion in the boundary

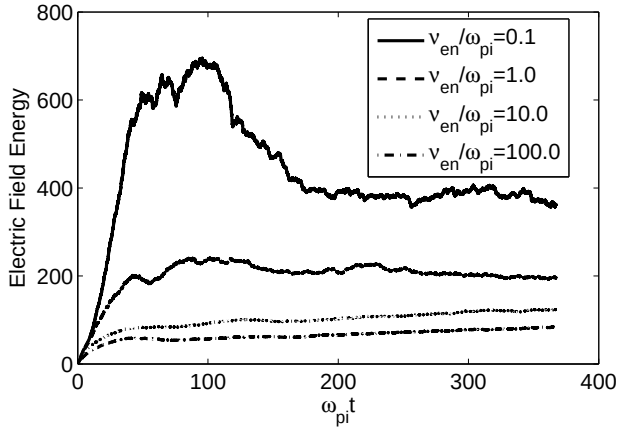

Figure 6.6: The electron and neutral collision effect on the field energy development for $\omega_{pe}/\Omega_{ce} = 0.15$.

layer region across a magnetic field.

6.3.2 Instabilities due to Electron Cross Flow

The $\mathbf{E}\times\mathbf{B}$ flow and diamagnetic drifts may provide the energy source for the electron-ion-hybrid mode and lower-hybrid drift instability. With dust expansion arising from the dust acoustic instability, it provides a condition to stimulate shear-driven instability for expanding dust clouds [*Scales et al.,* 2012]. The dust expansion speed serves as the role of keeping the boundary condition sharp. In this section, we will study the shear-driven instability with a diffusively expansion speed on the order of the ion thermal speed, which may occur at a time when dust expansion and sharp boundary establishes in previous section. Starting from a equilibrium stage, this section aims to describe the fundamental characteristics of irregularities in the $\hat{y}$ direction near the lower hybrid frequency.

Romero et al. [1992b] shows that a sheared electron cross-field flow excites the electron-ion-hybrid mode if $\kappa = \omega_{\rm S}/\omega_{\rm LH} > 1$ and coherent structures longer than the electron gyro radius; for $\kappa = \omega_{\rm S}/\omega_{\rm LH} < 1$ the lower-hybrid drift instability dominates with short wavelength near the order of electron gyro radius [*Drake et al.,* 1984] and there is no vortex formation. The

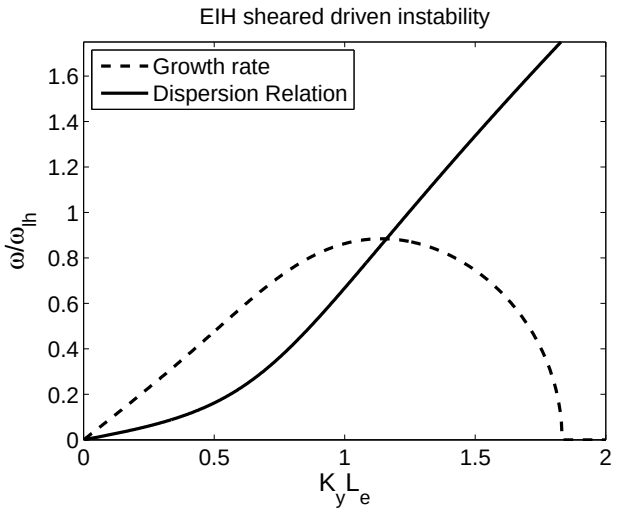

Figure 6.7: Linear growth rate and real frequency calculation for the shear-driven or EIH instability in the boundary layer of the expanding dust cloud.

shear frequency is defined $\omega_s = V_0/L_{\rm E}$, where V_0 is the peak electron flow velocity and $L_{\rm E}$ represents the flow's shear scale length. The scale length of the electron flow is generally considered in the range $\rho_{\rm e} < L_{\rm E} < \rho_{\rm i}$ to study the shear driven instability [*Romero and Ganguli*, 2003], which is the case for our simulation. These instabilities due to electron cross flow are high frequency in the range of lower hybrid frequency compared to the dust acoustic frequency.

The mechanism for the EIH instability in perpendicular to the magnetic field is the electron flow velocity $v_{\rm ey}$. The local dispersion relation in frequency ω and wavenumber $k_{\rm y}$ for this instability has been described previously [*Scales et al.,* 2010]

$$\tilde{\omega}^4 + (\frac{\delta_{\rm i}}{\tilde{k}_{\rm y}} S - \frac{\alpha_{\rm i}}{\delta_{\rm i}} \tilde{k}_{\rm y})\tilde{\omega}^3 - \tilde{\omega}^2 + \frac{\alpha_{\rm i}}{\delta_{\rm i}} \tilde{k}_{\rm y} \tilde{\omega} = 0 \tag{6.12}$$

where $\tilde{\omega} = \omega/\omega_{\rm lh}$, $\tilde{k}_{\rm y} = k_{\rm y} L_{\rm E}$, $\delta_{\rm i} = \omega_{\rm pi}/\Omega_{\rm ci}$, $S = L_{\rm E}/L_{\rm N}$ and $\alpha_{\rm i} = v_{\rm ey}/\Omega_{\rm ci} L_{\rm E}$, where $L_{\rm E} = (dv_{\rm ey}/dx)/v_{\rm ey0}$ is the electron flow velocity shear scale length, $v_{\rm ey}$ is the electron drift flow velocity along the boundary and $L_{\rm N} = (dn_{\rm e0}/dx)/n_{\rm e0}$ is the electron density gradient scale length. This EIH instability generates turbulence in the range of lower hybrid frequency $\omega_{\rm lh}$. Figure 6.7 shows the calculated linear growth rate and wave frequency. It is observed

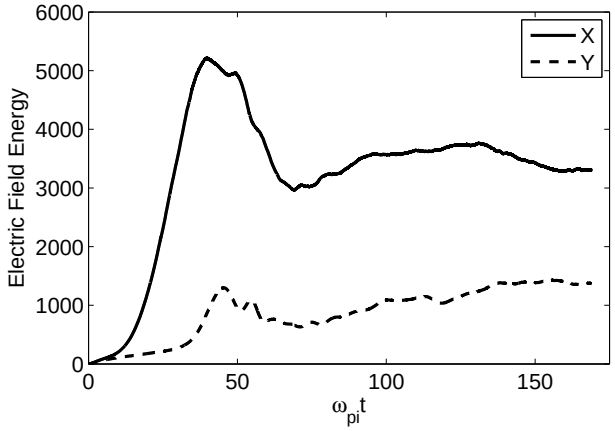

Figure 6.8: Time evolution of the electrostatic field energy for EIH instability for the ratio $\omega_{pe}/\omega_{ce} = 0.15$.

that the frequency at maximum linear growth is near $\omega_{\rm lh}$ and the wave growth rate of the order $\sim \omega_{\rm lh}$. The wave growth rate is maximized for $k_y L_{\rm E} \sim 1$ which implies the wavelength $\lambda \sim L_{\rm E}$. The wavelength of the waves is determined by the gradient scale length $L_{\rm E}$ of the electron flow V_E as shown in several references [e.g., *Chae et al.*, 2000; *Scales et al.,* 2012].

Figure 6.8 shows the time evolution of the electric field energy for $\omega_{\rm pe}/\Omega_{\rm ce} = 0.15$. The energy in the ambipolar electric field $E_{\rm x}$ grows initially and the resulting highly sheared $\mathbf{E}\times\mathbf{B}$ electron flow in the $\hat{y}$ direction provides free energy for the development of lower-hybrid waves. Subsequently, the $E_{\rm y}$ electric field grows due to the development of the EIH instability. The simulation wave frequency and wave growth rate agrees with linear analysis. Waves saturate when vortex starts to develop in electron dynamics.

Figure 6.9 shows one-dimensional X cross section plot of electron density $n_{\rm e}/n_{\rm e0}$, ion density $n_{\rm i}/n_{\rm i0}$, dust density $n_{\rm d}/n_{\rm d0}$, the electron flow velocity $V_{\rm ey}$ and two dimensional electron density structures at two different times $\omega_{\rm pi}t = 40$ and $\omega_{\rm pi}t = 56$. Waves start to grow linearly and then saturate. At a linear time $\omega_{\rm pi}t = 40$, the maximum electron flow velocity reaches up to $v_{\rm ey}/v_{\rm i} = 10$. The mode number $m_y = 8$ is observed in plasma density structure at a linear stage. When waves saturate at a time $\omega_{\rm pi}t = 56$, vortex structures start to

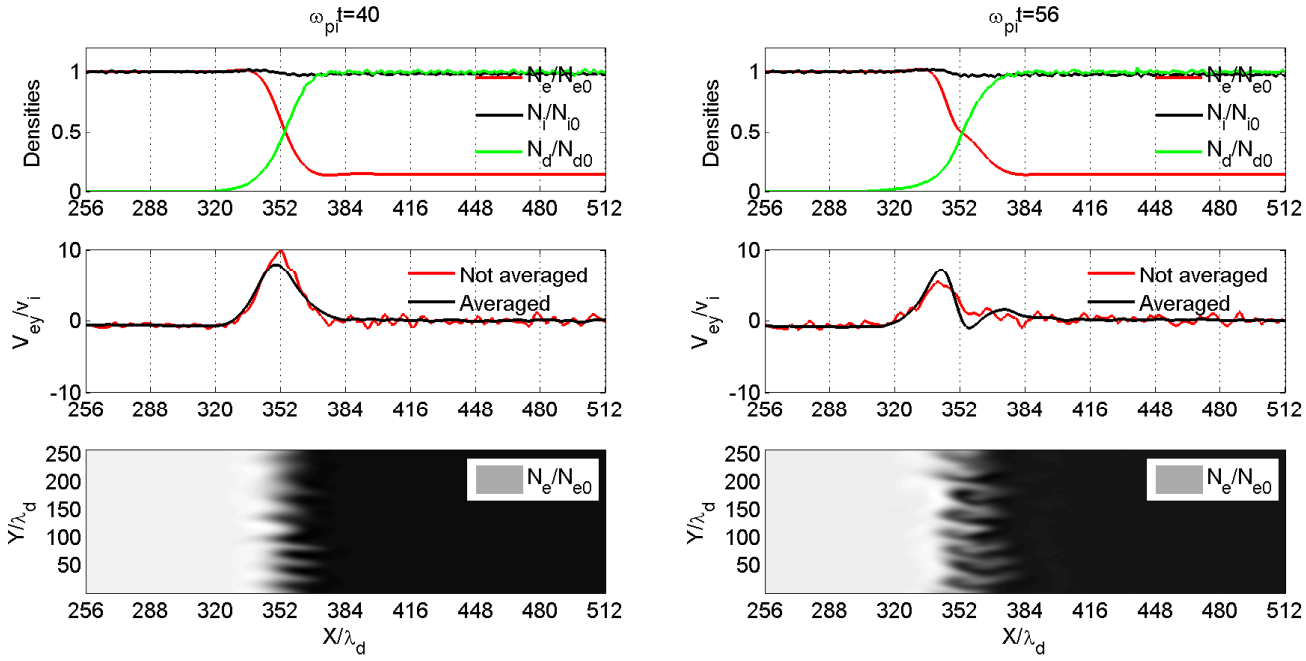

Figure 6.9: One-dimensional plot of densities, electron flow in the y direction and two dimensional electron structures at two different times $\omega_{\rm pi} = 40$ (left) and $\omega_{\rm pi} = 56$ (right)

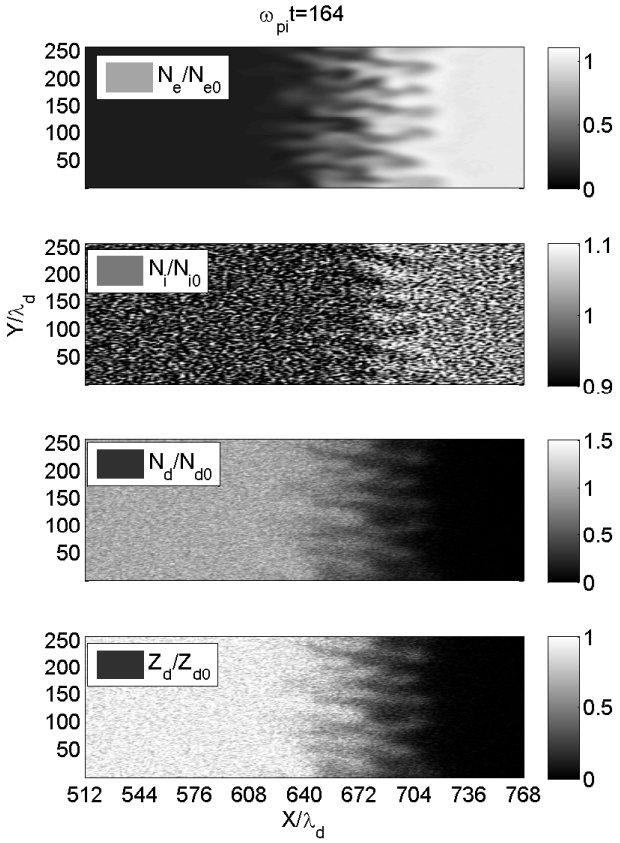

Figure 6.10: Two-dimensional plot of electron density, ion density, dust density and dust charge number density at time $\omega_{\rm pi}t = 164$

develop. The shear-driven instability produces the vortex-like structure of the order of the velocity shear scales size.

Figure 6.10 shows two-dimensional plot of electron density $n_{\rm e}/n_{\rm e0}$, ion density $n_{\rm i}/n_{\rm i0}$, dust density $n_{\rm d}/n_{\rm d0}$ and the dust charge number $Z_{\rm d}/Z_{\rm d0}$ for $\omega_{\rm pe}/\Omega_{\rm ce} = 0.15$ at a late time. At a later time $\omega_{\rm pi}t = 164$, fluctuation structures in the $\hat{y}$ direction are observed in the electron density, ion density structure as well as dust density and dust charge number. It is noted that nonlinear wave structures in electron density are clearly observed.

The excitation of shear-driven instability will depend on the boundary condition, magnetic

fields, the dust parameters as well as collision effects. However, this section provides a feasible and efficient methodology to study such shear-driven structure in order to compare structures that are observed simultaneously with dust acoustic wave excitation in a boundary layer. It is noted that the shear-driven instability with dust expanding due to the dust acoustic wave shows similar characteristics for a diffusively expansion model as discussed. These features observed by this new model agree well with our past work by assuming strongly magnetized electrons $\omega_{\rm pe}/\Omega_{\rm ce} \to 0$.

6.4 Discussion of Applications

For the CARE experiment, the gradient of the dust cloud edge and the sharpness of electron density gradient are important factors to determine the turbulence in a boundary layer. The electron density depletion is determined by the dust parameters such as dust density, dust particle size and the dust charging process. A sharp electron density gradient will be favorable for exciting these instabilities. On one hand, the dust acoustic wave will possibly occur on the edge of the dust cloud, which propagate into the center of the clouds. Also, the dust acoustic turbulence may cause dust heating and anomalous diffusion. Note that the dust acoustic wave may be quenched by the dust and neutral collisions as shown by *Mahmadian and Scales* [2012]. On the other hand, in perpendicular to geomagnetic field, the shear-driven instability may also occur along the boundary. It is noted that the shear-driven instability depends on the magnetic field and electron density depletion significantly. The shear-driven instability may cause a relative large electron density fluctuation compared to the electron fluctuation caused by the dust acoustic wave , which will highly depend on the electron density depletion gradient. The size of shear-driven instability is on the order of electron flow scale length. The shear-driven instability will also cause fluctuations in ion density, dust density and dust charge number.

Another important application will be in the category of laboratory dusty plasma. Most

laboratory dusty plasma wave have been studied in unmagnetized conditions. The new laboratory facilities are under development, which will have the capability to study the magnetic field effect on dusty plasmas. The self-consistent model developed in this work has the capability of describing the dust charging process, unmagnetized and magnetized plasma dynamics and wave excitation in an inhomogeneous magnetized dusty plasma environment. This model will have great potential application for magnetized dusty plasmas as the next frontier for complex plasma research with upcoming experiment facilities [*Thomas Jr et al.*, 2012].

The boundary layer problem could occur in various cases such as the polar mesosphere region, active space ionospheric and magnetospheric modification experiment, the earth's magnetospheric boundary layers, and laboratory dusty plasmas [e.g., *Cho and Kelly*, 1993; *Bernhardt et al.,* 2011; *Bernhardt et al.,* 2012; *Galvez et al.*, 1988; *Barkan*, 1995]. This model could also be extended to study phenomena related to boundary layer effects in a traditional plasma environment.

6.5 Summary

A new hybrid two-dimensional model has been developed to investigate possible instabilities in a nonuniform magnetized dusty plasmas. A charging model has been adopted to deal with the dust grain charging process. A simple but efficient algorithm is adopted to deal with ion current collection in the particle-in-cell method. The dust acoustic instability produced in the boundary layer has been investigated with magnetic field effects. The localized dust clouds produce electron density depletion due to the dust negatively charging process. The ambipolar electric field provides the energy source for exciting the dust acoustic wave and lower hybrid shear-driven instability. The magnetic fields impact both dust acoustic wave and lower hybrid shear-driven instability. The excitation mechanism for such dust acoustic waves in a unmagnetized/magnetized dusty plasma has been compared and discussed. The

dust acoustic wave may cause the dust cloud anomalous diffusion across the magnetic field. The dust cloud expansion leads to a lower hybrid shear-driven instability in the $\hat{y}$ produced simultaneously with the dust acoustic wave in the $\hat{x}$ direction in the plane perpendicular to the magnetic field. Important features of high frequency shear-driven instability have also been studied by this new model.

Chapter 7

Conclusion and Future Work

7.1 Conclusion

Active charged aerosol release experiments in space provide an alternate way to study plasma irregularities created in dusty space plasmas with radar diagnostics and in-situ measurements. The future charged aerosol experiment CARE will continue efforts to investigate plasma irregularities generation in space dusty plasma environment. A follow-on CARE II mission is planned for launch from Andoya, Norway in 2013.

The research work has presented an analysis of plasma irregularity generation during the charged aerosol release experiment. The formation, evolution and saturation of possible plasma irregularities have also been characterized for plasma wave detection and radar measurement. Similarities exist with past passive space observations of nonlinear irregularity structures as well as with observations in the PMSE source region. Also, the work suggest parameter regimes for the future charged aerosol release experiment (CARE II). The mechanisms of possible irregularities have been summarized in Table 7.1.

The sounding rocket launching site determines the geometry of the dust injection direction with respect to the geomagnetic field. It is important to conduct such an experiment at a

Table 7.1: Summary of each instability in geometry

Instability	Mechanism	Propagation
Ion Acoustic(IA)	Dust beam along B	Along or off B
Dust Acoustic(DA)	Ion beam along B	Along/off B
Lower Hybrid streaming (LH-streaming)	Dust Beam perp to B	Perp to B
Dust Acoustic Wave (DAW)	Electron flow in Boundary	Along/off B
Lower Hybrid sheared (LH-sheared)	$E \times B$ electron flow	Perp to ExB

location with ground radar and satellite orbit coverage. The first experiment occurred at Wallops island, VA. The dust injection direction is not quite along or in perpendicular to the magnetic field. The second sounding rocket mission will take place at a higher latitude in Norway or at Poker Flat, Alaska. The dust injection direction will be mostly along the geomagnetic field. Depending on the exhaust release direction relative to the geomagnetic field, different irregularities could be generated as summarized in Table 7.1. If the dust are injected perpendicular to the magnetic field, lower-hybrid streaming instability will occur most likely inside the clouds. Also, the dust acoustic wave may start to develop at the leading edge of the dust clouds and then propagate towards the clouds. The lower-hybrid shear-driven instability could occur at the regions where the boundary layer gradient are in perpendicular to the geomagnetic field. When the dust expansion direction is along the magnetic field, the ion acoustic instability will be the most likely candidate for generating plasma irregularities and enhanced radar echoes. The dust acoustic wave instability may still occur starting from the dust cloud boundary layer. The wave propagation direction will be impacted by the dust expansion speed, which is important for radar measurement. The dust expansion speed $V_{\mathrm{d}}/v_i = 3$ will be preferred in terms of exciting strong plasma irregularities and a broad aspect angle range for radars.

The optimum release time for the charge aerosol release depends on the experimental purpose. The launch windows requires clear sky at observations site, moon below horizon, and sun at

12 to 18 degree depression angle. Also, sporadic-E should not be observed one hour before launch. The CARE I sounding rocket launching time was carefully chosen at the sunset in summer, when PMSEs usually occur in this season. At sunset, the photoemission by solar rays become less important in comparison to a day time experiment. Also, the night time experiment is favorable for optical instrument to operate. The altitude of dust clouds injection happens in the F-layer of the ionosphere. The dust clouds will settle down at a lower altitude afterwards due to force balance. The motion of the dust clouds can be tracked by instruments on satellites. Artificially released clouds are expected to produce similar phenomenon as natural dust clouds and PMSEs radar echoes.

If the sounding rocket occurs in a daytime experiment, the photoemission current may need to be considered as an important factor. The photoemission current needs to be evaluated carefully in comparison to the electron collection current to determine the dust grain charging process as discussed by *Rosenberg et al.* [2011]. The photoemission process if dominant may produce positively charged dust grain particles.

Ionospheric modification in the F region of the ionosphere is expected due to interaction between injected dust clouds and neutral gases with background plasmas. The effect of the dust generator of the sounding rocket could be ignored. The electron density depletion could occur by the charging process of injected dust particles (Al_2O_3) as well as due to interaction between neutral gases with background plasmas. We expect that the electron density depletion will be produced and mainly caused by the electron attachment material (dust grains) within the time period ~ 1 second. The size of dust grain particles ranges from 10 nm to several μm. Large dust grains with higher dust density will be better for producing electron density depletion and plasma irregularities. If irregularities develop, the dust charge number fluctuation may be observed. With in-situ dust detectors, the dust size and the dust charge number can be measured to contribute understanding such fundamental dusty environment in the ionosphere. The dust particles from the rocket exhaust may become the condensation nuclei for the formation of ice particles. The dust particle size detection with in-situ measurement could be used to compare measurement by ground radars. Meteoric

smoke particles in the D-region (approximately between 70 and 90 km) could be measured by radars using a method described by *Fentzke et al.*, [2009]. This technique has been proved at lower latitude using dual-beam Arecibo UHF observations [*Fentzke et al.,* 2009] and at high latitude using the Poker Flat Incoherent Scatter Radar (PFISR) [*Fentzke et al.,* 2012].

The motor firing time depends on the wave growth rate and interaction time between injected particles and background plasmas. Most plasma irregularities summarized in Table 7.2 have a wave growing period of the order 1 s. The firing time in the future CARE II experiment will be reduced to 2 s from 17.8 s in order to generate strongly concentrated dense modification effect. It is noted the dusty plasma assumption will not be valid when the intergrain distance becomes greater than the Debye length, that occurs for a sparse dust grain environment. The dust charge number will vary with time during the charging process. After firing, most irregularities occur during the next following several seconds, so it is important to make observations continuously. The duration time of the electron density depletion region will also impact small scale electron irregularity structures.

The irregularity size ranges in 10′s of cm to meters as summarized in Table 7.2. The EISCAT operates three incoherent scatter radar systems, at 224 MHz, 931 MHz in Northern Scandinavia and one at 500 MHz on Svalbard. The UHF 931 MHz radar can operate at vertical and magnetic zenith case and the VHF 224 MHz at vertical beam only now. For these radars, the radar are sensitive to irregularities at a radar half wavelength $\lambda = 16$ cm for 931 MHz, $\lambda = 67$ cm for 224 MHz and $\lambda = 30$ cm for 599 MHz. The radar Doppler spectra is an important factor to identify since plasma irregularities in a dusty plasma environment may modify the ion acoustic phase speed due to nonlinear wave and particle interaction. The CUTLASS coherent HF radars operate in the range $8 \sim 20$ MHz at Hankasalmi, Finland and Pykkvibar, Iceland. The HF radars have angle dependence for Bragg backscattering from irregularities, which require that the radio wave vector $\mathbf{k}$ is closely orthogonal to the magnetic field. More instruments may also be used to provide comprehensive diagnostics.

A full set of plasma diagnostics will be equipped in the CARE II mission to measure the

Table 7.2: Summary of characteristics for each instability

Instability	Frequency/Growth	Wavelength	Phase Speed	Electric Field
LH-sheared	$\sim$ 5kHz /0.001 s	10's of cm	$\sim$ 2km/s	10's of mV/m
IA	$\sim$ 30kHz /1 s	10's of cm	$\sim$ 2km/s	10's of mV/m
DA	$\sim$ 5Hz /1 s	10's of cm	$<$ 10 m/s	10's of mV/m
DAW	$\sim$ 5kHz /1 s	10's of cm	$<$ 10 m/s	10's of mV/m

charged dust density, the electron and ion densities, as well as electric fields associated with plasma waves produced by the release. Obtained spectra of density fluctuations will be useful to calculate scattering cross-section for different types of excited wave turbulence in comparison to radar measurement. Also, dust properties including the dust temperature, dust particle size and dust charge number will be explored, that will provide information about dust particulate characteristics embedded in a plasma environment. Nonlinear features that have been predicted in this work will be expected to observe such as localized electron density depletion, enhanced electric fields, particle heating and a broadband of frequency power spectral and etc.

In summary, plasma irregularities generation during the charged aerosol release experiment has been studied theoretically and computationally to support future experimental design and observations. The next experiment in the future will test some of our results in this work by experimental observations.

7.2 Future Work

Neutral gas dynamics will be incorporated by a Direct Simulation Monte Carlo (DSMC) model, that helps understanding neutral turbulence as well as collision effects. The distributions of solid rocket particulates in the rocket exhaust will be considered. The electron

temperature variation will be included in this work. A more accurate charging model including photoemission is also possible in a magnetized plasma environment. A three dimensional electromagnetic full PIC model with parallel computation may be expected in the future. Radar scatter in a dusty plasma with beams will be also investigated by electromagnetic theory.

The most desired work will be a self-consistent model to include neutral gas dynamics and dust aerosol particle injection, the dust charging process, the charged dust beam and ion beam formation and plasma irregularity generation. The neutral gas dynamics could be dealt by a Direct Simulation Monte Carlo model, which will help understanding important neutral gases dynamics and how plasma beam during such experiment may form properly.

Bibliography

[1] Appleton, E. V., and M. A. F. Barnett (1926), On same direct evidence for downward atmospheric reflection of electric rays, *Proc: Roy. SOC. (London)*, *109*, 621-641.

[2] Backhouse, T. W. (1885), The luminous cirrus cloud of June and July, *Meteorol. Mag.*, *20*, 133.

[3] Barkan, A., R. L. Merlino, and N. D'Angelo (1995), Laboratory observation of the dust-acoustic wave mode, *Phys. Plasmas*, *2*, 3563-3565.

[4] Baker, D. N. (2000), Effects of the Sun on the Earths environment, *J. Atmos. Sol. Terr. Phys., 62*, 1669-1691.

[5] Balsley, B. B., W. L. Ecklund, D. C. Fritts (1983), Vhf echoes from the high-latitude mesosphere and lower thermosphere: observations and interpretations, *J. Atmos. Sci., 40*, 2451-2466.

[6] Barnes, C., M. K. Hudson, and W. Lotko (1985), Weak double layers in ion acoustic turbulence, *Phys. Fluids*, *28*, 1055.

[7] Bernhardt, P. A. (1984), Chemistry and dynamics of SF6 injections into the F region, *J. Geophys. Res., 89*, 3929.

[8] Bernhardt, P. A. (1987a), A critical comparison of ionospheric depletion chemicals, *J. Geophys. Res., 92*, 4617-4628.

[9] Bernhardt, P. A., and L. M. Duncan, Ionospheric focused heating-A hybrid modification experiment (1987b), *J. Atmos. Terr. Phys., 49*, 1107-1117.

[10] Bernhardt, P. A., W. E. Swartz, M. C. Kelley, M. P. Sulzer, and S. T. Noble (1988), Spacelab 2 upper atmospheric modification experiment over Arecibo, 2, plasma dynamics, *Astrophys. Lett. Commun.*, *27*, 3, 183198.

[11] Bernhardt, P. A., P. Rodriguez, C. L. Siefering, and C. S. Lin (1991), Field-aligned dynamics of chemically induced perturbations to the ionosphere, *J. Geophys. Res., 96*, 13887.

[12] Bernhardt, P. A., J. D. Huba, P. K. Chaturvedi, J. A. Fulford, P. A. Forsyth, D. N. Anderson, and S. T. Zalesak (1993), Analysis of rocket beacon transmissions for computerized reconstruction of ionospheric densities, *Radio Sci.*, *28*, 613 - 627, doi:10.1029/93RS00383.

[13] Bernhardt, P. A., G. Ganguli, M. C. Kelley, and W. E. Swartz (1995), Enhanced radar backscatter from space shuttle exhaust in the ionosphere, *J. Geophys. Res., 100* (A12), 23,811-23,8185.

[14] Bernhardt, P. A., C. L. Siefring, P. Rodriguez, D. G. Haas, M. M. Baumback, H. A. Romero, D. A. Solin, F. T. Djuth, L. M. Duncan, D. E. Hunton, C. J. Pollock, M. P. Sulzer, C. A. Tepley, L. S. Wagner, J. A. Goldstein (1995), The ionospheric focused heating experiment, *J. Geophys. Res.*, *100(A9)*, 17,331-17,345, doi:10.1029/94JA01887.

[15] Bernhardt, P. A. (2009), An update on charged aerosol release experiment CARE, presented at *AGU Fall 2009 meeting*, San Francisco, CA.

[16] Bernhardt, P. A., J. B. Baumgardner, A. N. Bhatt, P. E. Erickson, M. F. Larsen, T. R. Pedersen, and C. L. Siefring (2011) , Optical emissions observed during the charged aerosol release experiment (CARE I) in the ionosphere, *IEEE Trans. Plasma Sci., 39*, 2774-2775, doi: 10.1109/TPS.2011.216494.

[17] Bernhardt, P. A., J. B. Baumgardner, A. N. Bhatt, A. Coster, P. J. Erickson, C. R. Kaplan, R. A. Haaser, M. F. Larsen, F. D. Lind, T. R. Pedersen, R. F. Pfaff, P. A. Roddy, S. P. Rodriquez, P. W. Schuck, C. L. Siefring, S. M. Smith, E. R. Talaat, and J. F. Thomason (2012), Ground and space-based measurement of rocket engine burns in the ionosphere, *IEEE Trans. Plasma Sci., 40*, 1267-1286.

[18] Bernstein, I. B. and I. N. Rabinowitz (1959), Theory of electrostatic probes in a low-density plasma, *Phys. Fluids*, *2*, 112.

[19] Bingham, R., V. D. Shapiro, P. K. Shukla, and R. Trines (2004), Lower-hybrid wave activity and reconnection at the Magnetosphere, *Phys. Scr., T113*, 144-148, doi:10.1238/Physica.Topical.113a00144

[20] Bingham, R., U. De Angelis, V.N. Tsytovich, and O. Havne (1991), Electromagnetic wave scattering in dusty plasmas, *Phys. Fluids B*,*3*, 811.

[21] Birdsall, C. K., and A. B. Langdon (1991), *Plasma Physics via Computer Simulation* , New York: McGraw-Hill.

[22] Birdsall, C. K. (1991), Particle-in-cell charged-particle simulations, plus Monte Carlo collisions with neutral atoms, PIC-MCC, *IEEE Trans. Plasma Sci., 19*, 65-85.

[23] Booker, H. C. (1961), A local reduction of F-region ionization due to missile transit, *J. Ceophys. Res., 66*, 1073.

[24] Bordikar, M. R., and W. A. Scales (2012), Lower hybrid turbulence associated with creation of dusty plasmas in the near-earth space environment, *IEEE Trans. Plasma Sci., 40*, 946-953.

[25] Breit G., and M. Tuve (1926), A test of the existence of the conducting layer, *Phys. Rev.*, *28*, 554-573; also, A radio method for estimating the height of the ionosphere conducting layer (1925), *Nature*, *116*, 357.

[26] Canuto, C., M. Y. Hussaini, A. Quarteroni, and T. A. Zang (1988), *Spectral Methods in Fluid Dynamics*, Springer-Verlag Berlin, Heidelberg.

[27] Chae, G. S., W. A. Scales, G. Ganguli, P. A. Bernhardt and M. Lampe (2000), Numerical model for low-frequency ion waves in magnetized dusty plasmas, *IEEE Trans. Plasma Sci., 28*, 1694-1705, doi: 10.1109/27.901256.

[28] Chang, T. (1993), Lower-hybrid collapse, caviton turbulence, and charged particle energization in the topside aurora1 ionosphere and magnetosphere, *Phys. Fluids B, 5*, 2646-2656, doi: 10.1063/1.860702.

[29] Chapman, S. ,The absorption and dissociative or ionizing effect of monochromatic radiation in an atmosphere on a rotating earth, *Proc. Roy. SOC. (London)*, *43*, 2645, 1931; also, The absorption and dissociative or ionizing effect of monochromatic radiation in an atmosphere on a rotating earth Part II: Grazing incidence, *Proc. Roy. Soc. (London)*, *43*, 484-501, 1931.

[30] Chen, F. F. (1965), *Plasma diagnostic techniques* ed R H Huddlestone and S L Leonard, chp 4, New York: Academic

[31] Cho, J. Y. N., T. M. Hall, and M. C. Kelley (1992), On the role of charged aerosols in polar mesosphere summer echoes, *J. Geophys. Res., 97*, 875.

[32] Cho, J. Y. N. and M. C. Kelley (1993), Polar mesospheric summer radar echoes: Observations and current theories, *Rev. Geophys.*, *31*, 243-265.

[33] D'Angelo, N. (1990), Low-frequency electrostatic waves in dusty plasmas, *Planet. Space Sci. 38* 1143-1146.

[34] Davidson, R. C., N. T. Gladd, C. S. Wu, and J. D. Huba (1977), Effects of finite plasma beta on the lower-hybrid-drift Instability, *Phys. Fluids*, *20*, 301.

[35] Drake, J. F., P. N. Guzdar, A. B. Hassam, and J. D. Huba (1984), Nonlinear mode coupling theory of the lower-hybrid-drift instability, *Phys. Fluids*, *27*, 1148.

[36] Dyson, P. L., J. P. McClure, and W. B. Hanson (1974), In situ measurements of the spectral characteristics of F region ionospheric irregularities, *J. Geophys. Res., 79*, 10, 1497-1502, doi:10.1029/JA079i010p01497.

[37] Eklund, W. L., and B. B. Balsley (1981), Long-term observations of the Artic mesophere with MST radar at Poker Flat, Alaska, *J. Geophys. Res.*, *86*, 7775.

[38] Ergun, R. E., et al. (1998a), FAST satellite observations of electric field sturcutres in the auroral zone, *Geophys. Res. Lett.*,*25*, 2025.

[39] Ergun, R. E., C. W. Carlson, J. P. McFadden, F. S. Mozer, L. Muschietti, and I. Roth (1998b), Debye-scale plasma structures associated with magnetic-field-aligned electric fields, *Phys. Rev. Lett.*, *81*, 826.

[40] Eriksson, A. I., B. Holback, P. O. Dovner, R. Bostram, G. Holmgren, M. Andre, L. Eliasson, and P. M. Kintner (1994), FREJA observations of correlated small-scale density depletions and enhanced lower hybrid waves, *Geophys. Res. Lett., 21*, 1843-1846, doi:10.1029/94GL00174.

[41] Evans, J. V. (1969), Theory and practice of ionosphere study by Thomson scatter radar, *Proceedings of the IEEE , 57*, 496-530, doi: 10.1109/PROC.1969.7005

[42] Fortov, V. E. , A. G. Khrapak, S. A. Khrapak, V. I. Molotkov, A. P. Nefedov, O. F. Petrov, and V. M. Torchinsky (2000), Mechanism of dust-acoustic instability in a direct current glow discharge plasma, *Phys. Plasmas*, *7*, 1374.

[43] Fortov, V. E. E., Ivlev, A. V., Khrapak, S. A., Khrapak, A. G., and Morfill, G. E. (2005). Complex (dusty) plasmas: Current status, open issues, perspectives. *Physics reports, 421*, 1, 1-103.

[44] Fentzke, J.T., D. Janches, I. Strelnikova and M. Rapp (2009), Meteoric smoke particle properties derived using dual-beam Arecibo UHF observations of D-region spectra during different seasons,*J. Atmos. Sol. Terr. Phys.*, *71*, 1982 -1991.

[45] Fentzke, J. T., V. Hsu, C. G. M. Brum, I. Strelnikova, M. Rapp, and M. Nicolls (2012), D region meteoric smoke and neutral temperature retrieval using the poker flat incoherent scatter radar, *Geophys. Res. Lett.*, *39*, L21102, doi:10.1029/2012GL053841

[46] Fu, H., and W. A. Scales (2011), Nonlinear evolution of the ion acoustic instability in artificially created dusty space plasmas, *J. Geophys. Res., 116*, A10315, doi:10.1029/2011JA016825.

[47] Fu, H., and W. A. Scales (2012), Nonlinear evolution of the dust acoustic instability in artificially created dusty space plasmas, *IEEE Trans. Plasma Sci., 40*, 1223-1228, doi: 10.1109/TPS.2011.2180929.

[48] Gadsden, M. (1990), A secular change in noctilucent cloud occurrence, *J. Atmos. Terr. Phys., 52*, 247-251.

[49] Galvez, M., S. P. Gary, C. Barnes and D. Winske (1988), Computer simulations of plasma expansion across a magnetic field, *Phys. Fluids*, *31*, 1554.

[50] Ganguli, G., P. A. Bernhardt, W. A. Scales, P. Rodriguez, C. L. Siefring, and H. A. Romero, Physics of negative ion plasmas created by chemical releases in space, in Physics of Space Plasmas, SPI Conf. Proc. and Reprint Ser., vol. 12, edited by T. Chang, pp. 161-183, Scientific, Cambridge, Mass., 1993.

[51] Gore, A. (1992), *Earth in the Balance: Ecology and the Human Spirit*, Houghton Mifflin, Boston, Mass.

[52] Goss, S., L. Hespel, P. Gossart, and A. Delfou (2006), Morphological characterization and particle sizing of alumina particles in solid rocket motor, *J. Propul. Power, 22*, 127-135.

[53] Gray, P. C., M. K. Hudson, W. Lotko, and R. Bergmann (1991), Decay of ion beam driven by acoustic waves into ion holes, *Geophys. Res. Lett., 18*, 1675-1678, doi:10.1029/91GL02089.

[54] Gurnett, D. A., A. M. Persoon, R. F. Randall, D. L. Odem, S. L. Remington, T. F. Averkamp, M. M. Debower, G. B. Hospodarsky, R. L. Huff, D. L. Kirchner, M. A. Mitchell, B. T. Pham, J. R. Phillips, W. L. Schintler, P. Sheyko, and D. R. Tomash (1995), The Polar Plasma Wave Instrument, *Space Sci. Rev., 71*, 597-622.

[55] Hagfors, T. (1992), Note on the scattering of electromagnetic waves from charged dust particles in a plasma, *J. Atmos. Terr. Phys., 54*, 333-338.

[56] Hockney, R. W. ,and J. W. Eastwood (1981), *Computer Simulation Using Particles*. New York: McGraw-Hill.

[57] Huba, J. D., N. T. Gladd, and K. Papadopoulos (1978), Lower-hybrid-drift wave turbulence in the distant magnetotail, *J. Geophys. Res., 83(A11)*, 5217-5226, doi:10.1029/JA083iA11p05217.

[58] Jana, M. R., A. Sen, and P. K. Kaw (1993), Collective effects due to charge fluctuation dynamics in a dusty plasma, *Phys. Rev. E., 48*, 3930-3933.

[59] Jackson, J. E., H. A. Whale, and S.J. Bauer (1962), Local ionospheric disturbance created by a burning rocket, *J. Geophys. Res.*, *67*, 2059-2061.

[60] Jesse, O. (1887), Die Hohe der leuchtenden (silbernen) Wolken, *Meteorol. Z.*, *4*, 424.

[61] Karimabadi, H., N. Omidi, and K. B. Quest (1991), Two-dimensional simulations of the ion/ion acoustic instability and electrostatic shocks, *J. Geophys Res.*, *18*, 1813-1816.

[62] Kelley, M. C., D. T. Farley, and J. Rottger (1987), The effect of cluster ions on anomalous VHF backscatter from the summer polar mesosphere, *Geophys. Res. Lett.*, *14*, 1031.

[63] Kintner, P. M., P. W. Schuck and J. R. Franz (2000), Spaced measurements and progress in understanding space plasma waves, *Phys. Plasmas, 7*, 2135-2141, doi: 10.1063/1.874033.

[64] Kintner, P. M., J. Vago, S. Chesney, R. L. Arnoldy, K. A. Lynch, C. J. Pollock and T. E. Moore (1992), Localized lower hybrid acceleration of ionospheric plasma, *Phys. Rev. Lett., 68*, 2448-2451, doi: 10.1103/PhysRevLett.68.2448.

[65] Koskinen, H. E. J., R. Lundin, and B. Holback (1990), On the plasma environment of solitary waves and weak double layers, *J. Geophys. Res., 95*, 5921-5929, doi:10.1029/JA095iA05p05921.

[66] Labelle, J., and P. M. Kintner (1986), Large amplitude wave packets observed in the ionosphere in association with transverse ion acceleration, *J. Geophys. Res., 91*, 7113-7118, doi:10.1029/JA091iA06p07113.

[67] Maharaj, S. K., S. R. Pillay, R. Bharuthram,S. V. Singh and G. S. Lakhina (2004), The effect of dust grain temperature and dust streaming on electrostatic solitary structures in a non-thermal plasma, *Phys. Scr., T113*, 135-140, doi:10.1088/0031-8949/2004/T113/034.

[68] Mahmoudian, A. and W. A. Scales (2012), Irregularity excitation associated with charged dust cloud boundary layers, *J. Geophys. Res.*, *117*, A02304, doi:10.1029/2011JA017204.

[69] McAdams, K. L., J. Labelle, P. W. Schuck, and P. M. Kintner (1998), PHAZE II observations of lower hybrid burst structures occurring on density gradients, *Geophys. Res. Lett., 25*, 3091-3094, doi:10.1029/98GL02424.

[70] Mendillo, M., G. S. Hawkins, and J.A. Klobuchar (1975a), A Large-Scale Hole in the Ionosphere Caused by the Launch of Skylab, *Science*, *187*, 343.

[71] Mendillo, M., G. S. Hawkins, and J. A. Klobuchar (1975b), A sudden vanishing of the ionospheric F region due to the launch of Skylab, *J. Geophys. Res., 80*, 2217-2228, doi:10.1029/JA080i016p02217.

[72] Mendillo, M., D. Rote, and P. A. Bernhardt (1980), Preliminary report on the HEAO hole in the ionosphere, *Eos Trans. AGU*, *61*, 529-530.

[73] Mendillo, M., and J. Baumgardner (1982), Optical signature of an ionospheric hole, *Geophys. Res. Lett., 9*, 215 - 218, doi:10.1029/GL009i003p00215.

[74] Mendillo, M. (1988), Ionospheric holes: A review of theory and recent experiments, *Adv. Space Res., 8*, 51-62.

[75] Mendillo, M., S. M. Smith, A. Coster, P. Erickson, J. Baumgardner, and C. Martinis (2008), Man-made space weather, *Space Weather, 6*, S09001, DOI:10.1029/2008SW000406.

[76] Melrose, D. B. (1986), *Instabilities in Space and Laboratory Plasmas*, pp. 5052, Cambridge Univ. Press, New York.

[77] Merlino, R. L., A. Barkan, C. Thompson, and N. D'Angelo (1998), Laboratory studies of waves and instabilities in dusty plasmas, *Phys. Plasmas.*, *5*, 1607-1614.

[78] Merlino, R. L., A. Barkan, C. Thompson, and N. D. Angelo (1997), Experiments on waves and instabilities in dusty plasmas, *Plasma Phys. Controlled Fusion*, *39*, 421

[79] Mozer, F. S., R. Ergun, and M. Temerin (1997), New features of time domain electric field structures in the auroral acceleration region, *Phys. Rev. Lett.*, *79*, 1281.

[80] Mueller, A. C., and D. J. Kessler (1985), The effects of particulates from solid rocket motors fired in space, *Adv. Space. Res., 5*, 77-86, doi:10.1016/0273-1177(85)90389-8.

[81] Omidi, N. , K. Akimoto, D. A. Gurnett, and R. R. Anderson (1988), Nature and the nonlinear evolution of electrostatic waves associated with the AMPTE solar wind releases, *J. Geophys Res.*, *93*, 8532-8544.

[82] Orszag, S. A. (1972a), Comparison of pseudospectral and spectral approximation, *Stud. Appl. Math*, *51*, 253-259.

[83] Orszag, S. A. (1972b), Numerical simulation of incompressible flows within simple boundaries: accuracy, *J. Fluid Mech*, *49*, 75-112

[84] Orszag, S. A. (1972c), Numerical simulation of incompressible flows within simple boundaries. I. Galerkin (spectral) representations, *Studies in Appl. Math.*, *50*, 395.

[85] Ozeki M. and K. Heki (2010), Ionospheric holes made by ballistic missiles from North Korea detected with a Japanese dense GPS array, *J. Geophys. Res., 115*, A09314, DOI:10.1029/2010JA015531.

[86] Pcseli, H. L., K. Iranpour, O. Holter, B. Lybekk, J. Holtet, J. Trulsen, A. Eriksson, and B. Holback, Lower hybrid wave cavities detected by the FREJA satellite (1996), *J. Geophys. Res., 101*, 5299-5316, doi:10.1029/95JA03127.

[87] Patacchini, L., I. H. Hutchinson, and G. Lapenta (2007), Electron collection by a negatively charged sphere in a collisionless magnetoplasma, *Phys. Plasmas*, *14*, 062111.

[88] Piel, A., M. Klindworth, O. Arp, A. Melzer, and M. Wolter (2006), Obliquely propagating dust-density plasma waves in the presence of an ion beam, *Phys. Rev. Lett.* , *97*, 205009-1-205009-4.

[89] Piel, A., O. Arp, M. Klindworth, and A. Melzer (2008), Obliquely propagation dust density waves," *Phys. Rev. E.*, *77*, 026407-1-026407-7.

[90] Platov, Y. V., S. A. Chernouss, and M. J. Kosch (2004), Classification of gasdust formations from rocket exhaust in the upper atmosphere, *J. Spacecr. Rockets*, *41*, 667.

[91] Pokhotelov, O. A., O. G. Onishchenko, P. K. Shukla, and L. Stenflo (1999), Drift-Alfven vortices in dusty plasmas, *J. Geophys. Res., 104(A9)*, 19,797-19, 800, doi:10.1029/1999JA900221.

[92] Rao, N. N., P. K. Shukla, and M. Y. Yu (1990), Dust-acoustic waves in dusty plasmas, *Planet Space Sci.*, *38*, 543-546.

[93] Rapp, M., and Lubken, F. J. (2004). Polar mesosphere summer echoes (PMSE): Review of observations and current understanding. *Atmos Chem. Phys.*, *4*, 4777-4876.

[94] Reddy, R. V., G. S. Lakhina, N. Singh, and R. Bharuthram (2002), Spiky parallel electrostatic ion cyclotron and ion acoustic waves, *Nonlinear Proc. Geophys.*, *9*, 25.

[95] Retterer, J. M. (1997), A model for particle acceleration in lower hybrid collapse, *Phys. Plasmas, 4*, 2357-2364, doi: 10.1063/1.872217.

[96] Romero, H. , G. Ganguli, Y. C. Lee and P. J. Palmadesso (1992a), Electronion hybrid instabilities driven by velocity shear in a magnetized plasma, *Phys. Fluids B*, *4*, 1708.

[97] Romero, H. G. Ganguli and Y. C. Lee (1992b), Ion acceleration and coherent structures generated by lower hybrid shear-driven instabilities, *Phys. Rev. Lett.*, *69*, 3503.

[98] Romero, H. and G. Ganguli (1993), Nonlinear evolution of a strongly sheared cross-field plasma flow, *Phys. Fluids B 5*, 3163.

[99] Rosenberg, N. W., Project Firefly 1962-1963, *Environmental Research Papers*, No. 15, FACRL-64-364, May 1964.

[100] Rosenberg M. (1993), Ion and dust-acoustic instabilities in dusty plasmas, *Planet. Space Sci.* , *41*, 229-233.

[101] Rosenberg M. (1996), Ion-dust streaming instability in processing plasmas, *J. Vac. Sci. Technol. A*, *14*, 631-633.

[102] Rosenberg, M., M. Salimullah, and R. Bharuthram, Lower hybrid instability driven by charged dust beam (1999), *Planet. Space Sci., 47*, 1517-1519.

[103] Rosenberg M., and P. K. Shukla (2000), Low-frequency Hall current instability in a dusty plasma, *J. Geophys Res.*, *105*, 23135-23139.

[104] Rosenberg M.,andP.K. Shukla (2004), Iondusttwostreaminstabilityinacollisionalmagnetizeddustyplasma, *ournalofPlasmaPhysics*,*70*,317322.

[105] Rosenberg, M., P. A. Bernhardt, and S. E. Clark (2011), Excitation of ion waves by charged dust beams in ionospheric aerosol release experiments, *Planet. Space Sci., 59*, 312-318, doi:10.1016/j.pss.2010.11.01.

[106] Sato, T., and H. Okuda (1981), Numerical simulations on ion acoustic doubler layers, *J. Geophys. Res.*, *86*, 3357

[107] Scales, W. A., P. A. Bernhardt, and G. Ganguli, Simulations of negative ion clouds and electron density depletions produced during electron attachment chemical release experiments, in Physics of Space Plasmas, SPI Conf. Proc. and Reprint Ser., vol. 12, edited by T. Chang, pp. 597-608, Scientific, Cambridge, Mass., 1993.

[108] Scales, W. A., P. A. Bernhardt, G. Ganguli, C. L. Siefring, and P. Rodriguez (1994), Small-scale plasma irregularities produced during electron attachment chemical releases, *Geophys. Res. Lett.*, *21*, 605-608.

[109] Scales, W. A., P. A. Bernhardt, and G. Ganguli (1995), Early time evolution of a chemically produced electron depletion, *J. Geophys. Res.*, *100*, 269-280.

[110] Scales, W. , and G. Chae (2003), Nonlinear evolution of dust waves driven by ionospheric cross-field electron currents, *Geophys. Res. Lett.*, *30*, 1157.

[111] Scales, W. (2004a), Nonlinear development of a low-frequency Hall current instability in a dusty plasma, *Phys Scripta.*, *T107*, 107-112.

[112] Scales, W. A., and G. Ganguli (2004b), Electrodynamic structure of charged dust clouds in the Earth's middle atmosphere, *New J. Phys., 6*, 12.

[113] Scales, W. A., M. R. Bordikar, A. Mahmoudian, and H. Fu (2010), Irregularities associated with creation of dusty plasmas in the near-earth space environment, *IEEE Trans. Plasma Sci., 38*, 880-885, doi:10.1029/94JA02490.

[114] Scales, W. A., G. Ganguli, L. Rudakov, and M. Mithaiwala (2012), Model for nonlinear evolution of localized ion ring beam in magnetoplasma, *Phys. Plasmas*, *19*, 062902, doi: 10.1063/1.4729330

[115] Schmidlin, F. J. (1992), First observation of mesopause temperatures lower than 100 K, *Geophys. Res. Lett., 19*, 1643.

[116] Schuck, P. W., C. E. Seyler, J. -L. Pinco, J. W. Bonnell, and P. M. Kintner (1998), Theory, simulation, and observation of discrete eigenmodes associated with lower hybrid solitary structures, *J. Geophys. Res., 103*, A4, 6935-6953, doi:10.1029/97JA02922.

[117] Schuck, P. W., J. W. Bonnell, and P. M. Kintner (2003), A review of lower hybrid solitary structures, *IEEE Trans. Plasma Sci., 31*, 1125-1177, doi: 10.1109/TPS.2003.822043.

[118] Selwyn, G. S. (1994), Optical characterization of particle traps, *Plasma Sources Sci. Tehcnol.*, *3*, 340.

[119] Seyler, C. E. (1994), Lower hybrid wave phenomena associated with density depletions, *J. Geophys. Res., 99*, 19, 513-19, 525, doi:10.1029/94JA01572.

[120] Seyler, C. E. and J. Providakes (1987), Particle and fluid simulations of resistive current-driven electrostatic ion cyclotron waves, *Phys. Fluids, 30*, 3113-3128, doi:10.1063/1.866487.

[121] Shapiro, V. D., V. I. Shevchenko, G. I. Solovev, V. P. Kalinin, R. Bingham, R. Z. Sagdeev, M. Ashora-Abdalla, J. Dawson, and J. J. Su (1993), Wave collapse at the lower hybrid resonance, *Phys. Fluids B, 5*, 9, 31483162.

[122] Shukla, P. K., R. Bingham, R.O. Dendy, H. Pecseli, and L. Stenflo (1995), Nonlinear Structures in Space and Laboratory Plasmas, *J. Phys. IV France, 5*, C6-19.

[123] Shukla, P. K. (2001), A survey of dusty plasma physics, *Phys. Plasmas, 8*, 1791, doi: 10.1063/1.1343087

[124] Shukla, P. K., and A. A. Mamun (2002), *Introduction to Dusty Plasma Physics*, Inst. of Phys., Bristol, U. K.

[125] Smith, B. A. (1982), A new look at the Saturn system: The Voyager-2 images, *Science*, *215*, 504-537.

[126] Stone, R. (1991), Signs of wet weather in the polar mesosphere?, *Science, 255*, 1488.

[127] Tajima, T. (1989), *Computational Plasma Physics: With Applications to Fusion and Astrophysics, Frontiers in Phys.*, vol. 72, Addison-Wesley, Redwood City, Calif.

[128] Temerin, M., M. Woldorff, and F. S. Mozer (1979), Nonlinear steepening of the electrostatic ion cyclotron wave, *Phys. Rev. Lett.*, *43*, 1941.

[129] Thomas, G. E. (1991), Mesospheric clouds and the physics of the mesopause region, *Rev. Geophys., 29*, 553.

[130] Thomas, L., I. Astin, and I. T. Prichard (1992), The characteristics of VHF echoes from the summer mesopause region at mid-latitudes, *J. Atmos. Terr. Phys., 54*, 969.

[131] Thomas Jr, E., R. L. Merlino and M. Rosenberg (2012), Magnetized dusty plasmas: the next frontier for complex plasma research, *Plasma Phys. Control. Fusion 54*, 124034

[132] Trottenberg, T. , D. Block, and A. Piel (2006), Dust confinement and dust-acoustic waves in weakly magnetized anodic plasmas, *Phys. Plasmas*, *13*, 042105.

[133] Tsytovich, V. N., Winter (1998), J. , On the role of dust in fusion devices, *Phys. Usp., 41*, 815822.

[134] Vago, J. L., P. M. Kintner, S. W. Chesney, R. L. Arnoldy, K. A. Lynch, T. E. Moore, and C. J. Pollock (1992), Transverse ion acceleration by lower hybrid waves in the topside auroral ionosphere, *J. Geophys. Res., 97*, 16, 935-16,957, doi:10.1029/92JA01526.

[135] Vahedi, V., and M. Surendra (1995), A Monte Carlo collision model for the particle-in-cell method:applications to argon and oxygen discharges, *Computer Phys. Commun., 87*, 179-198, doi:10.1016/0010-4655(94)00171.

[136] Winske, D., S. P. Gary, M. E. Jones, M. Rosenberg, D. A. Mendis and V. W. Chow (1995), Ion heating in a dusty plasma due to the dust/ion acoustic instability, *Geophys. Res. Lett., 22*, 2069-2072, doi:10.1029/95GL01983.

[137] Winske, D and P. C. Liewer (1978), Particle simulation studies of the lower hybrid drift instability, *Phys. Fluids, 21*, 1017-1025, doi: 10.1063/1.862321.

[138] Winske, D., S. P. Gary, M. E. Jones, M. Rosenberg, D. A. Mendis, and V. W. Chow (1995), Ion heating in a dusty plasma due to the dust/ion acoustic instability, *Geophys. Res. Lett.* , *22*, 2069-2072.

[139] Winske, D. and M. Rosenberg (1998), Nonlinear development of the dust acoustic instability in collisional dusty plasma, *IEEE Trans. Plasma Sci. 26*, 92-99.

[140] Winske, D., L. Yin, N. Omidi, H. Karimabadi, and K. B. Quest (2003), Hybrid simulation codes: Past, present and future: Tutorial, in Space Plasma Simulations, Lecture Notes in Phys., vol. 615, edited by J. Buechner, C. T. Dum, and M. Scholer, p. 359, Springer-Verlag, New York

[141] Winske, D. (1989), Development of flute modes on expanding plasma clouds, *Phys. Fluids B*, *1*, 1900, doi: 10.1063/1.858922.

[142] Winske, D. and W. Daughton (2012), Generation of lower hybrid and whistler waves by an ion velocity ring distribution, *Phys. Plasmas*, *19*, 072109, doi: 10.1063/1.4736983